

UNCLASSIFIED

AD 102823

Armed Services Technical Information Agency

Reproduced by

DOCUMENT SERVICE CENTER

KNOTT BUILDING, DAYTON, 2, OHIO

This document is the property of the United States Government. It is furnished for the duration of the contract and shall be returned when no longer required, or upon recall by ASTIA to the following address: Armed Services Technical Information Agency, Document Service Center, Knott Building, Dayton 2, Ohio.

NOTICE: WHEN GOVERNMENT OR OTHER DRAWINGS, SPECIFICATIONS OR OTHER DATA ARE USED FOR ANY PURPOSE OTHER THAN IN CONNECTION WITH A DEFINITELY RELATED GOVERNMENT PROCUREMENT OPERATION, THE U. S. GOVERNMENT THEREBY INCURS NO RESPONSIBILITY, NOR ANY OBLIGATION WHATSOEVER; AND THE FACT THAT THE GOVERNMENT MAY HAVE FORMULATED, FURNISHED, OR IN ANY WAY SUPPLIED THE SAID DRAWINGS, SPECIFICATIONS, OR OTHER DATA IS NOT TO BE REGARDED BY IMPLICATION OR OTHERWISE AS IN ANY MANNER LICENSING THE HOLDER OR ANY OTHER PERSON OR CORPORATION, OR CONVEYING ANY RIGHTS OR PERMISSION TO MANUFACTURE USE OR SELL ANY PATENTED INVENTION THAT MAY IN ANY WAY BE RELATED THERETO.

UNCLASSIFIED

AD No. 102823

ASTIA FILE COPY

WADC TECHNICAL REPORT 55-158

FC

INVESTIGATIONS OF THREE-DIMENSIONAL CASCADES

JAMES E. ASH

*ARMOUR RESEARCH FOUNDATION
ILLINOIS INSTITUTE OF TECHNOLOGY*

MAY 1956

WRIGHT AIR DEVELOPMENT CENTER

FOREWORD

This report was prepared by James E. Ash of the Heat-Power Research Department of the Armour Research Foundation of Illinois Institute of Technology. It covers the work accomplished on Air Force Contracts No. AF 33(616)-102 and No. 33(616)-2369 under Project No. 3066 "Gas Turbine Technology", Task No. 70155 "Subsonic Flow through Three-Dimensional Turbomachinery Cascades". Personnel contributing to the work were J.E. Ash, J.C. Lee, O.E. Teichmann, and R.S. Thiele.

The work was administered by the Fluid Dynamics Research Branch of the Aeronautical Research Laboratory, Wright Air Development Center, with Mr. S. Hasinger acting as Task Scientist.

WADC TECHNICAL REPORT 55-158

INVESTIGATIONS OF THREE-DIMENSIONAL CASCADES

JAMES E. ASH

ARMOUR RESEARCH FOUNDATION
ILLINOIS INSTITUTE OF TECHNOLOGY

MAY 1956

AERONAUTICAL RESEARCH LABORATORY
CONTRACT AF 33(616)-2369
PROJECT 3066
TASK 70155

WRIGHT AIR DEVELOPMENT CENTER
AIR RESEARCH AND DEVELOPMENT COMMAND
UNITED STATES AIR FORCE
WRIGHT-PATTERSON AIR FORCE BASE, OHIO

ABSTRACT

The actual flow conditions within the passages of a 14-inch diameter, four-bladed impeller of a mixed flow compressor have been investigated and compared with design values, which were based on axial symmetry and incompressible, nonviscous flow. The blades were designed as bound-vortex sheets, having a zero tangential component of vorticity, i.e., the velocity distribution in meridional planes is not disturbed by the blades. Flow surveys at the impeller outlet from hub to shroud and from blade to blade were made with a three-dimensional, spherical pitot probe mounted on the impeller. This probe and also mercury seals for transferring the pressure signals from the rotating shaft to stationary manometers were especially developed for this investigation. Test runs conducted in the range from 1500 to 3000 rpm and from 8.7 to 44.1 cubic feet per second showed that the shape of the meridional velocity distribution between hub and shroud agrees essentially with the theory. However, in the blade-to-blade direction the distribution curves for the meridional velocity are displaced as much as 20% above and 10% below the average. Variations in the cone angle of the relative velocity are only in the order of 2° and 3° , i.e., the flow does not "twist" away much from surfaces of revolution. The median impeller slip factor was 0.57 within the test range.

The blade-to-blade distribution of the flow on the mean stream surface was also calculated by the relaxation method. It was found that the actual flow was more uniform than calculations showed. This may be due to the rapid reduction of the blade load near the tip and the shifting of low energy air toward the trailing face of the blades observed for all test runs.

The experimental techniques developed in the course of this investigation can be used to obtain consistent and reproducible surveys of the internal flow distribution in rotating cascades.

PUBLICATION REVIEW

This report has been reviewed and is approved.

FOR THE COMMANDER:

Aldro Lingard

ALDRO LINGARD, Colonel, USAF
Chief, Aeronautical Research Laboratory
Directorate of Research

4

TABLE OF CONTENTS

	<u>Page</u>
FOREWORD	
ABSTRACT	
I. INTRODUCTION	1
II. THEORETICAL ANALYSES	2
A. General Theory	2
B. Infinite Number of Blades	6
1. Vortex Theory of Flow	6
2. Special Case of Zero Ring-Vortex	8
3. Blade Design for Zero Ring-Vortex	10
C. Finite Number of Blades	25
1. General Considerations	25
2. Equation of Motion on the Mean Meridional Stream Surface	27
a. Absolute Irrotational Motion	27
b. Continuity Equation	27
c. General Equation	31
d. Boundary Conditions	32
3. Results of the Relaxation Solution	39
III. EXPERIMENTAL INVESTIGATION	41
A. Description of the Test Stand	41
B. Instrumentation	46
1. Inlet Conditions	46
2. Outlet Conditions	46
a. Preliminary Considerations	46
b. Three-Dimensional Spherical Pitot-Probe	48

	<u>Page</u>
c. Rotary Seal Pressure Take-Offs	50
3. Overall Performance	52
C. Test Procedure	53
D. Presentation of Data	53
1. Internal Flow Measurements	53
2. Efficiency, Discharge and Head Characteristic	55
IV. CORRELATION OF THEORY AND EXPERIMENTAL RESULTS	71
A. Disturbance of the Meridional Streamline Pattern	71
B. Similarity Considerations	74
C. Variation in the Energy and Whirl-Moment Values	74
D. Comparison with the Blade to Blade Solution	75
E. Impeller Slip Factor	77
F. Overall Performance	79
V. SUMMARY AND CONCLUSIONS	81
APPENDICES	
A. Symbols	84
B. The Three-dimensional Spherical Pitot-Probe	88
1. Theoretical Calibration Curves	88
2. Experimental Calibration Curves	94
3. Relation of the Probe to the Impeller Geometry	97
4. Numerical Example	103
C. Details of the Blade-to-Blade Relaxation Solution	106
1. Method of Solution	106
2. Irregular Grid Points	106
3. Kutta-Joukowski Condition	109
4. Determination of Velocity Distribution	110
BIBLIOGRAPHY	111

LIST OF ILLUSTRATIONS

<u>Figure</u>		<u>Page</u>
1	Velocity Diagram Notation	4
2	Dimensionless Layout of Meridional Streamline Pattern	12
3	Discharge and Meridional Velocity Distribution Along Orthogonal	15
4	Dimensionless Meridional Velocity Distribution Along Orthogonals	17
5	Variation of Dimensionless Meridional Velocity Component Along Meridional Streamlines	17
6	Dimensionless Whirl-Moment Diagram	17
7	Graphical Blade-Design Procedure	20
8	Mean Stream Surface of Revolution for Axial-Symmetry Conditions .	28
9	Circulation and Velocity Diagram on Mean Stream Surface	28
10	Elemental Region for Application of Continuity Equation	30
11	Mesh Notation about Central Point O	30
12	Mean Meridional Streamline Coordinates and Channel Height	33
13	Variation of ξ , η , B, and $\sin \delta$ with the Radial Coordinate . . .	34
14	Curves for Determination of the Function, $f(\xi_0) = -\frac{1}{2} \frac{d \ln B}{d \xi}$. .	34
15	Boundary Conditions for the Flow Field on the Mean Stream Surface	38
16	Relative Streamlines at the Design Condition	40
17	Schematic Diagram of the Test Stand	42
18	Test Stand and Dynamometer Unit	43
19	Inlet Nozzle and Straightening Vanes	44
20	Front View of Impeller	45
21	Impeller with Spherical Pitot-Probe Mounted on Positioning Disk .	45

<u>Figure</u>		<u>Page</u>
22	Section of Mercury Seal for Pressure Transfer	51
23	Plan View Perpendicular to Impeller Axis Showing Circumferential Positions of Spherical Pitot	54
24	Traverse Positions of the Spherical Pitot in the Meridian Plane	54
25	Distribution of Meridional Component of Dimensionless Relative Velocity Between Hub and Shroud Surfaces at Impeller Outlet . . .	62
26	Distribution of Meridional Component of Dimensionless Relative Velocity Along Periphery at Impeller Outlet.	64
27	Variation of Tangential Exit Angle for Relative Velocity Along Periphery at Impeller Outlet	65
28	Variation of Relative Flow Direction in Meridional Plane at Impeller Outlet	66
29	Distribution of Whirl-Moment Along Periphery at Impeller Outlet .	67
30	Distribution of Energy Input to Flow as Measured Along Periphery at Impeller Outlet	68
31	Efficiency and Head Characteristic	70
32	Static Pressure Variation From Hub to Shroud at Impeller Outlet .	72
33	Static Pressure Variation from Blade to Blade on Mean Stream Surface at Impeller Outlet	73
34	Variation of Impeller Efficiency from Blade to Blade at Impeller Outlet	76
35	Comparison of Measured and Theoretical Meridional Velocity Distribution on Mean Stream Surface at the Impeller Outlet	78
36	Impeller Slip Factor	80
B1	Notation for Spherical Probe-Head	89
B2	Theoretical Calibration Curves for 5-Hole Spherical Pitot-Probe .	93
B3	Spherical Pitot-Probe Calibration Fixture	95
B4	Constructional Details of Spherical Pitot-Probe	96

<u>Figure</u>		<u>Page</u>
B5	Calibration Curves of Spherical Pitot for Determination of Magnitude and Direction of Flow	98
B6	Calibration Curves of Spherical Pitot for Determination of Static Pressures	100
C1	Notation for Irregular Star Operator	108
C2	Notation for Star Operator Applied at Blade Inlet Tip	108
C3	Irregular Transition Point between Fine and Coarse Grids	108

LIST OF TABLES

<u>Table</u>		<u>Page</u>
I	Meridian Streamline Pattern Data	16
II	Blade Design for Design Parameter, $Q/\omega D^3 = 0.060$	23
III	Cylindrical Coordinates of Streamlines on Front and Back Vane Surfaces	24
IV	Mean Stream Surface Data	35
V	Four Bladed Impeller Data	56
VI	Comparison of Inlet and Outlet Flow Rates	70

I. INTRODUCTION

Considerable progress has been achieved in the past for the one and two-dimensional methods of analysis as applied to radial-flow and axial-flow turbomachines. However, in mixed-flow machines, the three-dimensional effects are of relatively greater importance, and further knowledge is required of the detailed flow conditions. Recent analyses (for example, those of Wu² and Stanits^{4, 5}) of inviscid, three-dimensional flow suggest methods for the design of blade cascades. However, general use of these methods is restricted because of the complexity and great expenditure of effort involved in their application, and because of the lack of experimental knowledge necessary to establish the limitations of the theory. Therefore, the objective of this investigation is to provide additional experimental information pertaining to the flow conditions within the impeller and to evaluate the theory in terms of the experimental data. In an effort to supplement the existing experimental techniques, a three-dimensional, spherical pitot-probe and a pressure-transfer device employing mercury seals have been developed for measurement of the relative flow fields within the rotating impeller.

An experimental, four-blade, mixed-flow impeller was constructed in accordance with a design procedure developed from a bound-vortex theory of the flow presented by Spannhake¹. Axial symmetry was assumed in the design, and the flow was considered to be nonviscous, incompressible, and steady. The experimental investigation of the impeller was conducted in

For all numbered references, see bibliography

NOTE: This publication was released in February 1956.

a compressor-cascade test stand using air as the fluid medium.

A quasi-three-dimensional, relaxation solution of the blade-to-blade variation in the flow on the mean stream surface of revolution was computed according to methods proposed by Stanitz^{4,5} in order to investigate the suitability of numerical methods as applied to the more general curved blades of the experimental impeller. The circumferential variation in the flow predicted on the basis of this theory is compared with the measured results.

II. THEORETICAL ANALYSES

A. General Theory

The dynamic equation governing the three-dimensional flow of an inviscid fluid through a turbomachine, neglecting body forces,

$$\bar{a} = -\frac{1}{\rho} \nabla p \quad (1)$$

follows directly from Newton's second law of motion. Considering the density to be a function of the pressure only, the pressure gradient may be expressed as an integral term by means of the relation,

$$\frac{1}{\rho} \nabla p = \nabla \int \frac{dp}{\rho}. \quad (2)$$

With reference to a cylindrical coordinate system fixed to the impeller and rotating with a constant angular speed, the fluid acceleration is given by the equation

$$\bar{a} = \bar{a}_{rel} + 2\bar{\omega} \times \bar{w} - \omega^2 \bar{r}, \quad (3)$$

where \bar{r} is the cylindrical radial-coordinate, and $2\bar{\omega} \times \bar{w}$ is the Coriolis acceleration. The relative acceleration may be expressed in terms of the

relative velocity \bar{w} as

$$\bar{a}_{rel} = \frac{\partial \bar{w}}{\partial t} + (\bar{w} \cdot \nabla) \bar{w} = \frac{D\bar{w}}{dt} . \quad (4)$$

Considering the relative motion to be steady, $\frac{\partial \bar{w}}{\partial t} = 0$, and making use of the vector identity, $(\bar{w} \cdot \nabla) \bar{w} = \nabla \frac{w^2}{2} - \bar{w} \times \bar{\lambda}_{rel}$, the basic dynamic equation becomes

$$\nabla \left(\frac{w^2}{2} + \int \frac{dp}{\rho} \right) + 2\bar{\omega} \times \bar{w} - \omega^2 \bar{r} - \bar{w} \times \bar{\lambda}_{rel} = 0. \quad (5)$$

The law of cosines applied to the triangle formed by the velocity diagram shown in Fig. 1 yields the relation,

$$w^2 = c^2 + (r\omega)^2 - 2 r \omega c_t, \quad (6)$$

and by substitution into equation (5), making use of the vector identity $\nabla r^2 = 2 \bar{r}$, there is obtained the equation

$$\nabla \left(\frac{c^2}{2} + \int \frac{dp}{\rho} - \omega r c_t \right) + 2\bar{\omega} \times \bar{w} - \bar{w} \times \bar{\lambda}_{rel} = 0. \quad (7)$$

It is convenient to introduce the energy input H and the quantity I according to the definitions

$$gH = \frac{c^2}{2} + \int \frac{dp}{\rho}, \quad (8)$$

$$I = H - \frac{\omega}{g} r c_t . \quad (9)$$

Equation (7)* may be expressed as

$$g\nabla I + 2\bar{\omega} \times \bar{w} - \bar{w} \times \bar{\lambda}_{rel} = 0. \quad (7a)$$

The vorticity of the absolute motion is related to the relative vorticity by the relationship

$$\bar{\lambda}_{rel} = \bar{\lambda} - 2\bar{\omega}, \quad (10)$$

and an alternate form of equation (7a) is

$$g\nabla I - \bar{w} \times \bar{\lambda} = 0. \quad (7b)$$

Differentiation of the quantity I with respect to the relative fluid motion, together with equations (6), (8), and (9), leads to an important general consideration:

$$\begin{aligned} \frac{D}{dt} (gI) &= \frac{D}{dt} \left(\frac{w^2}{2} - \frac{(r\omega)^2}{2} \right) + \frac{1}{\rho} \frac{D}{dt} p \\ &= \bar{w} \cdot \frac{D}{dt} \bar{w} - \bar{w} \cdot \omega^2 \bar{r} + \frac{1}{\rho} \frac{\partial p}{\partial t} - \bar{w} \cdot \left[\frac{D}{dt} \bar{w} + 2\bar{\omega} \times \bar{w} - \omega^2 \bar{r} \right] \\ &= \frac{1}{\rho} \frac{\partial p}{\partial t}. \end{aligned} \quad (11)$$

For steady relative motion, the pressure at any fixed point relative to the impeller can be considered constant, and hence, from equation (11), the value of I for any fluid particle passing through the blade cascade

* A more general derivation of this equation for an ideal gas, involving heat conduction, is given by Wu²,

$$\frac{\partial \bar{w}}{\partial t} - \bar{w} \times (\nabla \times \bar{w}) + 2\bar{\omega} \times \bar{w} = -g\nabla I + T\nabla(\text{specific entropy}).$$

will remain constant. In terms of the whirl moment, $m = r\omega_z$, the well known Euler's turbine relation is obtained,

$$\nabla H = \frac{U}{g} \nabla m. \quad (12)$$

If the flow upstream of the blade cascade has a uniform distribution of I , so that the gradient of I is zero, then, from equation (7b), the absolute vortex lines must coincide with the relative streamlines, and the absolute vorticity of the flow will remain unchanged on passing through the blade cascade.

B. Infinite Number of Blades

1. Vortex Theory of Flow

A considerable simplification in the analysis of the flow through blade cascades is obtained by considering the fluid to be perfectly guided by the blade surfaces. That is to say, every relative stream surface is assumed to conform exactly to the blade shape. However, this can be achieved only if the spacing between the blades is very small, confining the fluid motion essentially to the curved surface of the blade. As an idealization, an infinite number of blades of infinitesimal thickness will be assumed. Under certain conditions, it has been found that analyses based upon this idealization will lead to solutions that give a good approximation of the mean flow between blades (Spannhake¹). By the introduction of an infinite number of blades, the general three-dimensional motion of the fluid is reduced to a two-dimensional motion on the blade surface completely described by two independent variables. By this assumption, the variable θ can be eliminated, as there is no variation about the axis of the cascade, and the cylindrical coordinates r and z will

suffice as the independent variables for steady motion.

In an actual impeller with a finite number of blades the flow is acted upon by pressure differences developed by the blade surfaces. For a given change in angular momentum of the through flow, these pressure differences will diminish as the blade number increases; however, as the space between the blades gets smaller, the weight flow acted upon by the pressure difference is reduced. In the limit, the ratio of the blade force to the fluid weight is a finite value, commonly referred to as the "distributed blade force", and represents the action of the blade cascade. This fictitious force \bar{K} may be introduced as an additional term into the basic dynamic equation (1),

$$\bar{a} = -\frac{1}{\rho} \nabla p + \frac{\bar{K}}{\rho}. \quad (13)$$

Carrying this additional force term through the steps leading to equation (7b), there will be obtained

$$g \nabla I - \bar{w} \times \bar{\lambda} = \frac{\bar{K}}{\rho}. \quad (14)$$

The force \bar{K} is used to define the bound vorticity associated with the blading,

$$\bar{K} = -\rho \bar{w} \times \bar{\lambda}_0. \quad (15)$$

The vector \bar{K} is normal to the blade surface since it represents the pressure force due to the blading; and as \bar{w} is tangent to the blade surface*, it necessarily follows from equation (15) that the bound vortex lines lie

* This implies, $\bar{w} \cdot \bar{K} = 0$.

in the blade surface. The sum of the bound vorticity attached to the blading and free vorticity of the flow is the total vorticity,

$$\bar{\lambda} = \bar{\lambda}_b + \bar{\lambda}_f .$$

The free vortices are acted upon only by the gravitational field; they follow the Helmholtz laws, and have no relationship with the force \bar{K} .

Equation (14) may then be expressed as

$$g \nabla I - \bar{w} \times \bar{\lambda}_b - \bar{w} \times \bar{\lambda}_f = \frac{\bar{K}}{\rho} . \quad (17)$$

From the definition of the bound vortices, equation (15), it follows that

$$g \nabla I - \bar{w} \times \bar{\lambda}_f = 0 . \quad (18)$$

For the same reasons as discussed immediately following equation (11), the fluid particles that have a uniform distribution of I in a region upstream of the blade cascade will move along relative streamlines which satisfy the relation

$$\bar{w} \times \bar{\lambda}_f = 0 . \quad (19)$$

Equation (19) implies that either the free vorticity is zero, or the free vortex lines coincide with the relative streamlines.

2. Special Case of Zero Ring Vortex ($\lambda_r = 0$)

The impeller used in the experimental investigation was designed in accordance with the preceding theory for an inviscid fluid passing through a cascade consisting of an infinite number of blades. A further simplification in the design procedure is introduced by imposing the

condition that the tangential component of the vorticity be zero. In terms of the cylindrical coordinate system, the tangential component of the vorticity is

$$\lambda_t = \frac{\partial c_r}{\partial z} - \frac{\partial c_z}{\partial r} = 0 . \quad (20)$$

On the basis of the continuity equation, it is necessary that the radial and axial components of both the absolute and relative fluid velocities at any point be identical. That is,

$$c_r = w_r ,$$

$$c_z = w_z ,$$

and hence,

$$\frac{\partial w_r}{\partial z} - \frac{\partial w_z}{\partial r} = 0 . \quad (21)$$

The equation of the blade surface may be represented by the equation

$$F(r,z) + \theta = 0 . \quad (22)$$

The direction numbers of a normal \bar{n} to the blade surface are $(\frac{\partial F}{\partial z}, \frac{\partial F}{\partial r}, \frac{1}{r})$. The free vortex lines must lie in the blade surface because they coincide with the relative streamlines. Further, since the bound vortex lines lie in the blade surface, it follows that the total absolute vortex lines must also lie in the blade surface as they are determined by the vector sum of the free and bound vortices. This implies that

$$\bar{n} \cdot \bar{\lambda} = 0 ,$$

and

$$\frac{\partial F}{\partial z} \lambda_z + \frac{\partial F}{\partial r} \lambda_r + \frac{1}{r} \lambda_t = 0. \quad (23)$$

The radial and axial components of the vorticity vector are

$$\lambda_r = \frac{1}{r} \frac{\partial c_z}{\partial \theta} - \frac{1}{r} \frac{\partial rc_t}{\partial z},$$

$$\lambda_z = \frac{1}{r} \frac{\partial rc_t}{\partial r} - \frac{1}{r} \frac{\partial c_r}{\partial \theta}.$$

The infinite blade restriction implies axial symmetry so that differentiation with respect to θ is zero. Introducing the whirl moment, $m = rc_t$, and for $\lambda_t = 0$, equation (23) simplifies to

$$\frac{\partial F}{\partial z} \frac{\partial m}{\partial r} - \frac{\partial F}{\partial r} \frac{\partial m}{\partial z} = 0. \quad (24)$$

The left side of this equation is the Jacobian determinant of the functions $F(r,z)$ and $m(r,z)$, and the vanishing of this determinant implies the functional dependence of F and m . This means that

$$m = m(F)$$

$$= m(\theta), \quad (25)$$

and, consequently, the intersection of the blade surface with radial planes ($\theta = \text{constant}$) are lines of constant whirl-moment.

3. Blade Design for Zero Ring-Vortex

a. Determination of the Meridional Streamline Pattern

As a preliminary consideration, suppose there are no blades present between the hub and shroud surfaces. Irrotational flow (i.e. flow having zero vorticity) passing through this annular space will satisfy the condition

$$\frac{\partial w_r}{\partial s} = \frac{\partial w_s}{\partial r} . \quad (26)$$

This differential equation may be used as the basis for the meridional streamline pattern of the free flow through the annular space without blading. If blades, or the equivalent bound-vortex surfaces, are introduced such that the tangential component of vorticity is zero, then equation (21) will be valid. This means that equation (26), which applies to the free flow without blading, will remain unchanged by the presence of blades designed so that λ_t is identically zero.

The first step in the blade design is the determination of the meridional flow pattern for free irrotational flow between specified contours of the hub and shroud surfaces. The natural coordinate system (s, n, θ) is convenient to use for this determination. The flow is irrotational,

$$\frac{\partial c_n}{\partial s} - \frac{\partial c_m}{\partial n} = 0, \quad (27)$$

and the convective component of the acceleration in the direction normal to the streamline is

$$c_m \frac{\partial c_n}{\partial s} = \frac{c^2}{r_c} , \quad (28)$$

and, hence, the irrotational condition may be expressed by

$$\frac{\partial c_m}{\partial n} = \frac{c_m}{r_c} . \quad (29)$$

This differential equation may be integrated along an orthogonal (Fig. 2),

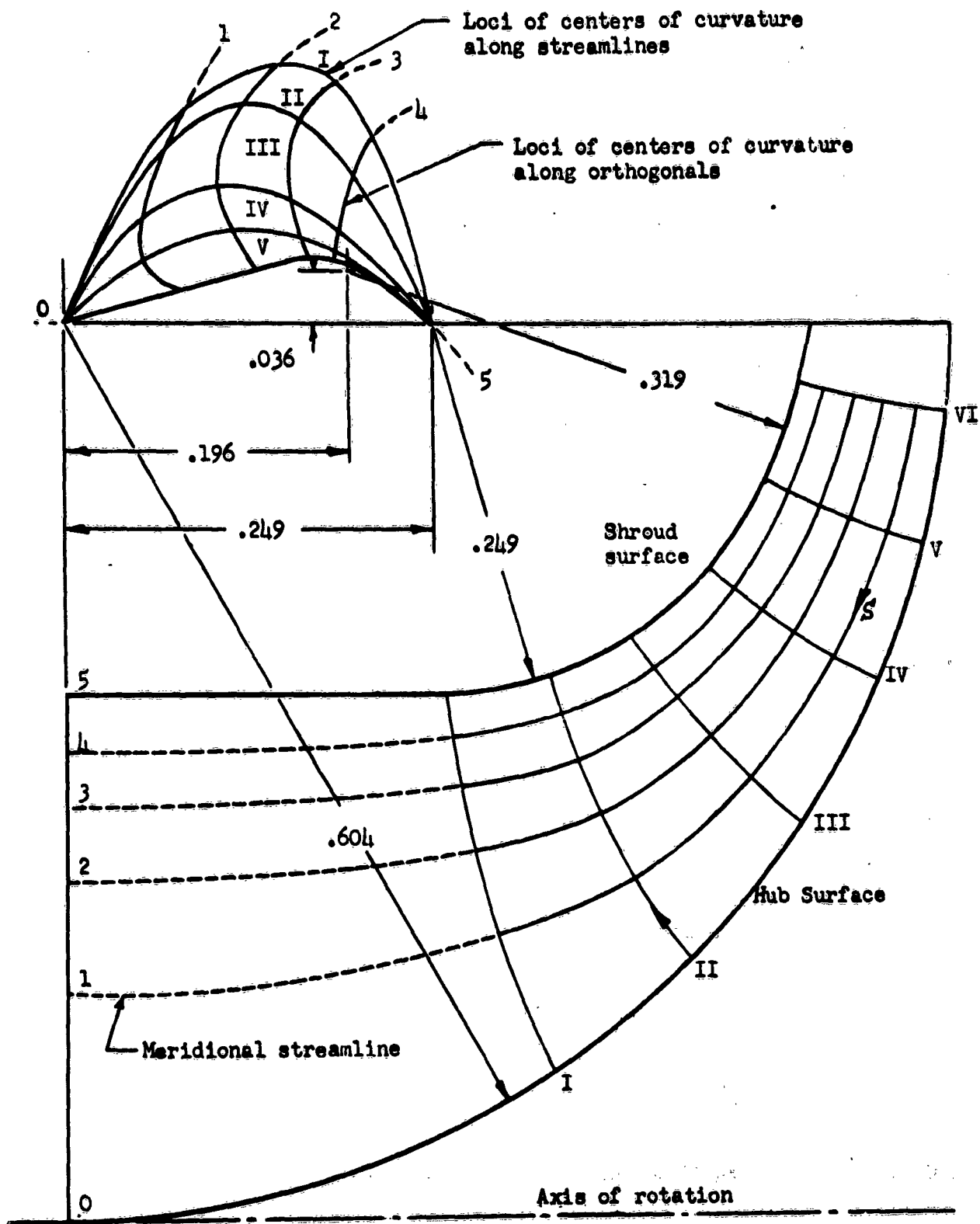


Fig. 2 DIMENSIONLESS LAYOUT OF MERIDIONAL STREAMLINE PATTERN

$$\ln \frac{c_m}{c_{mo}} = \int_0^n \frac{1}{r_c} dn,$$

and

$$\frac{c_m}{c_{mo}} = \exp \int_0^{n/\Delta n} \frac{\Delta n}{r_c} d\left(\frac{n}{\Delta n}\right). \quad (30)$$

The velocity distribution along an orthogonal, given by equation (30), satisfies the irrotational flow condition. If the meridional streamline pattern is constructed to satisfy this condition, together with a continuity requirement, the streamline pattern will be uniquely determined. The continuity condition requires that the same flow rate cross any two sections between adjacent stream surfaces. The volume rate of flow passing between the hub surface ($n = 0$), and any other stream surface is

$$Q_n = \int_0^n 2\pi r c_m dn,$$

and, in dimensionless form,

$$\frac{Q_n}{D^2 c_{mo}} = 2\pi \frac{\Delta n}{D} \int_0^{n/\Delta n} \frac{r}{D} \frac{c_m}{c_{mo}} d\left(\frac{n}{\Delta n}\right). \quad (31)$$

Equations (30) and (31) can be satisfied by a graphical method of computation. For the specified hub and shroud surface contours of Fig. 2, a number of estimated orthogonals are sketched into the meridional plane. For each of the orthogonals, the velocity distribution given by equation (30) is solved by graphical integration. This is done

most easily by estimating the distribution of $\Delta n/r_c$ along the orthogonal, and plotting this distribution against $n/\Delta n$. The area under this curve up to any value of $n/\Delta n$, represents the dimensionless velocity c_m/c_{m0} at this point; and from the area values, the distribution shown in Fig. 3 is obtained. The dimensionless discharge, also shown in Fig. 3, is computed from equation (31) by a graphical integration. From this discharge plot, the n -coordinates of the streamlines which equally partition the flow along each orthogonal are determined. Using the appropriate radius and center of curvature at each of these n -coordinates, the arcs of the meridional streamlines are drawn in with a compass. If the arcs blend into a smooth curve, the correct meridional streamlines have been obtained, satisfying both the continuity and irrotational flow conditions. If the arcs do not blend together, the original estimates of the orthogonals must be modified and the computational procedure repeated. The dimensionless layout of the meridional streamline pattern shown in Fig. 2 was obtained after the second computation. The pertinent numerical values for this streamline pattern are presented in Table I. The distribution of the dimensionless velocity $\frac{c_m}{Q/D^2}$ along each orthogonal, and along each meridional streamline, is shown in Figs. 4 and 5 respectively.

b. Determination of the Blade Shape

The design of the blade surface, considered as a bound vortex-sheet, is such that at the design operating condition the ring-component of the bound vorticity is zero. The design operating condition is dependent upon the desired discharge for a given speed and impeller size, and is fixed by a suitable choice of the design parameter, $Q/\omega D^3$.

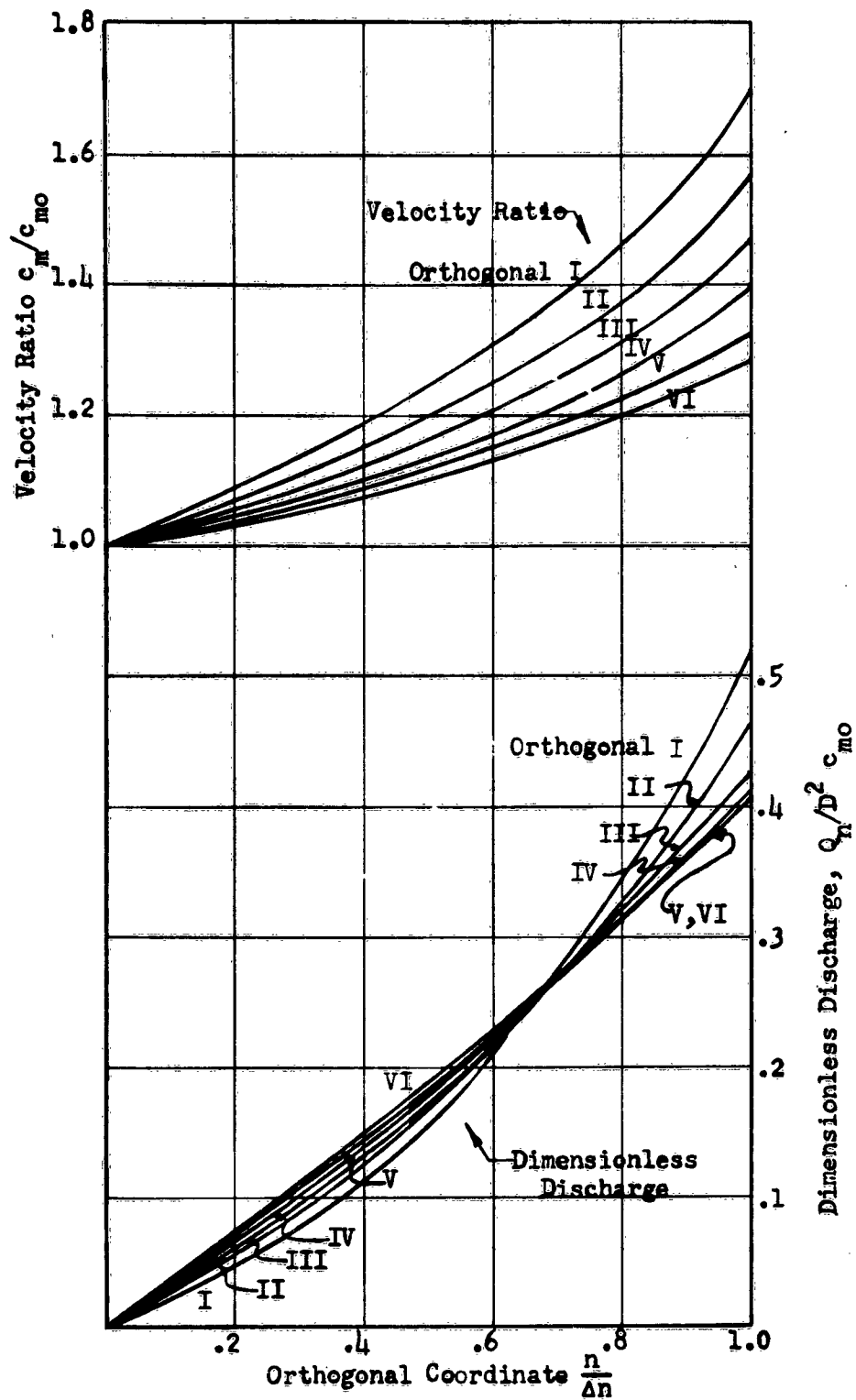


Fig. 3 DISCHARGE AND MERIDIONAL VELOCITY DISTRIBUTION ALONG ORTHOGONAL.

Table I

MERIDIAN STREAMLINE PATTERN DATA

	Meridian Streamline	$N = \frac{n}{D}$	$R = \frac{r}{D}$	$s = \frac{s}{D}$	$\frac{n}{\Delta n}$	$R_0 = \frac{r_0}{D}$	$\frac{\Delta n}{r_0}$	$\frac{Q_n}{D^2 \sigma_{no}}$	$\frac{\sigma_n}{\sigma_{no}}$	$\frac{\sigma_n}{Q/D^2}$
Orthogonal I $\frac{\Delta n}{D} = 0.270$	0	0	0.0994	0.452	0	0.604	0.447	0	1.000	1.930
	1	0.1014	0.1927	0.404	0.375	0.591	0.456	0.104	1.178	2.27
	2	0.1606	0.250	0.366	0.595	0.545	0.496	0.208	1.309	2.52
	3	0.209	0.291	0.329	0.756	0.480	0.563	0.311	1.429	2.75
	4	0.240	0.326	0.302	0.887	0.406	0.670	0.425	1.548	2.98
5	0.270	0.356	0.277	1.000	0.249	1.085	0.519	1.696	3.27	
Orthogonal II $\frac{\Delta n}{D} = 0.219$	0	0	0.1751	0.329	0	0.604	0.363	0	1.000	2.16
	1	0.068	0.229	0.299	0.310	0.582	0.376	0.0925	1.120	2.42
	2	0.1180	0.265	0.273	0.538	0.534	0.411	0.1850	1.225	2.64
	3	0.1576	0.318	0.217	0.719	0.469	0.467	0.2775	1.326	2.86
	4	0.1909	0.340	0.226	0.870	0.385	0.570	0.3700	1.433	3.10
5	0.219	0.367	0.206	1.000	0.249	0.882	0.463	1.563	3.38	
Orthogonal III $\frac{\Delta n}{D} = 0.1733$	0	0	0.266	0.208	0	0.604	0.287	0	1.000	2.34
	1	0.0463	0.296	0.195	0.267	0.556	0.311	0.085	1.083	2.53
	2	0.0856	0.325	0.180	0.494	0.500	0.347	0.171	1.166	2.72
	3	0.1194	0.351	0.165	0.689	0.432	0.401	0.257	1.254	2.93
	4	0.1450	0.374	0.155	0.853	0.348	0.497	0.342	1.350	3.16
5	0.1731	0.393	0.143	1.000	0.249	0.697	0.428	1.470	3.44	
Orthogonal IV $\frac{\Delta n}{D} = 0.2400$	0	0	0.364	0.099	0	0.604	0.232	0	1.000	2.43
	1	0.0342	0.380	0.093	0.244	0.542	0.258	0.082	1.062	2.58
	2	0.0644	0.396	0.087	0.460	0.471	0.297	0.165	1.126	2.74
	3	0.0917	0.413	0.079	0.655	0.398	0.352	0.247	1.200	2.92
	4	0.1175	0.428	0.076	0.840	0.321	0.437	0.329	1.290	3.14
5	0.1400	0.441	0.071	1.000	0.249	0.563	0.411	1.395	3.39	
Orthogonal V $\frac{\Delta n}{D} = 0.1190$	0	0	0.456	0	0	0.604	0.197	0	1.000	2.47
	1	0.0274	0.464	0	0.231	0.500	0.238	0.082	1.052	2.59
	2	0.524	0.474	0	0.440	0.437	0.272	0.163	1.110	2.73
	3	0.0770	0.482	0	0.647	0.387	0.307	0.244	1.178	2.90
	4	0.0988	0.492	0	0.830	0.350	0.340	0.325	1.249	3.07
5	0.1190	0.500	0	1.000	0.319	0.373	0.407	1.327	3.26	
Orthogonal VI $\frac{\Delta n}{D} = 0.1036$	0	0	0.547	-0.091	0	0.604	0.172	0	1.000	2.45
	1	0.0230	0.550	-0.086	0.222	0.498	0.208	0.082	1.042	2.57
	2	0.0442	0.553	-0.082	0.430	0.432	0.240	0.163	1.091	2.69
	3	0.0652	0.556	-0.078	0.629	0.384	0.270	0.244	1.148	2.82
	4	0.0850	0.561	-0.074	0.820	0.347	0.299	0.325	1.212	2.98
5	0.1036	0.565	-0.071	1.000	0.319	0.325	0.406	1.282	3.16	

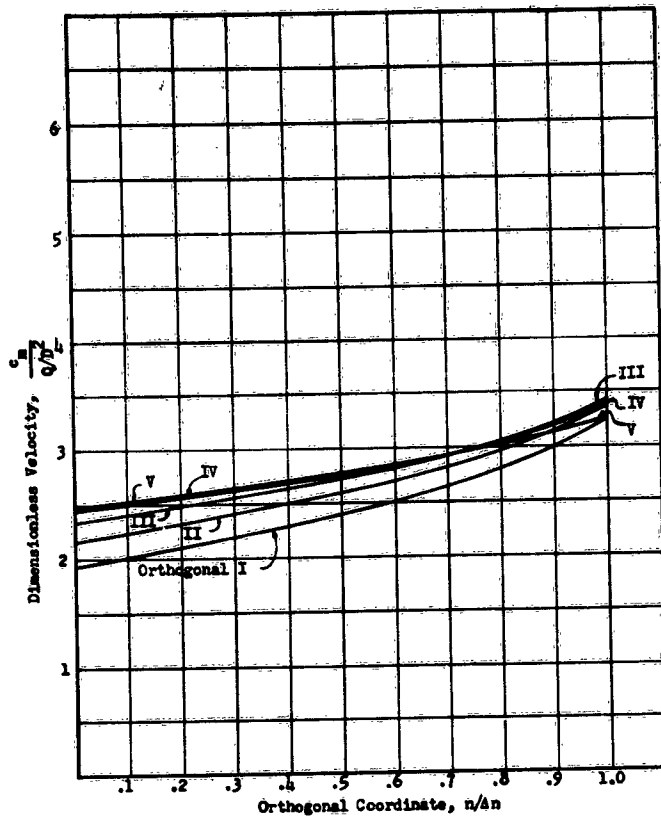


Fig. 4 DIMENSIONLESS MERIDIONAL VELOCITY DISTRIBUTION ALONG ORTHOGONALS.

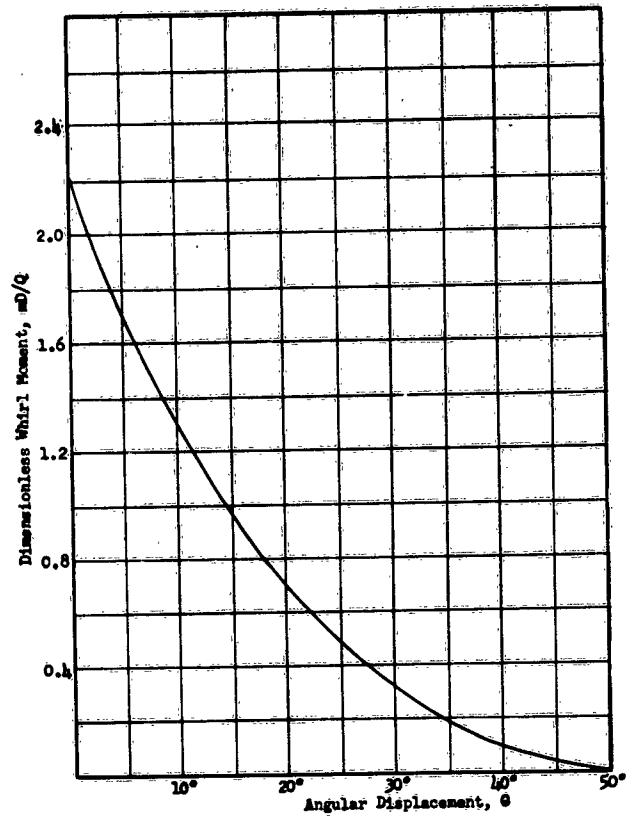


Fig. 6 DIMENSIONLESS WHIRL-MOMENT DIAGRAM

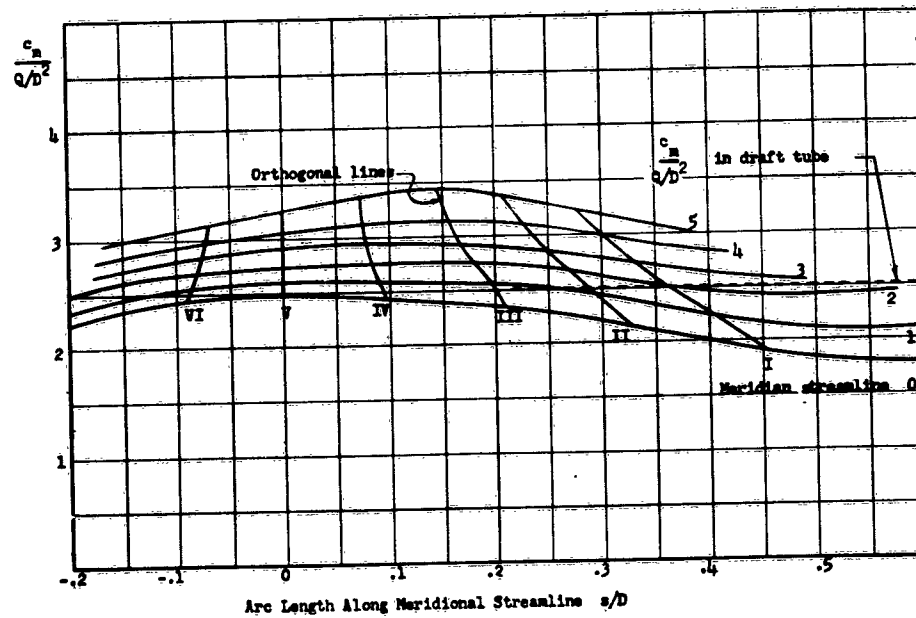


Fig. 5 VARIATION OF DIMENSIONLESS MERIDIONAL VELOCITY COMPONENT ALONG MERIDIONAL STREAMLINES

The blade design is based upon a typical value for this type of mixed-flow impeller of $Q/\omega D^3 = 0.060$. The blade cascade satisfying these conditions will not disturb the meridional streamline pattern already determined for the free flow.

Equation (25) expresses the fact that the intersection line of the blade surface with any radial plane is a line of constant whirl-moment. The whirl-moment is a function of θ , and can be arbitrarily chosen; however, several trials may be necessary to produce a desirable blade shape. For example, the total length of the blade may turn out to be very different along the hub and the shroud surfaces. How to change the whirl-moment for a desired modification of the blade shape is easily understood, once one has gone through the design procedure. The first choice of whirl-moment for the blade design of the test impeller led to a double-curvature of the blade along the shroud surface. The whirl-moment was adjusted so that this double-curvature was eliminated, and the final choice of whirl-moment distribution is shown in Fig. 6.

The design of the experimental blade cascade was accomplished by a combined numerical and graphical procedure. The differential equation of the relative streamlines on a conical development is

$$\frac{w_t}{w_m} = r \frac{d\theta}{ds} = \cot \beta, \quad (32)$$

and may be approximated by a finite-difference equation expressed in dimensionless form,

$$\delta \theta = \frac{1}{R} \cot \beta \delta S. \quad (33)$$

From this equation, angular increments were computed for constant incremental arc lengths, $\delta S = 0.028$, starting from the blade exit edge chosen along orthogonal V as shown in Fig. 2. The corresponding values of R were measured directly from this figure, and the values of $\cot\beta$ were determined from the velocity diagram at each point. It is apparent from the velocity diagram shown in Fig. 1, that the tangential and meridional relative velocity components are given by

$$w_t = u - c_t,$$

$$w_m = c_m.$$

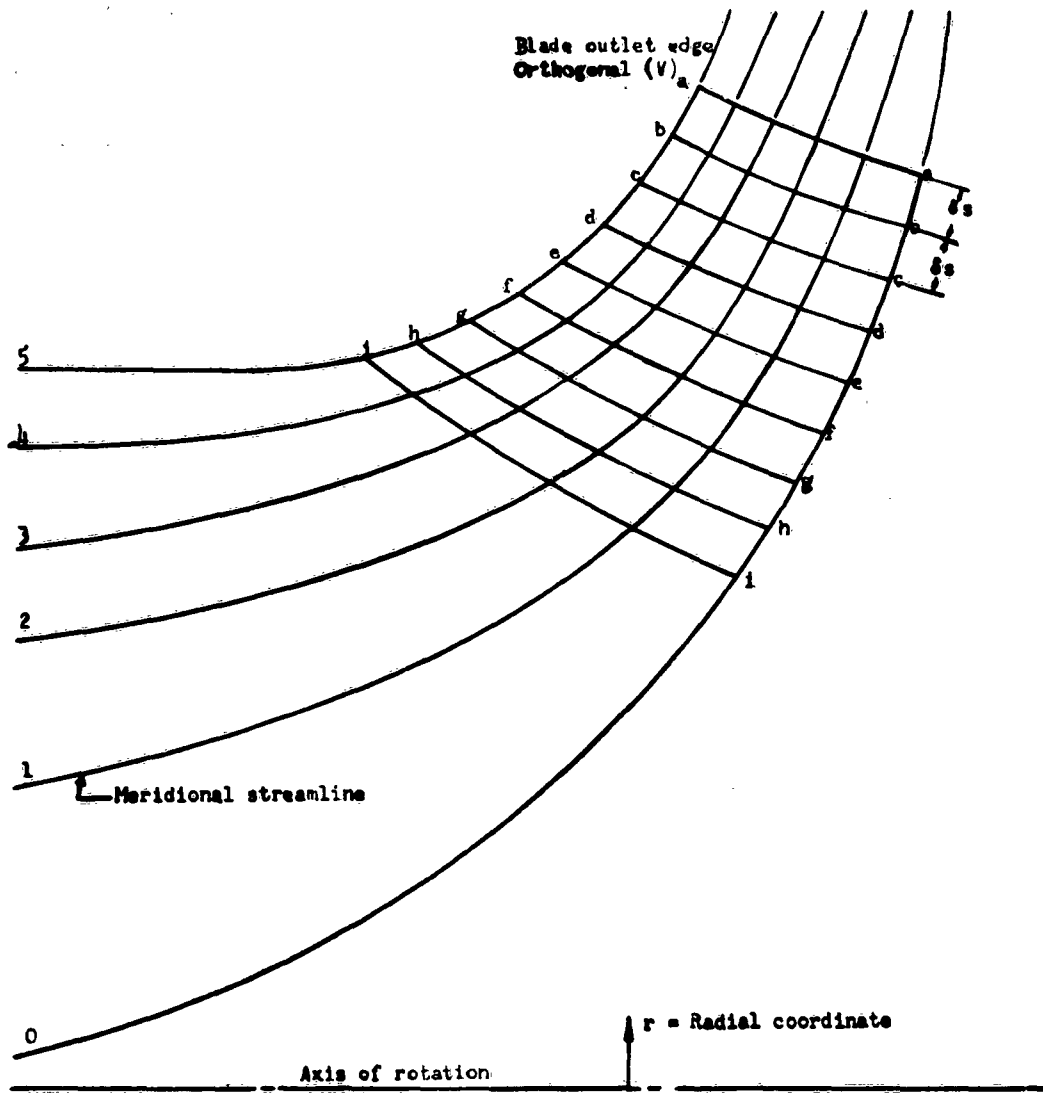
Introducing the whirl-moment, $m = rc_t$, the value of $\cot\beta$ is determined from the equation

$$\cot\beta = \frac{u - \frac{m}{r}}{c_m},$$

and, in dimensionless form,

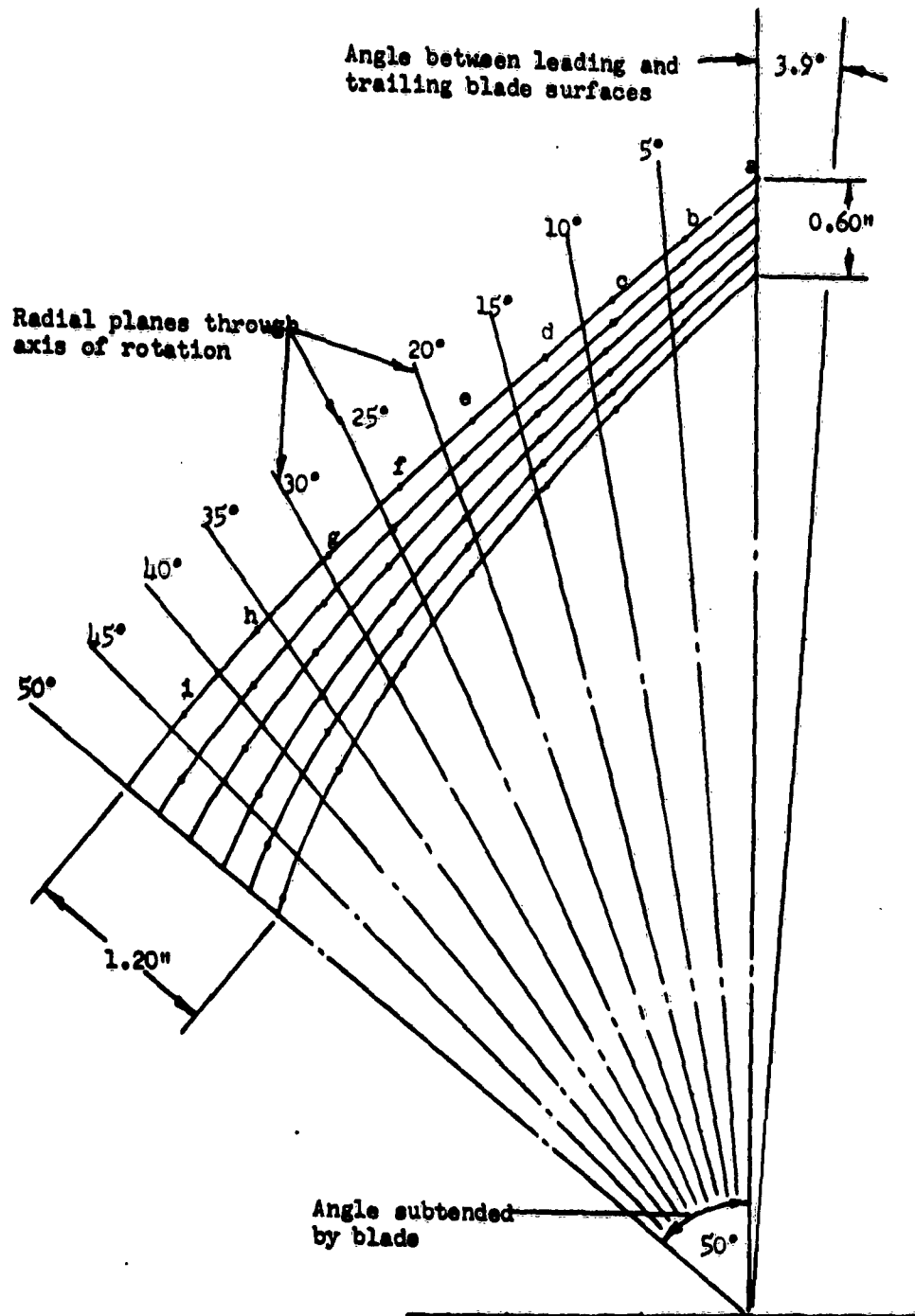
$$\cot\beta = \frac{1}{\frac{c_m}{Q/D^2}} \left[\frac{R}{Q/\omega D^3} - \frac{mD/Q}{R} \right]. \quad (34)$$

The dimensionless meridional velocity component is taken from Fig. 5, and the whirl-moment from Fig. 6. The details of the design procedure are progressively shown in Fig. 7, and the numerical values for the computation are given in Table II. The constant incremental arc lengths δs along each meridional streamline are shown in Fig. 7a. The corresponding computed values of $\delta\theta$ are used to determine the streamlines, shown in the

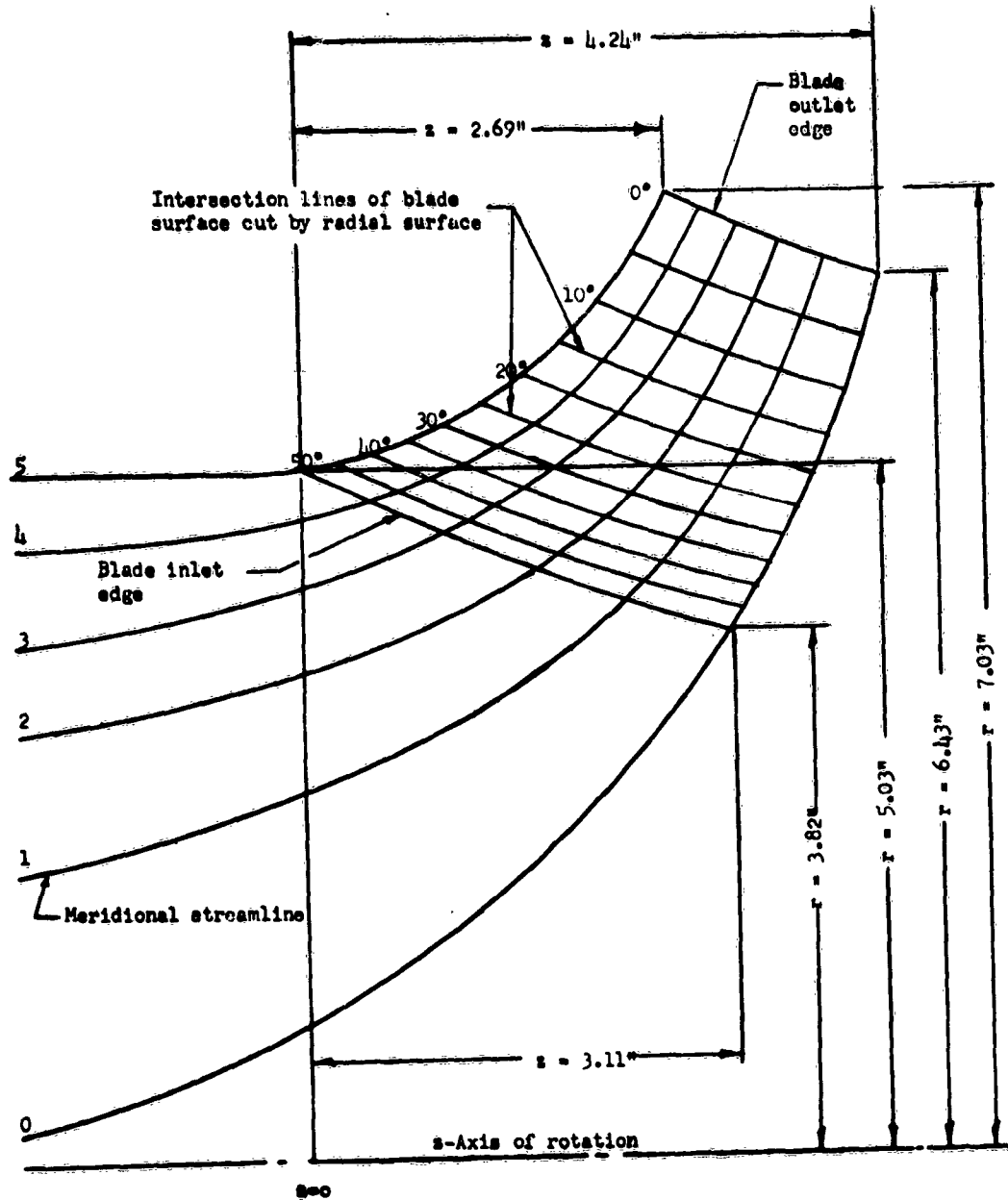


(a) Construction of Points Displaced from Blade Outlet Edge A Constant Arc-Distance Along Meridional Streamlines

Fig. 7 GRAPHICAL BLADE DESIGN PROCEDURE



(b) Plan View of Meridional Streamlines and Radial Planes
 Fig. 7 (Continued) GRAPHICAL BLADE DESIGN PROCEDURE



(c) Radially Cut Blade Intersection Lines

Fig. 7 (Concluded) GRAPHICAL BLADE DESIGN PROCEDURE

Table II

BLADE DESIGN FOR DESIGN PARAMETER, $\frac{Q}{\omega D^3} = 0.060$

	STATION	Meridian Distance S = s/D	Radial Distance R = r/D	Meridian Velocity $\frac{c_m}{Q/D^2}$	Angular Position θ (degree)	Whirl Moment $\frac{mD}{Q}$	δS	$\delta \theta$ (deg)	Cot β	Blade Angle β (deg)	
Streamline 0	a	0	0.458	2.47	0	2.21	0.028	4.00	1.15	41.0	
	b	0.028	0.431	2.47	4.00	1.80	0.028	4.54	1.22	39.3	
	c	0.056	0.404	2.46	8.54	1.40	0.028	5.27	1.33	36.9	
	d	0.084	0.378	2.44	13.8	1.03	0.028	6.2	1.47	34.3	
	e	0.112	0.352	2.41	20.0	0.69	0.028	7.4	1.63	31.5	
	f	0.140	0.326	2.39	27.4	0.40	0.028	8.7	1.76	29.5	
	g	0.168	0.301	2.37	36.1	0.16	0.028	10.1	1.90	27.8	
	h	0.196	0.277	2.33	46.2	0.02	0.028	11.3	1.95	27.1	
	i	0.224	0.254	2.29	57.5	0	-	-	-	-	
	Streamline 1	a	0	0.466	2.59	0	2.21	0.028	4.02	1.168	40.6
		b	0.028	0.438	2.59	4.02	1.80	0.028	4.51	1.232	39.1
c		0.056	0.413	2.58	8.53	1.40	0.028	5.26	1.354	36.4	
d		0.084	0.388	2.58	13.8	1.03	0.028	6.11	1.478	34.1	
e		0.112	0.362	2.57	19.9	0.69	0.028	7.12	1.606	31.9	
f		0.140	0.339	2.56	27.0	0.41	0.028	8.21	1.735	30.0	
g		0.168	0.317	2.54	35.2	0.18	0.028	9.39	1.856	28.3	
h		0.196	0.296	2.53	44.6	0.035	0.028	10.31	1.903	27.7	
i		0.224	0.276	2.51	54.9	0	-	-	-	-	
Streamline 2		a	0	0.474	2.72	0	2.21	0.028	4.03	1.190	40.0
		b	0.028	0.447	2.73	4.03	1.80	0.028	4.50	1.254	38.6
	c	0.056	0.421	2.74	8.53	1.40	0.028	5.13	1.347	36.6	
	d	0.084	0.397	2.74	13.7	1.04	0.028	5.89	1.459	34.4	
	e	0.112	0.374	2.75	19.6	0.71	0.028	6.76	1.576	32.4	
	f	0.140	0.353	2.75	26.4	0.43	0.028	7.71	1.696	30.5	
	g	0.168	0.332	2.74	34.1	0.21	0.028	8.64	1.788	29.2	
	h	0.196	0.313	2.73	42.7	0.05	0.028	9.49	1.852	28.4	
	i	0.224	0.296	2.71	52.2	0	-	-	-	-	
	Streamline 3	a	0	0.483	2.90	0	2.21	0.028	3.98	1.198	39.9
		b	0.028	0.457	2.91	3.98	1.81	0.028	4.41	1.256	38.5
c		0.056	0.433	2.92	8.39	1.41	0.028	5.03	1.357	36.4	
d		0.084	0.410	2.93	13.4	1.05	0.028	5.70	1.458	34.4	
e		0.112	0.388	2.93	19.1	0.74	0.028	6.43	1.556	32.7	
f		0.140	0.368	2.92	25.5	0.47	0.028	7.25	1.663	31.0	
g		0.168	0.349	2.92	32.8	0.24	0.028	8.08	1.757	29.7	
h		0.196	0.332	2.90	40.9	0.08	0.028	8.82	1.825	28.7	
i		0.224	0.320	2.87	49.7	0.003	0.028	9.30	1.855	28.3	
Streamline 4		a	0	0.491	3.07	0	2.21	0.028	3.92	1.199	39.8
		b	0.028	0.463	3.09	3.92	1.81	0.028	4.27	1.232	39.1
	c	0.056	0.442	3.11	8.19	1.43	0.028	4.82	1.329	37.0	
	d	0.084	0.423	3.13	13.0	1.08	0.028	5.45	1.437	34.8	
	e	0.112	0.400	3.14	18.5	0.77	0.028	6.06	1.510	33.5	
	f	0.140	0.382	3.15	24.6	0.50	0.028	6.74	1.606	31.9	
	g	0.168	0.365	3.14	31.3	0.28	0.028	7.44	1.693	30.6	
	h	0.196	0.352	3.12	38.7	0.11	0.028	8.11	1.780	29.3	
	i	0.224	0.341	3.10	46.8	0.02	0.028	8.53	1.814	28.9	
	Streamline 5	a	0	0.500	3.26	0	2.21	0.028	3.85	1.200	39.8
		b	0.028	0.476	3.30	3.85	1.82	0.028	4.20	1.245	38.8
c		0.056	0.452	3.34	8.05	1.44	0.028	4.62	1.301	37.5	
d		0.084	0.430	3.39	12.7	1.10	0.028	5.07	1.360	36.3	
e		0.112	0.413	3.42	17.8	0.80	0.028	5.62	1.446	34.7	
f		0.140	0.395	3.43	23.4	0.55	0.028	6.14	1.513	33.5	
g		0.168	0.381	3.42	29.5	0.33	0.028	6.75	1.604	31.9	
h		0.196	0.370	3.39	36.2	0.16	0.028	7.34	1.692	30.6	
i		0.224	0.362	3.34	43.5	0.045	0.028	7.84	1.769	29.5	

Table III

CYLINDRICAL COORDINATES OF STREAMLINES ON FRONT AND BACK VANE SURFACES

θ	Streamline Number												
	0		1		2		3		4		5		
	r	z	r	z	r	z	r	z	r	z	r	z	
0	Back Vane Surface												
0	356.1	4.240	6.535	3.850	6.645	3.520	6.770	3.215	6.900	2.945	7.030	2.685	
5	1.1	4.120	6.090	3.690	6.205	3.340	6.340	3.000	6.450	2.720	6.580	2.430	
10	6.1	3.985	5.720	3.535	5.830	3.160	5.970	2.790	6.080	2.475	6.220	2.170	
15	11.1	3.855	5.390	3.380	5.520	2.980	5.670	2.565	5.790	2.215	5.920	1.880	
20	16.1	3.740	5.120	3.235	5.265	2.810	5.420	2.355	5.550	1.970	5.690	1.590	
25	21.1	3.625	4.875	3.080	5.030	2.630	5.205	2.140	5.340	1.715	5.500	1.310	
30	26.1	3.520	4.675	2.950	4.830	2.465	5.020	1.945	5.180	1.480	5.355	1.025	
35	31.1	3.410	4.490	2.800	4.655	2.290	4.855	1.740	5.035	1.255	5.235	0.780	
40	36.1	3.310	4.325	2.660	4.500	2.120	4.715	1.540	4.920	1.030	5.140	0.520	
45	41.1	3.210	4.180	2.530	4.370	1.960	4.605	1.350	4.825	0.810	5.065	0.260	
50	46.1	3.110	4.035	2.390	4.245	1.780	4.510	1.155	4.760	0.580	5.030	0	

plan view of Fig. 7b. Starting from the blade outlet edge, radial planes are drawn in the plan view at 5 degree intervals up to the inlet blade edge, spanning a total angular displacement of 50 degrees. The intersection points of the meridional streamlines with these radial planes are plotted in Fig. 7c, and these points determine the intersection lines of the blade surface with the radial planes. As previously described, these intersection lines are lines of constant whirl-moment, and, consequently, indicate lines of constant energy input to the fluid from the blade cascade. The cylindrical coordinates of the blade surface are measured directly from these intersection lines and are presented in Table III. Templates designed according to the data of Table III were used to guide the construction of the pattern for the impeller casting.

C. Finite Number of Blades

1. General Considerations

The design of the experimental impeller is based upon flow conditions through a cascade with an infinite number of blades. Ruden³ has computed the potential through-flow for a cascade having a finite number of blades by considering the velocity at every point to be the sum of the average value with respect to θ plus a perturbation velocity. He showed that if perturbations of an order higher than the first are neglected, the average meridional values with respect to θ are exactly equal to the values computed on the basis of an infinite number of blades. In general practice, this condition is considered to be satisfied if the blades are not spaced too widely apart, the fluid is of low viscosity, and the operating conditions are near the design point. One of the ob-

objectives of the experimental phase of this program is to determine the extent to which the flow deviates from the theoretically predicted flow for an infinite number of blades. Assuming a uniform flow distribution from hub to shroud, Stanitz^{4,5} has computed the blade-to-blade variation in the flow through a conical, mixed-flow compressor by the relaxation method. He has also computed the flow on a general mean stream surface of revolution for a compressor having straight radial blades. Following the methods of Stanitz, the theoretical variation of the flow between the blades of the experimental impeller has been computed at the design operating condition $Q/\omega D^3 = 0.060$, for comparison with experiments and evaluation of the underlying potential flow assumptions.

Because of the small blade number (four) of the experimental impeller, the maximum deviation from the mean flow conditions are expected to occur in the tangential direction. The spacing between the hub and shroud surfaces is relatively small compared to the spacing between the blades; thus, it is assumed that the deviation of the meridional streamline pattern from the axial-symmetry solution is small. Further, at the design condition, the tangential component of the bound vortex-sheets representing the blade surface has been assumed to be zero, so that from the infinite-blade considerations the meridional streamline pattern should remain undisturbed. For these reasons, the flow is assumed to proceed along the surfaces of revolution generated by the meridional streamlines. This assumption does not allow a true, three-dimensional motion, since the fluid particles are thus hypothetically confined to predetermined surfaces of revolution. The quasi-three-dimensional solution so obtained, however, should give a more realistic picture of the flow conditions within the

impeller than would the axial-symmetry solution.

2. Equation of Fluid Motion on the Mean Meridional Stream Surface

a. Absolute Irrotational Motion

The general differential equation of the fluid motion is derived under the assumption that the flow is confined within a channel formed by two stream surfaces of revolution enclosing the stream surface generated by the mean meridional streamline as shown in Fig. 8. The flow is assumed to be irrotational upstream of the blade cascade, and according to the discussion immediately following equation (12), the absolute velocity of the fluid will remain irrotational upon passing through the impeller. In particular, the vorticity component normal to the stream surface is zero, implying the circulation on any closed path on the stream surface between the blades is zero (Stokes' theorem). Considering the path shown in Fig. 9, the following equation is obtained,

$$\lambda_n = 0 = \frac{1}{R \delta \sin \delta} \left[\frac{\partial}{\partial R} (C_t R \, d\theta) dR - \frac{\partial}{\partial \theta} (C_m \, dS) d\theta \right]. \quad (35)$$

Since $\sin \delta = dR/dS$, this equation may be simplified,

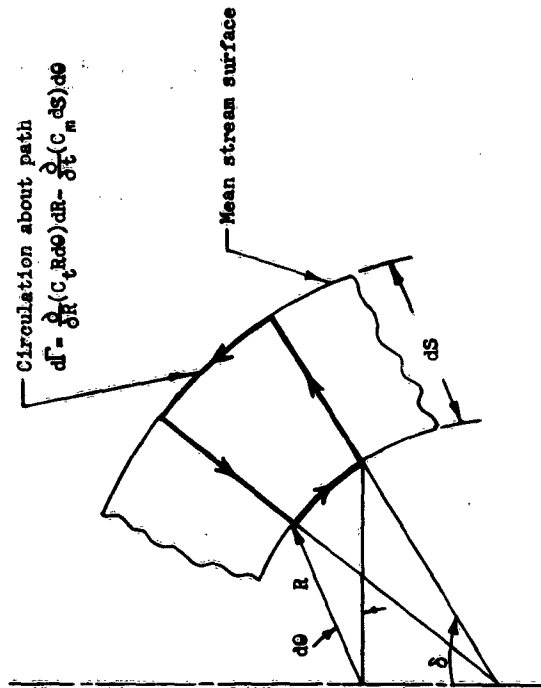
$$\begin{aligned} 0 &= \frac{\partial}{\partial R} (R C_t) - \frac{1}{\sin \delta} \frac{\partial C_m}{\partial \theta} \\ &= \frac{\partial}{\partial R} [R(2R + W_t)] - \frac{1}{\sin \delta} \frac{\partial W_m}{\partial \theta}; \end{aligned}$$

and, expanding this equation gives

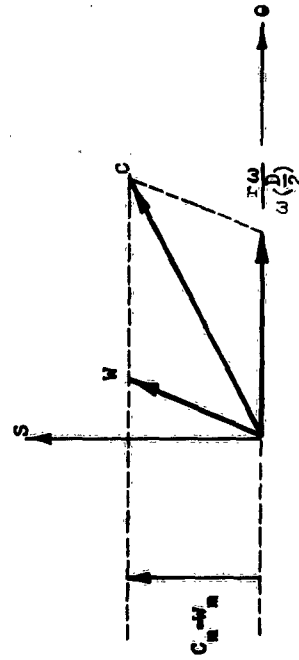
$$4R \sin \delta + W_t \sin \delta + R \sin \delta \frac{\partial W_t}{\partial R} - \frac{\partial W_m}{\partial \theta} = 0. \quad (36)$$

b. Continuity Equation

The application of continuity conditions to the elemental



(a) Elemental Circulation



(b) Velocity Diagram

Fig. 9 CIRCULATION AND VELOCITY DIAGRAM ON MEAN STREAM SURFACE

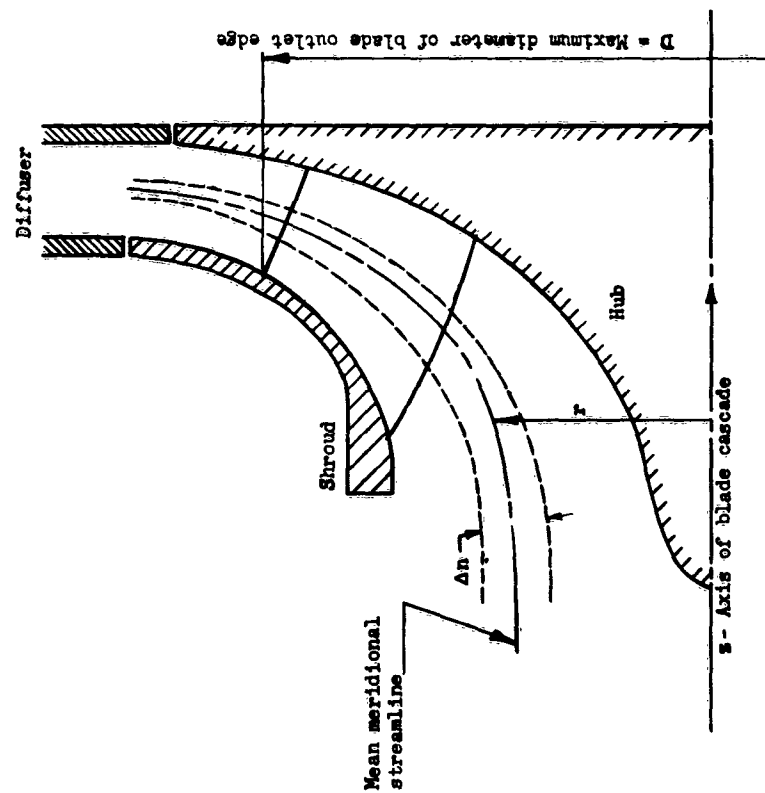


Fig. 8 MEAN STREAM SURFACE OF REVOLUTION FOR AXIAL SYMMETRY CONDITIONS

region shown in Fig. 10 yields the following equation,

$$0 = \frac{\partial}{\partial R} (W_m BR d\theta) dR + \frac{\partial}{\partial \theta} (W_t B dS) d\theta ;$$

and, since $dR/dS = \sin \delta$, there is obtained the equation

$$\frac{\partial}{\partial R} (W_m BR) + \frac{\partial}{\partial \theta} (W_t \frac{B}{\sin \delta}) = 0 . \quad (37)$$

A stream function ψ , satisfying equation (37), may be defined such that

$$\frac{\partial \psi}{\partial R} = - W_t \frac{B}{\sin \delta} , \quad (38a)$$

$$\frac{\partial \psi}{\partial \theta} = W_m BR . \quad (38b)$$

Coordinates (ξ, η) , introduced by Stanits⁴, on the mean stream surface are defined such that

$$\frac{d\eta}{d\theta} = \frac{1}{\Delta \theta} , \quad (39a)$$

$$\frac{d\xi}{dR} = \frac{1}{R \Delta \theta \sin \delta} . \quad (39b)$$

Since the Cauchy-Riemann equations are satisfied, the transformation of coordinates (R, θ) from the mean stream surface to the (ξ, η) plane is conformal; that is,

$$\frac{\partial \xi}{\partial S} = \frac{1}{R} \frac{\partial \eta}{\partial \theta} , \quad (40a)$$

$$\frac{1}{R} \frac{\partial \xi}{\partial \theta} = - \frac{\partial \eta}{\partial S} . \quad (40b)$$

In the transformed plane, equation (36) becomes

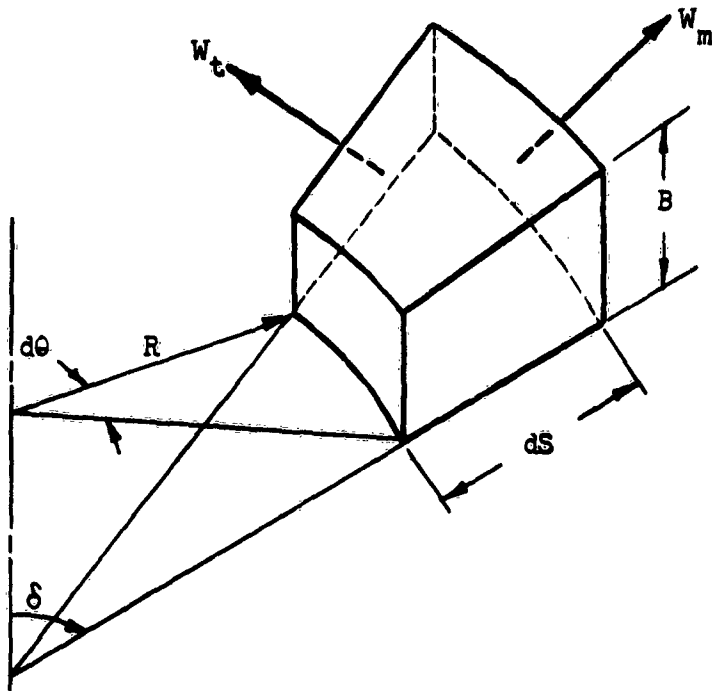


Fig. 10 ELEMENTAL REGION FOR APPLICATION OF CONTINUITY EQUATION

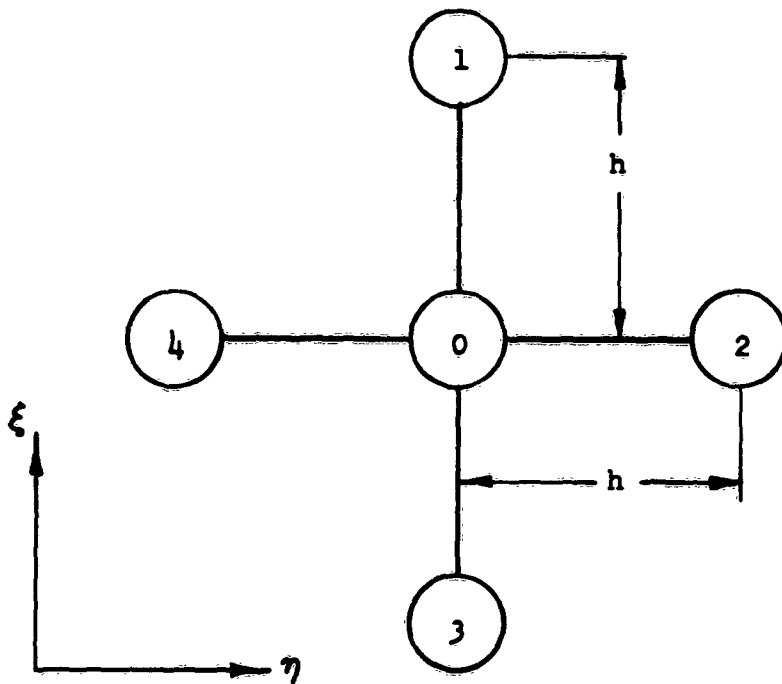


Fig. 11 MESH NOTATION ABOUT CENTRAL POINT O

$$4R \sin \delta + W_t \sin \delta + \frac{1}{\Delta \theta} \frac{\partial W_t}{\partial \xi} - \frac{1}{\Delta \theta} \frac{\partial W_m}{\partial \eta} = 0, \quad (41)$$

and the equations for the stream function become.

$$\frac{\partial \psi}{\partial \xi} = -W_t \text{ER} \Delta \theta, \quad (42a)$$

$$\frac{\partial \psi}{\partial \eta} = W_m \text{ER} \Delta \theta. \quad (42b)$$

c. General Equation

Combining the stream-function equations (42), and equation (41), the equation given by Stanitz is obtained,

$$\frac{\partial^2 \psi}{\partial \xi^2} + \frac{\partial^2 \psi}{\partial \eta^2} - \frac{d \ln B}{d \xi} \frac{\partial \psi}{\partial \xi} - 4 \text{ER}^2 (\Delta \theta)^2 \sin \delta = 0. \quad (43)$$

Using the notations shown in Fig. 11, equation (43) may be expressed in finite-difference form,

$$\psi_1 + \psi_2 + \psi_3 + \psi_4 - 4 \psi_0 + h f(\xi_0)(\psi_1 - \psi_3) - h^2 g(\xi_0) = 0, \quad (44)$$

where

$$f(\xi_0) = -\frac{1}{2} \left(\frac{d \ln B}{d \xi} \right)_0, \quad (45)$$

$$g(\xi_0) = 4 \left[\text{ER}^2 (\Delta \theta)^2 \sin \delta \right]_0. \quad (46)$$

The values of ξ as a function of R are determined from a numerical evaluation of the integral

$$\xi = \frac{1}{\Delta \theta} \int_{R_{\text{blade exit}}}^R \frac{1}{R \sin \delta} dR \quad (47)$$

The plot of the mean meridional streamline and the channel height B are

shown in Fig. 12. The cone angle δ is determined from the slope of the mean meridional streamline with respect to the axis of rotation,

$$\delta = \text{arc tan } \frac{dR}{dz}, \quad (48)$$

and the values of $\sin \delta$ are plotted in Fig. 13. The values of ξ obtained by the numerical integration of equation (47) are shown in Fig. 13, and the function $\ln B$, together with its derivative, is shown in Fig. 14. The θ -coordinates of the blade profile on the mean stream surface are shown in Fig. 12, and the corresponding η -coordinates are plotted in Fig. 13. The numerical values are presented in Table IV.

d. Boundary Conditions

The assumed boundary conditions that make the problem completely determinate can be summarized by the following four conditions.

1. The specified inlet flow is uniform far upstream.
2. The Kutta-Joukowski condition applies at the blade exit tip.
3. Periodic flow conditions prevail about the impeller axis, with a period equal to the blade number.
4. The flow is uniform far downstream of the blade cascade.

The flow conditions in the draft-tube upstream of the blade cascade are considered uniform at $\xi = -1.10$. Velocity traverses made during the test runs showed this assumption to be essentially correct. For this value of ξ , the radius R is 0.250, and the channel height B is 2.00. The meridional component of the upstream velocity is given by the

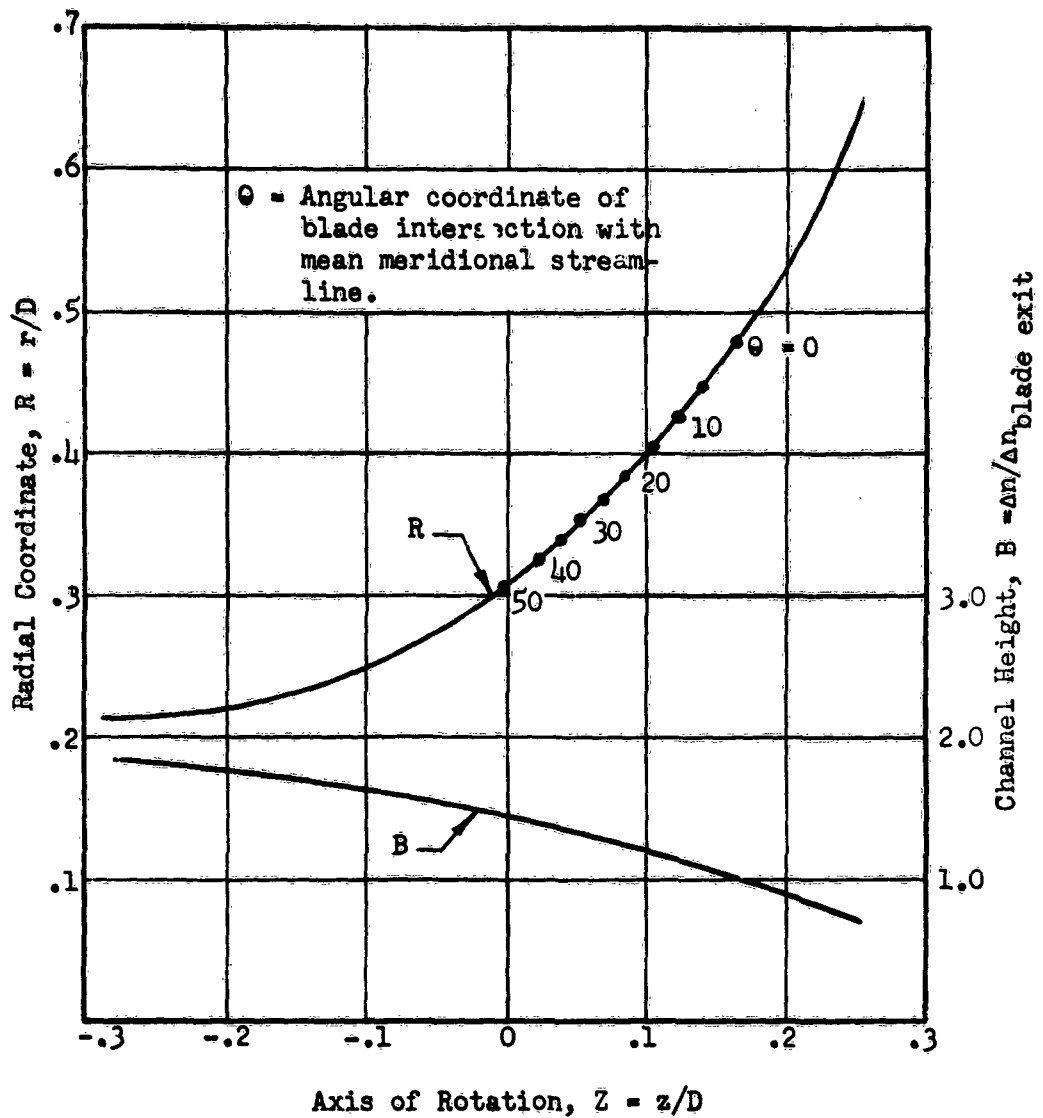


Fig. 12 MEAN MERIDIONAL STREAMLINE COORDINATES AND CHANNEL HEIGHT

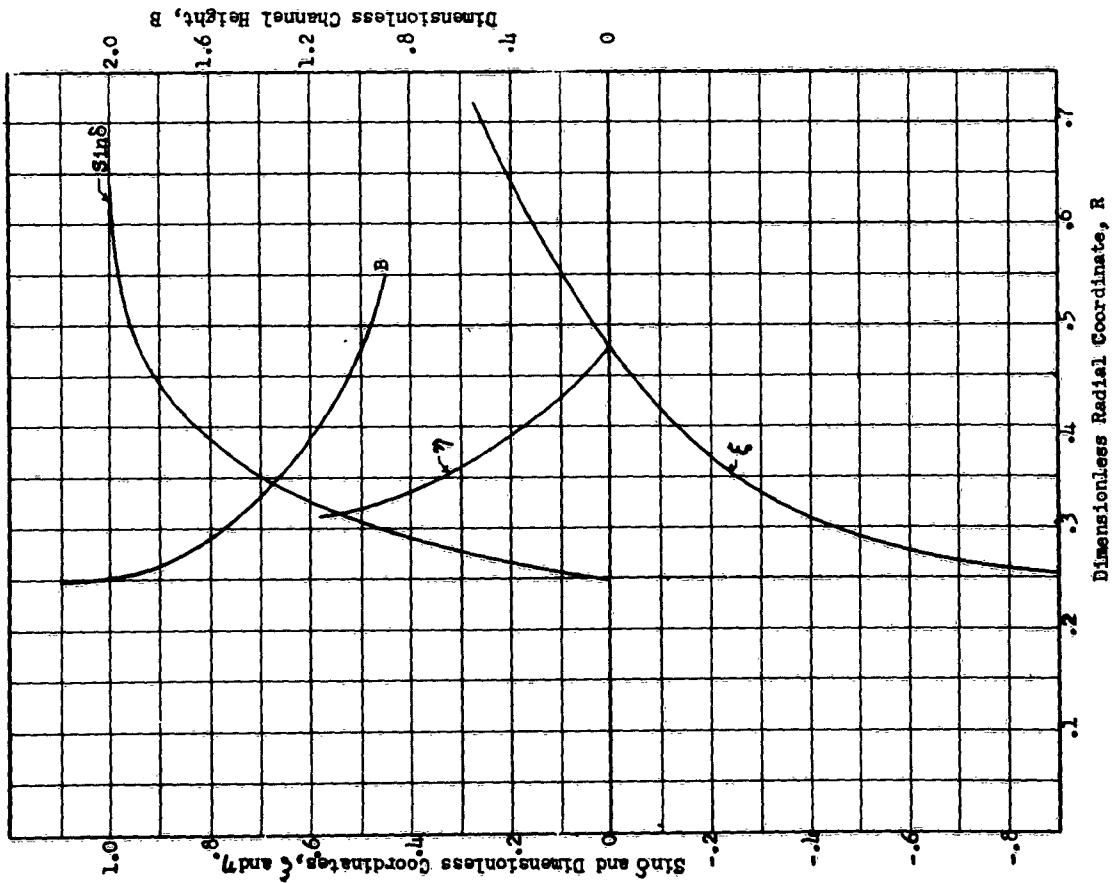


Fig. 13 VARIATION OF ξ , B , AND $\text{SIN } \delta$ WITH THE RADIAL COORDINATE.

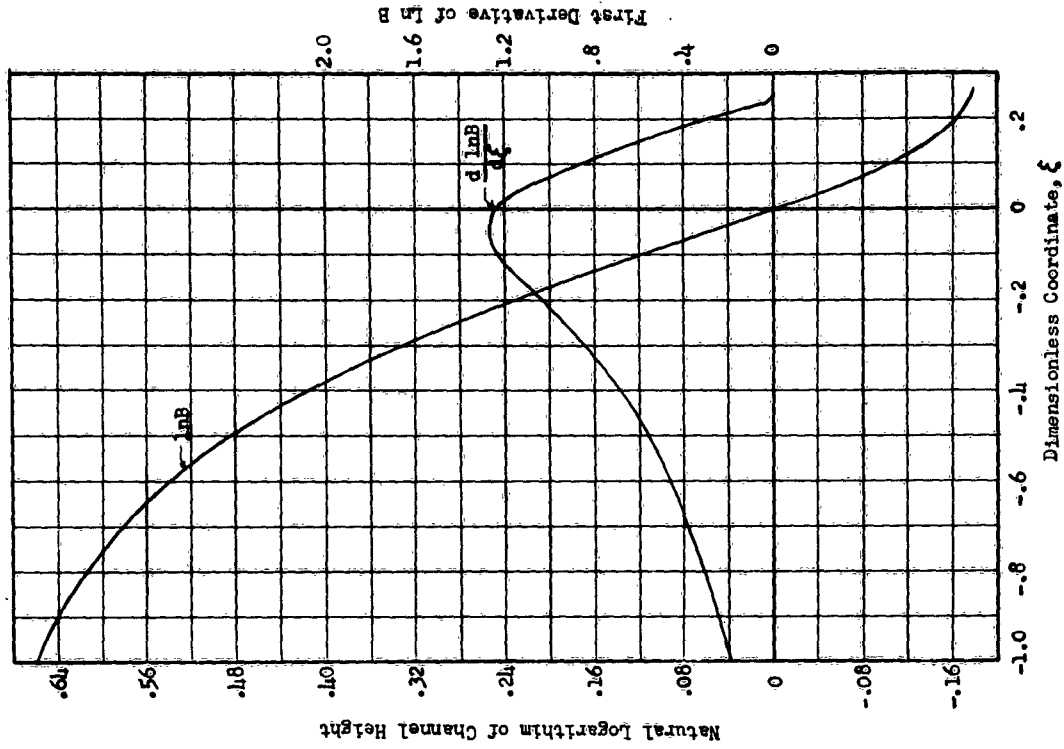


Fig. 14 CURVES FOR DETERMINATION OF THE FUNCTION, $f(\xi_0) = -\frac{1}{2} \frac{d \ln B}{d \xi}$

Table IV

MEAN STREAM SURFACE DATA

ξ	R	B	$\sin \delta$	$f(\xi_0)$	$g(\xi_0)$ ($\theta=1.502$)	η^* (Blade Profile)
- 1.10	0.250	2.00	0	0	0	
- 1.00	0.253	1.95	0.065	0.0925	0.0748	
- 0.90	0.255	1.89	0.093	0.1225	0.1032	
- 0.80	0.258	1.85	0.125	0.1540	0.1389	
- 0.70	0.265	1.78	0.187	0.1895	0.2109	
- 0.60	0.274	1.71	0.265	0.2320	0.3070	
- 0.50	0.287	1.62	0.365	0.2830	0.4395	
- 0.40	0.306	1.52	0.490	0.3440	0.6295	
- 0.30	0.331	1.39	0.620	0.4195	0.8518	0.430
- 0.20	0.367	1.26	0.748	0.5125	1.1456	0.270
- 0.10	0.416	1.12	0.860	0.6085	1.5047	0.122
- 0.05	0.446	1.06	0.907	0.6300	1.7258	0.060
0	0.477	1.00	0.942	0.6140	1.9333	0
0.05	0.514	0.94	0.968	0.5410	2.1687	
0.10	0.551	0.90	0.982	0.4330	2.4209	
0.15	0.596	0.87	0.995	0.3075	2.7745	
0.20	0.641	0.85	1.000	0.1600	3.1514	
0.25	0.691	0.84	1.000	0.0000	3.6193	
0.30	0.745	0.84	1.000	0.0000	4.2071	

*At the blade inlet tip, $\eta = 0.581$ at $\xi = -0.383$

total volume rate of flow divided by the draft-tube area,

$$w_m = \frac{Q}{\pi r_{\text{draft}}^2} \quad (49)$$

The dimensionless velocity is

$$W_m = \frac{w_m}{\omega D/2} = \frac{Q}{\omega D^3} \frac{2}{\pi R^2 \text{draft}} \quad (49a)$$

The dimensionless draft-tube radius is 0.355, and at the design point, $Q/\omega D^3 = 0.060$; so that the meridional velocity component of the uniform upstream flow, as computed from equation (49a) is 0.303. Considering the upstream whirl-moment in the draft-tube to be zero, the tangential component of the absolute velocity is given by

$$c_t = u + w_t = 0,$$

and

$$w_t = -u = -r\omega.$$

The dimensionless relative velocity component is thus

$$\begin{aligned} W_t &= -\frac{r\omega}{\omega D/2} = -2R \\ &= 2(0.250) = -0.500 . \end{aligned}$$

The derivatives of the stream function are

$$\begin{aligned} \frac{\partial \psi}{\partial \xi} &= -W_t BR \Delta \theta \\ &= -(-0.500)(2.00)(0.250)(1.502) = 0.376, \end{aligned}$$

$$\begin{aligned} \frac{\partial \psi}{\partial \eta} &= W_m BR \Delta \theta \\ &= (0.303)(2.00)(0.250)(1.502) = 0.2276 . \end{aligned}$$

The span between blades is $\Delta\eta = 1$, and consequently, $\Delta\Psi = 0.2276$. For convenience, a stream-function Ψ may be defined such that

$$\Psi = 100 \frac{\psi}{\Delta\Psi} . \quad (50)$$

The value of Ψ on the leading face of the blade profile is made equal to zero, and on the trailing face a value of 100 is chosen. The specified values of the derivatives of the stream-function on the upstream boundary are shown in Fig. 15.

The Kutta-Joukowski condition requires that the relative flow leaves the blade tip tangent to the blade surface. The best numerical procedure to follow is to satisfy all boundary conditions with the exception of the Kutta condition in the first relaxation solution, and then adjust the downstream whirl-moment value until the tangency condition is satisfied. The adjustment of the downstream whirl-moment value is determined by a separate relaxation solution involving fixed zero-values of the stream-function on the blades and a unit change in the upstream whirl-moment value. The corresponding changes in the stream-function are determined to a first approximation by the relaxation solution of the Laplace equation,

$$\nabla^2\Psi = 0, \quad (51)$$

and, in accordance with these values, the stream-function is adjusted to satisfy the Kutta condition. A final computation must then be made to satisfy the more accurate differential equation (43). The details of this computation are presented in Appendix C.

From symmetry considerations, the flow is cyclic in the η -direction with a period equal to the blade spacing, $\Delta\eta = 1$. Periodic

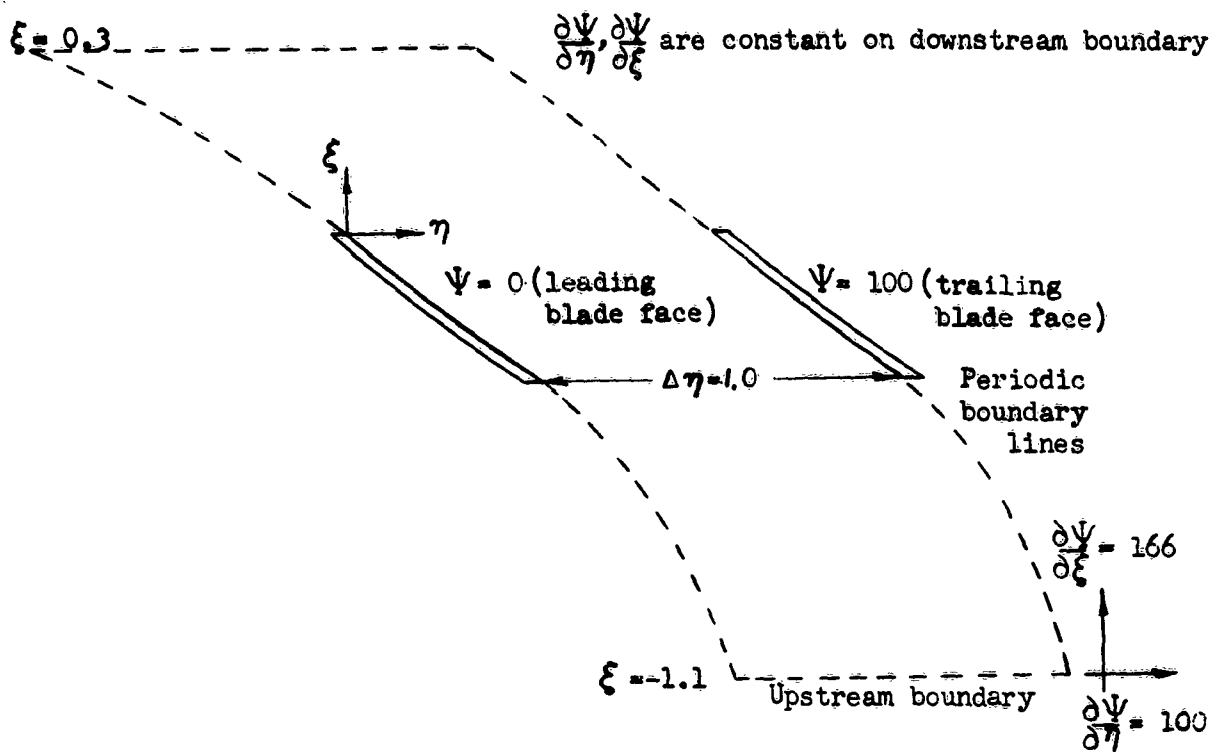


Fig. 15 BOUNDARY CONDITIONS FOR THE FLOW FIELD ON THE MEAN STREAM SURFACE.

boundary lines are sketched in as shown in Fig. 15, and for any given value of ξ , the value of the stream-function on the right-hand boundary line must equal the value on the left-hand boundary line plus 100.

The flow conditions are considered to become uniform downstream in the vaneless diffuser, so that the derivatives of the stream-function, shown in Fig. 15, are constant on the downstream boundary.

The flow conditions around the boundaries enclosing the flow region have now been completely described, and the problem can be solved by relaxation methods. A discussion of the results of this computation at the design condition follows.

3. Results of the Relaxation Solution

After the residuals occurring in the relaxation solution have been eliminated, the values of the stream function at the nodes of the relaxation grid are used to determine the relative streamlines. A streamline is a line drawn smoothly through common values of the stream function as is shown in Fig. 16. For any streamline, the numerical value of Ψ indicates the quantity of flow, passing between the contour line of the leading blade face and the specified streamline, as a percentage of the total flow passing between the two blades. From the distribution of the stream-function along the periphery at the blade exit-tip, the meridional velocity distribution is computed by means of equation (42b). The velocity distribution computed on this basis is compared, in Chapter IV, with the distribution measured at various operating conditions of the test impeller.

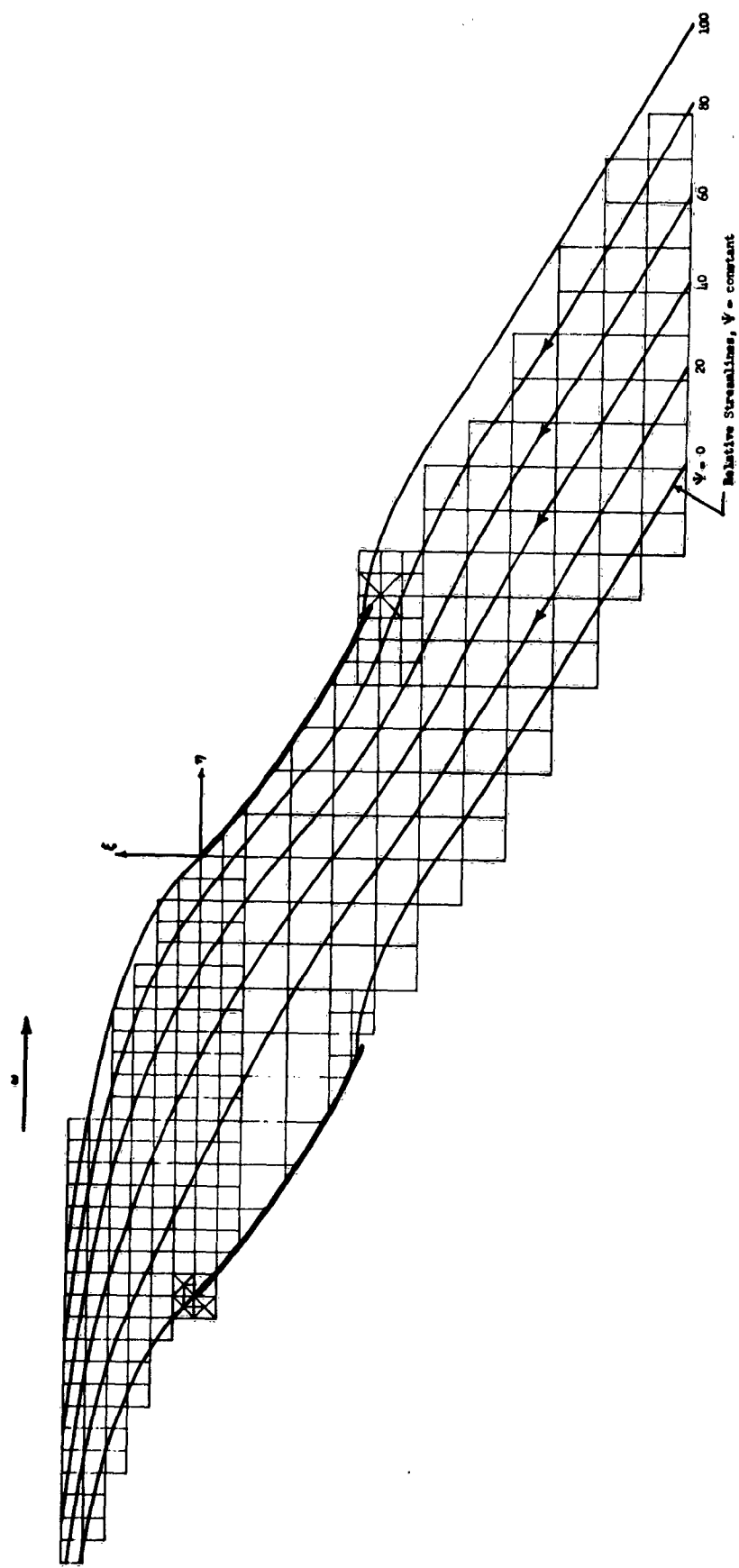


Fig. 16 Relative Streamlines at the Design Conditions

III. EXPERIMENTAL INVESTIGATION

A. Description of the Test Stand

A schematic diagram of the test stand used in this investigation is shown in Fig. 17, and the complete test stand with the dynamometer drive is shown in the photograph of Fig. 18. The dynamometer unit has a 20 horsepower rating and a speed range from 400 to 6000 rpm. A large, box-type filter is provided upstream of the inlet nozzle to prevent damage and clogging of the instruments. The filter consists of flannel cloth supported by wire mesh screening, and has static pressure taps at the walls of the box to measure the pressure drop across the filter. A standard A.S.M.E. long-radius nozzle is installed at the inlet of the draft tube to measure the rate of flow, and to provide smooth entry of the air. Six straightening vanes are mounted in the nozzle (Fig. 19), and extend from the inlet face to the end of the long radius.

The impeller is cast of an aluminum alloy and has a maximum blade diameter of 14.06 inch (see Figs. 20 and 21). The details of the impeller design have been described in Section II. An aluminum disc is mounted on the back of the impeller to support the pitot probe, which can be located in six different peripheral positions relative to the impeller. An adjustable dummy pitot-probe is provided diametrically opposite the actual probe to minimize the dynamic unbalance of the unit. The impeller and the positioning disc were each dynamically balanced so that the unit remains in dynamic balance even though the location of the positioning disc is changed relative to the impeller. The ring arrangement shown on the back of the positioning disc is to support the stainless-steel tubing which

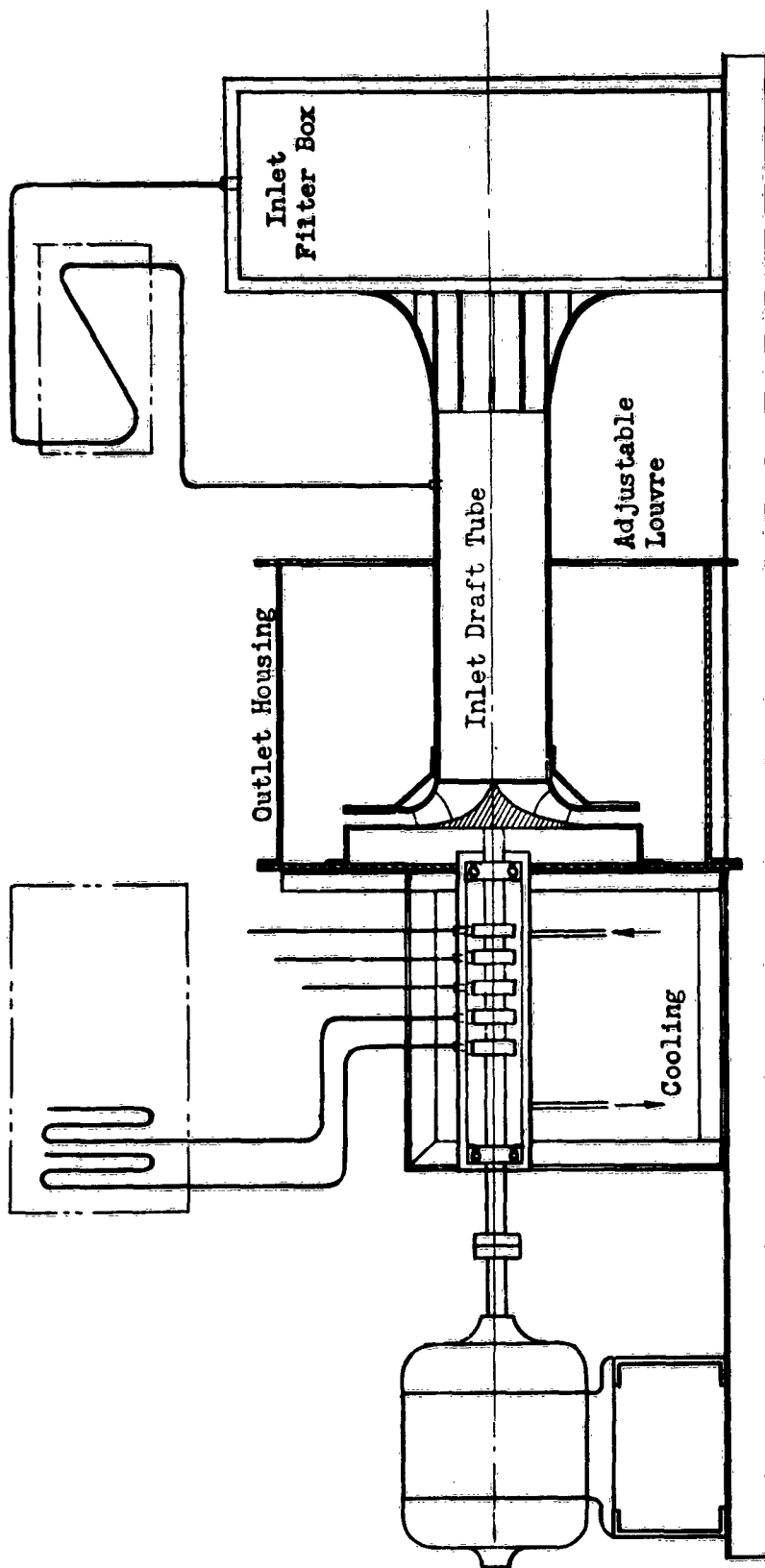


Fig. 17 SCHEMATIC DIAGRAM OF THE TEST STAND



Fig. 18 TEST STAND AND DYNAMOMETER UNIT



Fig. 19 INLET NOZZLE AND STRAIGHTENING VANES

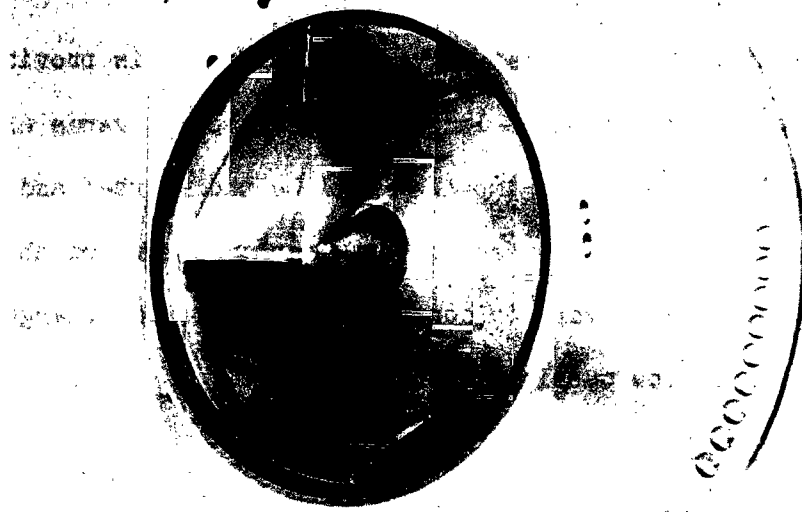


Fig. 20 FRONT VIEW OF IMPELLER

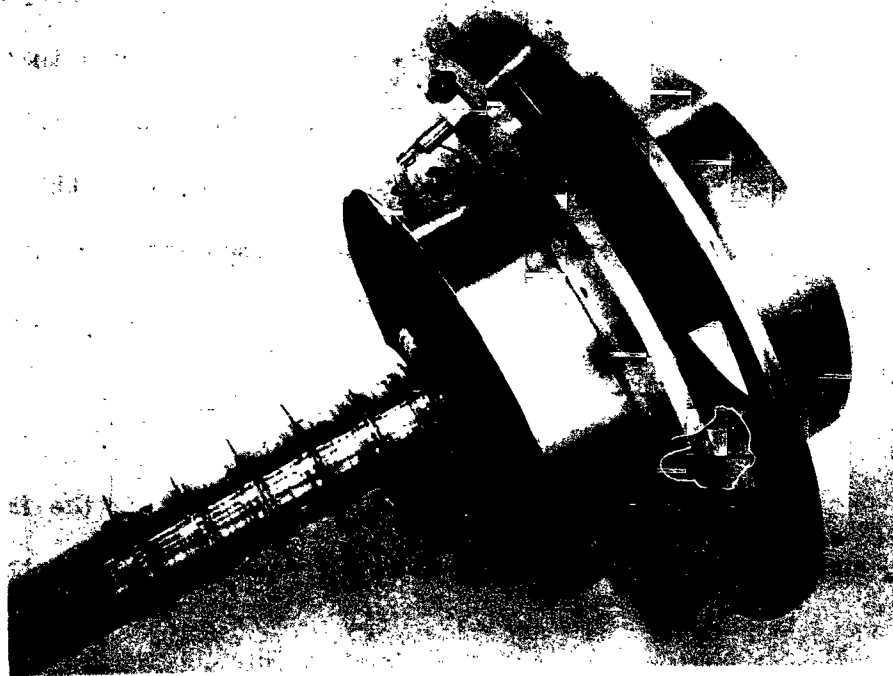


Fig. 21 IMPELLER WITH SPHERICAL PITOT-PROBE MOUNTED ON POSITIONING DISC

leads from the pitot-probe to the shaft, against centrifugal force effects. The tubing is connected to longitudinal holes which are drilled in the shaft and lead to the rotary-seal pressure take-offs.

At the exit of the impeller, a vaneless diffuser is provided which consists of two parallel plates of large diameter. Guide vanes are omitted so that the relative flow in the impeller will be undisturbed and steady. The flow leaving the diffuser, passes into a discharge drum which is equipped with adjustable louvers to control the impeller discharge pressure and the total rate of flow passing through the unit.

B. Instrumentation

1. Inlet Conditions

The total volume rate of flow entering the draft tube is measured with a standard A.S.M.E. long-radius nozzle. The static pressure taps are in the parallel throat portion at the recommended distance from the inlet face. Values of the nozzle coefficient for a range of throat Reynolds numbers are provided in the A.S.M.E. Fluid Meters Report.

Conditions downstream of the straightening vanes in the nozzle are measured by means of a pitot-traverse taken with a spherical probe. Pre-rotation of the flow could not be detected, either with the pitot-traverse, or by visual observation using small flags inserted into the flow stream.

2. Outlet Conditions

a. Preliminary Considerations

The absolute velocity of the fluid leaving the impeller is unsteady, and it varies periodically with a frequency given by the product

of the blade number and the impeller rotative speed. Because of the errors produced by pressure waves and high fluid resistance in the tubing connecting the probe and the pressure pickup, accurate measurement of the absolute velocity (and pressure) distribution by means of stationary total pressure probes is considered impractical. There are pressure-sensitive electronic instruments commercially available which are highly responsive, but an accurate measurement of the direction of the unsteady absolute flow is considered unfeasible using any type of total pressure probe presently available; extreme sensitivity would be required of the instrument, particularly at low flows, and very small size would be necessary to eliminate disturbances. Studies of incompressible liquid flow in pumps have been successfully made using an intercepting valve, rather than an instrument recording a continuous pressure measurement with time. In this method, pressure impulses of very short duration are intercepted and measured at intervals synchronized with the impeller rotation; and, by varying the phase of interception, a series of pressure impulses can be plotted as a continuous curve. At the greater impeller speeds, serious objections to this method are raised because there is hardly any means of actuating the intercepting valve fast enough to transmit pressure impulses within small phase angles.

A possible alternate method of measuring the unsteady absolute velocity is by means of the hot-wire anemometer. As a preliminary study, small hot-wire probes were made with 0.045 inch lengths of 0.0003 inch diameter tungsten wire and were calibrated in a steady flow stream. Difficulty was encountered because of the rather low sensitivity

of the hot-wire, when used as a constant-current instrument, at air velocities over 140 fps. Greater sensitivity could be obtained by increasing the current, but at the risk of burning out the wire; a 100 milliamp current was considered to be the maximum safe operating limit. It was decided that this instrument was not practical to use for accurate quantitative measurements in the range of air velocities encountered. A further objection to the hot-wire probe, was the significant change in calibration caused by deposits on the wire from small traces of oil vapor in the air. The hot-wire probe and electronic circuits employed were of the type used by Pearson^{10,11}.

Because of the difficulties involved in measurement of the unsteady absolute flow, it was decided to measure the steady relative flow by means of a pitot-type probe mounted on the impeller. The two chief difficulties involved with this type of probe were: (1) adjustment of the probe while in motion, and (2) transference of the pressure from the rotating probe to stationary manometers. A discussion of these difficulties and the manner in which they were overcome is included in the following paragraphs.

b. The Three-Dimensional Spherical Pitot-Probe

Among the several types of pitot-probes commonly used for measurement of flow direction, as well as flow velocity and static pressure, are the claw-type probe and the spherical probe. The most direct method of obtaining flow direction with the spherical probe is to adjust the probe along two perpendicular planes until its axis points in the direction of flow. This direction is then measured by protractor scales

on the two planes. Coincidence of the probe axis with the flow direction is obtained by balancing the pressure readings on symmetrically positioned orifice openings. An alternative method of measuring flow direction consists of yawing the probe until the resultant velocity vector is in one known plane, and then using two-dimensional calibration curves for the determination of the flow direction in the other plane. Both of these methods require adjustment of the probe during operation, which involves almost insurmountable mechanical difficulties, if accurate positioning is to be obtained. To avoid this difficulty, a three-dimensional calibration scheme was devised so that any velocity direction within an incident cone-angle of 25 degrees can be determined by measuring the pressure readings at five individual holes on the sphere surface. The details of this calibration are included in Appendix B.

The probe consists essentially of a tapered shaft with a 0.190-inch-diameter spherical sensing-head. The shaft is welded at a right-angle to a crosspiece mounted between the hub and shroud surfaces of the blade cascade. Five pressure holes are on the spherical surface; the center hole is at the end of the shaft axis, and each of the other four holes are symmetrically spaced on a sphere radius forming an angle of 40 degrees with the probe axis. Detailed drawings of the probe are shown in Appendix B. Two probes were made, one having orifice holes of 0.011 inch diameter, and the other having holes of 0.016 inch diameter. The individual calibration curves for the two different probes are compared in Appendix B. The larger sized orifice holes were of a distinct advantage because of the greatly reduced response time of the instrument.

The cross-piece for both probes is at a sufficient distance downstream from the probe head, so that no appreciable flow disturbance occurs at the pickup.

c. Rotary-Seal Pressure Take-offs

A pressure transfer device is required to transfer the pressure readings from the rotating pitot-probe to stationary manometers. Hamrick, Mizisin, and Michel¹² used sealed ball-bearing units for the pressure-transfer section. Their report mentions difficulties incurred through leakage due to failures of the seals. As a preliminary investigation, a model was made employing various commercial brands of sealed ball-bearings. It was found that the model would operate perfectly for awhile, and then would develop intermittent leaks. In view of the unreliable performance of this type of seal, a transfer device employing contact-type rawhide seals was developed. This seal was used successfully at the 1500 rpm impeller speed, but at higher speeds, overheating and wear became excessive and resulted in seal failures. Considerable effort was expended to adequately lubricate and cool the seals, and at the same time, keep the air chambers perfectly free from the lubricant. Best success was achieved using air cooling and small amounts of molybdenum-disulfide as a lubricant.

In an effort to improve the pressure-transfer device, a viscous-drag mercury seal was designed. A pilot-model with transparent faces was made to determine the optimum seal gap, mercury reservoir volume, and range of operating speeds. Guided by the tests conducted with this model, the prototype was designed and is shown in Fig. 22. The best performance was obtained by using a smooth disk rotat-

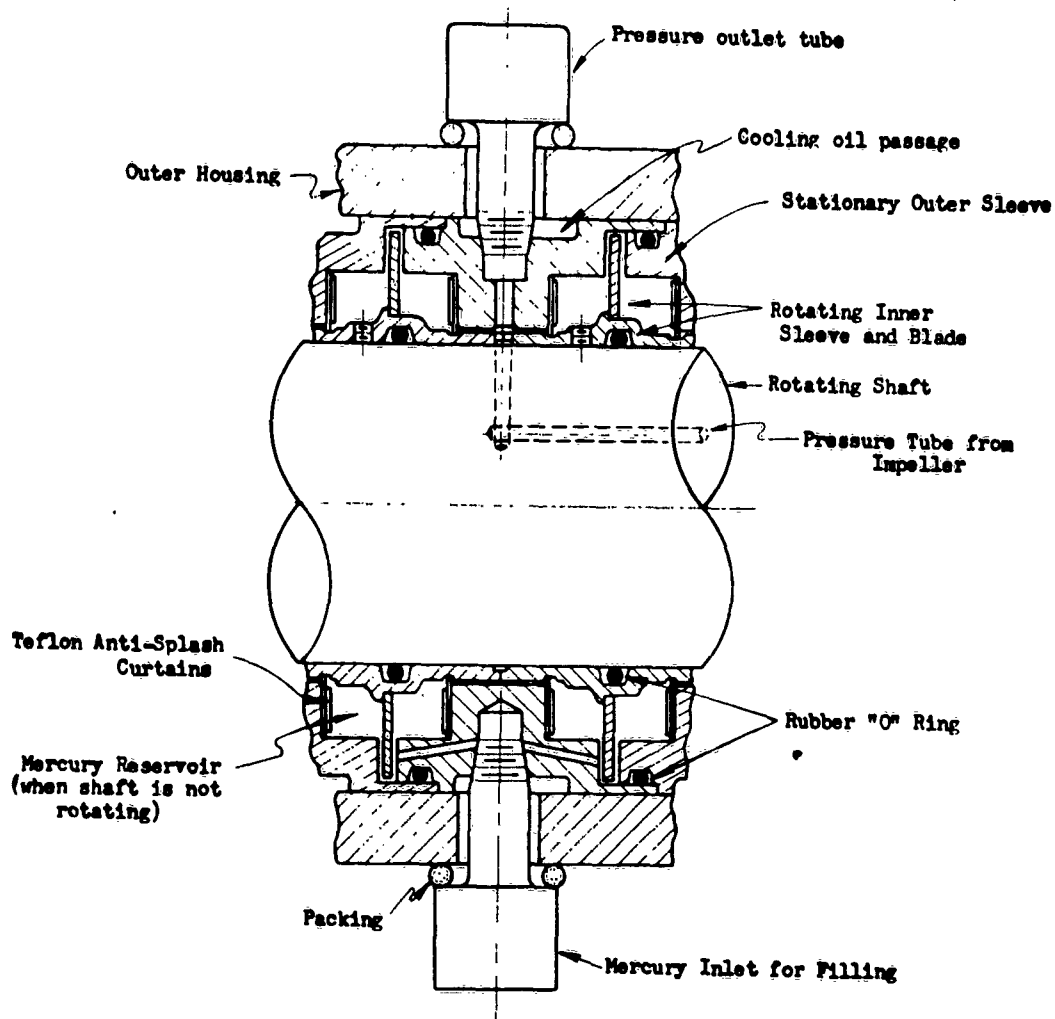


Fig. 22 SECTION OF MERCURY SEAL FOR PRESSURE TRANSFER

ing in the mercury reservoir. The centrifugal action produced by disk friction causes the mercury to rotate and fill the space between the rotating disk and the stationary housing. A disk of this type located at each side of the pressure take-off opening in the shaft produces a sealed air chamber from which the pressure may be measured with a stationary manometer.

To obtain reliable measurements of the relative flow it is necessary that the sealing be perfect. Errors were encountered at first because of contamination of the mercury caused by contact with base metals, O-rings, or minute quantities of lubricants. This contamination produces an amalgamation which will adhere to the rotating disk and interfere with the cohesive forces between the disk and the mercury, resulting in a periodic breakdown of the sealing surface and erratic pressure readings. At speeds greater than 1000 rpm the seals will quickly heat up, accelerating the formation of mercuric amalgams. Air cooling was used at the 1500 rpm speed, but was inadequate for higher impeller speeds. Liquid cooling presents a problem because of the possibility of very small amounts of the liquid coming into contact with the mercury. In place of oil, ethylene-glycol was used as the coolant because it has less serious contamination effects on the mercury. Contact of the mercury with O-rings tends to promote the formation of amalgams and it was necessary to insert a teflon back-up ring into the O-ring groove to provide a barrier between the O-ring and the mercury.

3. Overall Performance

The pressures at the inlet filter box, and inside the discharge housing, were measured to determine the overall energy input to the fluid. The pressure distribution relative to the blades was measured at the

impeller outlet by means of static pressure taps in the hub surface leading to the rotary seals. Static pressure taps were also located in the walls of the stationary diffuser. The brake torque and power were measured with the dynamometer.

C. Test Procedure

The velocity distribution relative to the rotating impeller is measured at the blade outlet with the spherical pitot-probe mounted at the six circumferential positions shown in Fig. 23. An eight-point traverse (Fig. 24) is made at each of these six circumferential positions. The resulting 48 positions cover the discharge area of 15.7 square inches between two adjacent blades. Two separate runs were required at each test point in order to check for leaks. This was accomplished by interchanging the tubes leading from the pitot-probe holes to the rotary seals, and checking the reproducibility of the manometer readings. A total set of readings were taken for a single speed and a fixed flow rate. The flow rate was measured at the standard inlet nozzle and adjusted by means of the louvers at the outlet housing. The pressures in the inlet filter chamber, the inlet draft-tube, the diffuser walls, and the drum housing at the outlet were measured. After the internal measurements of the flow distribution were completed, the rotary seal assembly was removed to eliminate the torque of this unit, and the overall performance of the impeller was measured with the dynamometer drive.

D. Presentation of Data

1. Internal Flow Measurements

The results of the detailed measurements of the flow distribution at the impeller outlet are presented in Table V. The first sections

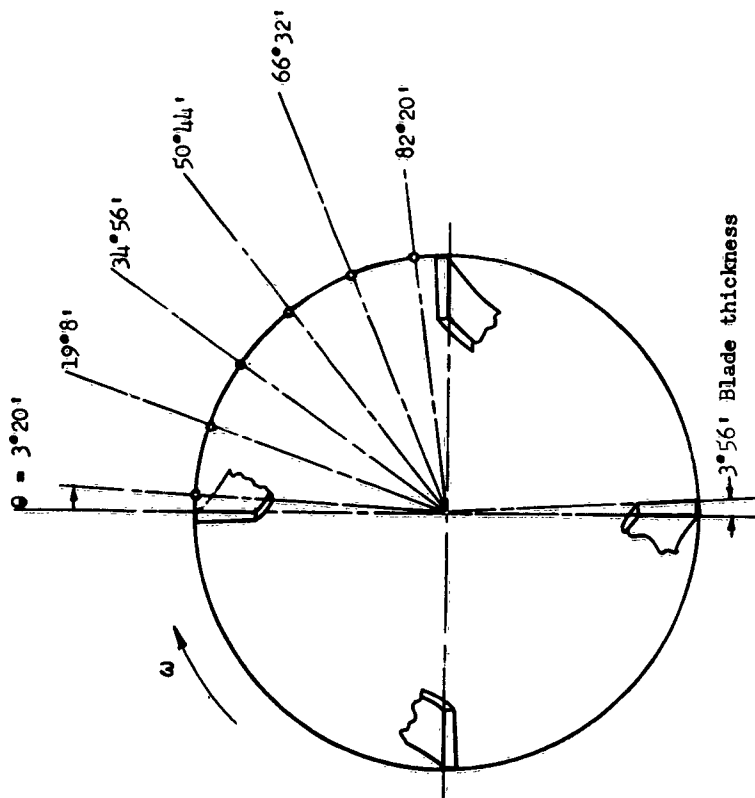
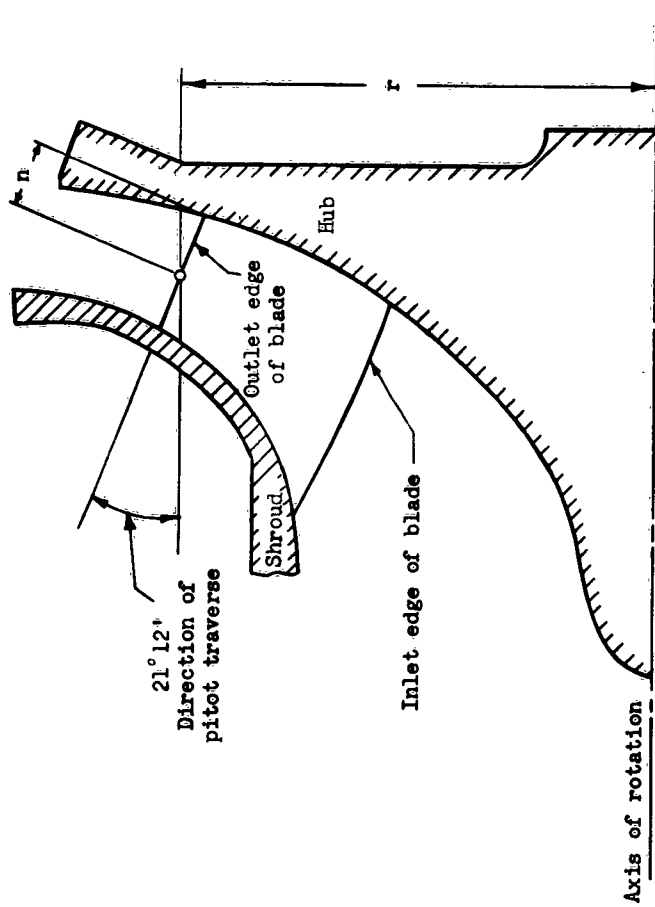


Fig. 23 PLAN VIEW PERPENDICULAR TO IMPELLER AXIS SHOWING CIRCUMFERENTIAL POSITIONS OF SPHERICAL PITOT.



Displacement "n" from Hub Surface (in.)	$n/\Delta n_T$	Radial Distance "r" from Axis (in.)
$n_1 = 0.300$	0.181	$r_1 = 6.539$
$n_2 = 0.400$.242	$r_2 = 6.575$
$n_3 = 0.600$.362	$r_3 = 6.647$
$n_4 = 0.800$.483	$r_4 = 6.720$
$n_5 = 1.000$.604	$r_5 = 6.792$
$n_6 = 1.200$.725	$r_6 = 6.865$
$n_7 = 1.400$.845	$r_7 = 6.937$
$n_8 = 1.500$.900	$r_8 = 6.973$

Fig. 24 TRAVERSE POSITIONS OF SPHERICAL PITOT IN THE MERIDIAN PLANE

of the table, (a) through (g), comprise the data taken with the spherical probe with the larger orifice holes (0.016 inch diameter), and using the mercury seals in the pressure transfer device. The latter sections of the table, (h) through (k), present the data taken with the spherical probe with the smaller orifice holes (0.011 inch diameter) and slower response time, and using the contact-type rawhide seals in the pressure-transfer device. The discharge rate is considerably lower for the runs made with the rawhide seals because a small high-resistance filter was used at the inlet to the draft tube; also, for these runs, a straight conical inlet to the draft-tube without straightening vanes was used in place of the bell-mouth nozzle.

Graphs of the data showing the distribution of the pertinent flow variables are given in Figs. 25 through 30. The distribution of the meridional component of the relative velocity across the channel from hub to shroud is shown in Fig. 25. For purposes of comparison, the theoretical velocity distribution for the meridional flow pattern, undisturbed by the blades, is shown for each of the flow rates. The distribution of the meridional component of the relative velocity from blade to blade is shown in Fig. 26, and the direction of the relative velocity in terms of δ and β is shown in Figs. 27 and 28. Figures 29 and 30 show the distribution of the whirl-moment and specific energy. In Figs. 26 through 30, the plots for the data taken with the rawhide seals are shown only for the mean meridional streamlines.

2. Efficiency, Discharge, and Head Characteristic

The primary objective of the experimental investigation was

Table V (Cont.)
FOUR-BLADED IMPELLER DATA

(c) 2200 RPM AND 11.3 CFS DISCHARGE

θ	r	w	w _s	w _r	w _t	w _m	θ	β	C _p	m	h _s	H	I
in.	fps	fps	fps	fps	fps	deg.	deg.	ft./sec.	ft.	ft.	ft.	ft.	
3°20'	6.539	106.6	37.5	62.1	87.3	64.5	74.3	36.5	20.8	35.8	123.1	-25.7	
	6.575	110.2	38.7	62.6	88.7	65.3	73.4	36.1	20.5	33.0	121.1	-25.6	
	6.647	113.1	21.1	63.6	91.1	67.0	71.6	36.3	20.2	28.2	118.6	-25.9	
	6.720	116.9	23.3	64.4	92.3	68.5	70.1	36.6	20.6	27.3	121.0	-26.4	
	6.792	118.9	26.0	64.8	92.7	71.2	68.6	37.5	21.3	22.6	123.4	-29.0	
	6.865	117.0	27.8	64.9	90.4	74.3	68.0	39.4	23.7	18.9	131.2	-34.4	
	6.937	118.0	31.3	74.9	85.1	81.1	67.3	43.6	48.1	0.8	148.6	-50.3	
	6.973	121.2	30.4	79.1	76.5	84.7	69.0	47.9	57.4	2.9	165.6	-73.4	
19°08'	6.539	108.1	35.2	53.9	92.4	56.0	74.3	31.2	13.1	38.8	104.5	-24.3	
	6.575	108.9	35.9	54.4	91.0	57.7	73.7	31.4	13.2	37.3	104.3	-25.9	
	6.647	110.4	18.0	54.4	93.8	58.3	72.0	31.9	13.8	36.7	107.1	-26.7	
	6.720	112.1	19.9	56.3	94.8	59.7	70.5	32.2	14.2	37.8	111.3	-26.1	
	6.792	113.9	21.9	57.2	96.0	61.3	69.0	32.5	14.9	39.0	115.6	-23.9	
	6.865	116.4	24.4	60.1	96.6	64.9	67.9	33.9	16.2	34.8	119.4	-24.5	
	6.937	118.7	25.1	64.5	96.4	69.2	68.7	35.7	17.8	26.5	121.9	-20.1	
	6.973	121.2	24.1	72.5	93.9	73.9	71.1	39.2	23.2	7.5	142.8	-42.8	
31°56'	6.539	113.5	35.3	53.5	98.6	55.6	74.1	29.4	11.8	22.3	86.2	-22.6	
	6.575	116.2	16.8	53.1	99.2	57.1	72.5	29.4	11.8	20.1	84.4	-21.5	
	6.647	118.0	18.0	54.5	100.7	57.4	71.7	29.6	12.8	25.0	87.3	-18.6	
	6.720	119.4	19.9	55.4	102.2	58.9	70.2	29.9	13.0	22.2	89.1	-20.1	
	6.792	120.2	23.9	56.5	102.8	60.6	68.7	30.5	15.6	19.2	92.6	-23.5	
	6.865	123.5	24.5	61.4	102.5	62.6	67.5	31.4	16.8	18.3	92.6	-27.6	
	6.937	126.9	23.1	64.2	101.8	68.9	69.2	33.9	17.7	0.7	97.1	-29.5	
	6.973	127.3	23.1	71.7	99.7	75.3	72.1	37.1	19.9	14.4	110.7	-31.7	
50°14'	6.539	116.8	16.6	57.4	100.1	60.3	73.9	31.5	13.8	12.8	85.1	-13.6	
	6.575	116.9	17.0	56.8	100.7	59.3	73.4	31.0	13.0	12.0	88.0	-12.2	
	6.647	118.3	18.3	57.5	101.2	60.3	72.3	30.6	14.0	12.9	83.6	-18.5	
	6.720	120.4	20.8	58.2	103.2	61.8	70.3	30.7	14.8	13.3	85.9	-18.7	
	6.792	122.7	22.0	62.0	102.2	63.6	68.5	31.4	15.8	13.1	87.8	-18.6	
	6.865	124.9	22.7	62.0	102.2	64.9	68.0	32.1	15.8	6.7	87.2	-21.6	
	6.937	127.9	25.7	64.2	101.8	69.2	68.0	33.7	17.0	5.0	92.7	-28.9	
	6.973	127.3	24.2	72.4	101.8	76.3	71.5	36.9	18.7	-	94.7	-39.1	
66°32'	6.539	117.9	15.6	63.3	98.1	65.2	76.2	33.6	14.9	15.7	93.4	-13.2	
	6.575	118.3	17.2	62.4	99.0	64.7	74.6	33.2	14.9	15.7	92.8	-13.0	
	6.647	119.7	20.4	62.4	100.2	65.5	71.8	33.2	15.2	17.5	91.2	-14.6	
	6.720	123.1	23.3	63.6	102.7	67.7	69.9	33.4	16.7	9.3	91.3	-13.2	
	6.792	126.5	26.2	66.4	104.5	71.4	68.4	34.3	17.7	5.1	91.6	-13.6	
	6.865	128.7	29.1	68.5	104.2	74.4	66.9	35.3	18.8	-	91.6	-13.6	
	6.937	130.4	29.5	72.0	104.5	77.8	67.7	36.6	19.4	-	91.9	-20.9	
	6.973	128.8	27.5	73.2	102.4	78.2	69.4	37.4	18.3	-	93.9	-31.3	
82°20'	6.539	96.8	17.2	72.4	61.9	74.4	76.6	50.2	34.7	44.6	54.9	-54.9	
	6.575	106.8	31.3	75.1	72.8	78.1	74.2	47.0	29.3	33.3	170.2	-39.4	
	6.647	116.1	33.8	78.0	80.3	83.9	74.7	46.3	26.2	20.8	164.8	-22.7	
	6.720	120.9	38.9	82.0	82.2	88.7	67.5	47.2	16.8	11.8	168.1	-19.4	
	6.792	125.7	36.7	85.1	83.8	92.7	66.9	47.9	16.6	-0.1	187.0	-21.9	
	6.865	131.4	37.9	89.0	86.2	96.5	66.9	48.2	15.6	-	185.5	-21.2	
	6.937	128.5	37.3	91.6	88.1	98.9	67.9	50.3	11.1	29.5	152.5	-56.6	
	6.973	120.3	22.4	91.6	78.3	91.4	75.8	49.4	12.3	-	115.0	-116.1	

Table V (Cont.)

FOUR-BLADED IMPELLER DATA

(d) 2200 RPM AND 22.3 CFS DISCHARGE

θ	r	w	w _s	w _r	w _t	w _m	θ	β	C _p	m	h _s	H	I
in.	fps	fps	fps	fps	fps	deg.	deg.	ft./sec.	ft.	ft.	ft.	ft.	
3°20'	6.539	89.6	12.9	49.4	73.6	51.1	75.4	34.8	51.9	102.9	184.2	-18.3	
	6.575	90.2	13.6	49.1	74.4	51.0	74.5	34.4	51.8	102.4	184.4	-18.8	
	6.647	92.0	15.3	49.5	75.2	51.8	72.8	34.6	52.4	105.5	189.8	-17.7	
	6.720	94.1	16.9	50.7	77.4	53.4	71.6	35.7	52.0	108.9	192.6	-14.2	
	6.792	96.6	18.9	53.1	78.4	56.4	70.4	37.5	52.0	104.5	198.5	-14.6	
	6.865	98.4	21.1	56.0	78.0	59.9	69.1	43.1	53.8	103.2	204.0	-16.4	
	6.937	104.1	27.1	65.8	76.0	71.2	67.6	43.1	57.2	85.5	214.9	-21.9	
	6.973	104.1	29.0	66.9	74.3	72.9	66.6	44.5	59.6	85.5	223.4	-24.4	
19°08'	6.539	85.5	9.4	37.2	34.4	34.4	75.8	26.7	49.1	116.4	176.7	-15.1	
	6.575	86.5	10.2	37.3	34.7	34.7	74.7	26.6	48.9	115.1	175.4	-16.4	
	6.647	87.8	11.3	37.4	34.6	34.6	73.2	26.4	49.0	116.1	177.1	-16.8	
	6.720	89.1	12.1	37.3	34.2	34.2	72.0	26.2	49.1	117.9	179.2	-16.7	
	6.792	90.8	13.0	36.6	34.2	34.2	71.4	26.6	49.2	118.9	182.2	-16.7	
	6.865	92.8	14.8	40.7	34.5	34.5	71.6	27.5	49.5	118.3	185.9	-17.9	
	6.937	91.3	14.4	47.7	34.8	34.8	72.7	31.1	50.5	108.7	185.0	-23.9	
	6.973	92.0	15.7	52.4	34.3	34.3	74.6	36.5	50.6	93.3	196.2	-55.7	
31°56'	6.539	92.0	9.9	37.9	33.2	33.2	75.4	25.2	42.3	117.8	147.8	-16.8	
	6.575	92.4	11.0	37.5	33.1	33.1	73.7	25.2	42.3	115.5	147.4	-15.9	
	6.647	93.1	11.8	38.7	33.3	33.3	70.3	24.7	42.5	117.0	147.4	-12.9	
	6.720	94.7	12.3	38.7	33.3	33.3	69.3	25.5	42.4	118.7	148.7	-11.6	
	6.792	96.7	13.3	40.5	33.3	33.3	68.3	25.8	42.3	118.3	153.0	-12.3	
	6.865	101.6	15.7	49.5	33.3	33.3	69.3	25.8	42.7	94.5	159.2	-17.5	
	6.937	102.7	15.4	53.1	33.3	33.3	72.6	32.6	42.7	24.7	172.8	-27.5	
	6.973	101.9	13.7	53.1	33.3	33.3	75.5	32.6	42.7	90.2	172.8	-27.5	
50°14'	6.539	100.4	11.5	43.0	33.0	33.0	75.0	35.0	35.6	19.4	130.7	8.1	
	6.575	99.6	11.4	43.6	33.0	33.0	74.7	35.2	36.5	19.4	130.7	5.9	
	6.647	99.2	12.3	43.9	33.0	33.0	73.8	34.9	37.7	20.9	137.2	-5.9	
	6.720	101.7	13.9	45.9	33.0	33.0	71.0	34.8	37.7	20.9	137.2	-11.7	
	6.792	104.4	15.1	47.1	33.0	33.0	69.4	34.8	37.7	20.9	136.9	-10.6	
	6.865	108.5	16.9	47.1	33.0	33.0	68.0	34.4	37.1	19.6	128.7	-10.8	
	6.937	107.9	15.4	49.1	33.0	33.0	67.1	34.2	37.1	21.4	128.1	-12.1	
	6.973	104.8	13.1	50.7	33.0	33.0	70.5	34.1	37.1	25.9	135.0	-18.1	
66°32'	6.539	98.8	10.9	46.1	32.2	32.2	75.5	30.4	36.6	18.9	131.9	9.8	
	6.575	100.6	12.2	46.0	32.2	32.2	74.6	29.7	38.9	21.2	131.0	10.4	
	6.647	103.2	14.9	45.7	32.2	32.2	72.2	29.6	40.2	24.4	134.2	-10.3	
	6.720	105.7	17.1	46.0	32.2	32.2	70.6	29.6	40.2	24.4	134.2	-10.3	
	6.792	107.5	18.8	46.5	32.2	32.2	69.0	29.6	40.2	24.4	136.0	-7.1	

Table V (Cont.)

FOUR-BLADED IMPELLER DATA

(e) 3000 RPM AND 30.8 CFS DISCHARGE

θ	r	v	v _h	v _t	v _r	v _h	v _t	v _r	v	v _h	v _t	v _r	v	τ	in.	v	v _h	v _t	v _r	v	β	ct	m	h _s	H	I
°	ft.	ft/sec	ft/sec	ft/sec	ft/sec	ft/sec	ft/sec	ft/sec	ft/sec	ft/sec	ft/sec	ft/sec	ft/sec	ft/sec	ft.	ft.	ft.	ft.	ft.	ft.	ft.	ft.	ft.	ft.	ft.	ft.
3°20'	6.539	119.7	17.5	100.4	62.9	119.7	74.5	33.0	70.8	38.6	204.4	148.4	29.1	6.540	59.1	4.9	29.7	50.2	31.2	29.2	31.6	35.4	19.3	36.3	71	23
	6.575	118.6	18.8	98.4	62.0	118.6	73.1	33.1	72.7	39.8	215.2	148.5	29.1	6.576	60.1	4.9	29.7	50.2	31.2	29.2	31.6	35.4	19.3	36.3	71	23
	6.611	122.0	21.0	101.7	64.2	122.0	71.9	33.6	72.3	40.0	215.0	148.5	29.1	6.612	60.1	4.9	29.7	50.2	31.2	29.2	31.6	35.4	19.3	36.3	71	23
	6.720	123.5	23.2	100.7	65.7	123.5	70.6	34.3	73.9	41.4	220.9	148.5	29.1	6.721	60.1	4.9	29.7	50.2	31.2	29.2	31.6	35.4	19.3	36.3	71	23
	6.792	124.7	26.0	100.7	67.1	124.7	67.7	34.2	74.1	42.8	230.7	148.5	29.1	6.793	60.1	4.9	29.7	50.2	31.2	29.2	31.6	35.4	19.3	36.3	71	23
	6.865	128.7	29.3	103.1	71.2	128.7	67.6	35.0	74.1	44.2	239.7	148.5	29.1	6.866	60.1	4.9	29.7	50.2	31.2	29.2	31.6	35.4	19.3	36.3	71	23
	6.937	133.6	32.4	104.3	74.2	133.6	64.6	35.8	74.1	45.6	248.7	148.5	29.1	6.938	60.1	4.9	29.7	50.2	31.2	29.2	31.6	35.4	19.3	36.3	71	23
	6.973	133.4	30.9	99.1	71.5	133.4	63.9	42.5	74.1	46.0	242.5	148.5	29.1	6.974	60.1	4.9	29.7	50.2	31.2	29.2	31.6	35.4	19.3	36.3	71	23
	6.539	116.3	13.3	104.9	64.9	116.3	75.1	26.3	67.0	36.5	212.8	148.4	29.1	6.540	57.1	6.9	20.2	52.9	21.4	71.3	22.0	32.7	17.8	36.4	60	27
	6.575	117.8	14.0	105.7	65.1	117.8	74.4	26.2	66.4	36.4	212.4	148.4	29.1	6.576	57.1	6.9	20.2	52.9	21.4	71.3	22.0	32.7	17.8	36.4	60	27
6.611	120.6	15.5	105.2	65.2	120.6	72.8	25.9	65.5	36.3	211.0	148.4	29.1	6.612	57.1	6.9	20.2	52.9	21.4	71.3	22.0	32.7	17.8	36.4	60	27	
6.720	123.3	16.6	105.1	65.3	123.3	72.3	26.3	65.4	36.2	210.6	148.4	29.1	6.721	57.1	6.9	20.2	52.9	21.4	71.3	22.0	32.7	17.8	36.4	60	27	
6.792	126.5	17.9	105.2	65.4	126.5	72.0	27.3	65.3	36.1	210.9	148.4	29.1	6.793	57.1	6.9	20.2	52.9	21.4	71.3	22.0	32.7	17.8	36.4	60	27	
6.865	129.5	18.6	105.4	65.5	129.5	72.7	28.9	66.3	36.0	210.6	148.4	29.1	6.866	57.1	6.9	20.2	52.9	21.4	71.3	22.0	32.7	17.8	36.4	60	27	
6.937	130.2	20.1	105.4	67.4	130.2	73.0	32.8	72.2	35.9	211.0	148.4	29.1	6.938	57.1	6.9	20.2	52.9	21.4	71.3	22.0	32.7	17.8	36.4	60	27	
6.973	132.1	20.1	98.7	69.0	132.1	73.8	36.1	73.8	35.9	202.8	148.4	29.1	6.974	57.1	6.9	20.2	52.9	21.4	71.3	22.0	32.7	17.8	36.4	60	27	
3°56'	6.539	130.2	13.8	115.7	58.0	130.2	76.6	27.3	55.5	30.2	161.9	264.9	29.7	6.540	59.8	5.1	17.7	56.9	18.4	73.9	18.8	25.7	24.0	32.2	48	20
	6.575	128.0	15.1	115.9	58.0	128.0	73.9	25.1	56.2	30.8	180.5	275.5	29.7	6.576	62.7	6.6	18.0	59.7	19.1	69.9	18.7	26.8	24.9	30.6	47	25
	6.611	127.0	17.5	117.1	58.2	127.0	71.1	24.8	56.9	31.5	185.2	290.9	29.7	6.612	62.7	6.7	18.1	59.1	19.2	69.0	19.0	28.9	27.5	30.2	55	24
	6.720	130.6	18.6	117.7	58.4	130.6	70.8	25.6	58.2	32.6	201.1	303.3	29.7	6.721	62.7	6.7	18.2	61.2	20.0	67.7	19.9	29.2	29.2	31.8	50	26
	6.792	134.7	21.3	120.6	58.1	134.7	69.2	26.5	57.2	32.4	194.2	309.0	29.7	6.793	62.7	6.7	18.2	61.2	20.0	67.7	19.9	29.2	29.2	31.8	50	26
	6.865	139.9	21.7	123.7	58.2	139.9	70.6	27.9	56.0	32.0	186.6	302.4	29.7	6.866	62.7	6.7	18.2	61.2	20.0	67.7	19.9	29.2	29.2	31.8	50	26
	6.937	141.7	19.9	122.1	58.2	141.7	74.0	30.5	59.5	34.4	165.8	309.9	29.7	6.938	62.7	6.7	18.2	61.2	20.0	67.7	19.9	29.2	29.2	31.8	50	26
	6.973	139.7	19.0	119.3	58.2	139.7	71.8	31.3	63.3	36.8	165.8	309.9	29.7	6.974	62.7	6.7	18.2	61.2	20.0	67.7	19.9	29.2	29.2	31.8	50	26
	6.539	137.9	16.4	119.8	57.0	137.9	76.2	29.9	63.3	36.8	143.5	258.4	29.7	6.540	61.0	4.9	16.5	56.5	17.2	65.9	16.7	70.2	15.4	31.3	57	31
	6.575	135.8	15.6	123.0	55.4	135.8	74.3	25.1	60.1	35.4	135.5	234.7	29.7	6.576	61.0	4.9	16.5	56.5	17.2	65.9	16.7	70.2	15.4	31.3	57	31
6.611	138.6	16.6	126.7	53.6	138.6	72.8	23.9	57.3	35.2	135.6	234.7	29.7	6.612	61.0	4.9	16.5	56.5	17.2	65.9	16.7	70.2	15.4	31.3	57	31	
6.720	141.4	19.5	128.4	56.1	141.4	70.8	24.9	58.0	35.2	147.0	236.8	29.7	6.721	61.0	4.9	16.5	56.5	17.2	65.9	16.7	70.2	15.4	31.3	57	31	
6.792	144.2	22.1	129.8	56.9	144.2	69.4	25.9	58.3	35.2	159.1	256.8	29.7	6.793	61.0	4.9	16.5	56.5	17.2	65.9	16.7	70.2	15.4	31.3	57	31	
6.865	147.4	23.2	130.4	56.8	147.4	70.3	27.8	59.3	35.2	144.2	256.8	29.7	6.866	61.0	4.9	16.5	56.5	17.2	65.9	16.7	70.2	15.4	31.3	57	31	
6.937	150.8	22.1	131.2	56.8	150.8	72.7	29.6	59.5	35.2	134.2	259.5	29.7	6.938	61.0	4.9	16.5	56.5	17.2	65.9	16.7	70.2	15.4	31.3	57	31	
6.973	151.3	18.2	131.6	56.8	151.3	75.9	29.6	63.3	35.2	134.2	259.5	29.7	6.974	61.0	4.9	16.5	56.5	17.2	65.9	16.7	70.2	15.4	31.3	57	31	
6°32'	6.539	139.1	15.6	120.7	57.4	139.1	77.0	29.8	50.5	27.5	126.7	240.6	29.7	6.540	58.4	10.3	17.7	48.0	33.3	72.0	18.2	31.7	20.6	28.1	67	33
	6.575	136.1	19.3	117.1	56.3	136.1	73.8	30.5	54.8	30.0	115.9	246.7	29.7	6.576	58.4	10.3	17.7	48.0	33.3	72.0	18.2	31.7	20.6	28.1	67	33
	6.611	141.0	20.8	120.8	56.2	141.0	71.5	27.7	50.2	27.3	128.4	232.8	29.7	6.612	58.4	10.3	17.7	48.0	33.3	72.0	18.2	31.7	20.6	28.1	67	33
	6.720	145.7	23.4	129.0	55.7	145.7	70.4	28.6	47.9	26.8	125.4	236.5	29.7	6.721	58.4	10.3	17.7	48.0	33.3	72.0	18.2	31.7	20.6	28.1	67	33
	6.792	147.5	25.8	126.7	55.7	147.5	70.0	30.0	51.1	28.1	133.1	262.2	29.7	6.793	58.4	10.3	17.7	48.0	33.3	72.0	18.2	31.7	20.6	28.1	67	33
	6.865	148.9	28.2	125.3	55.9	148.9	69.5	32.7	51.4	28.1	137.2	283.5	29.7	6.866	58.4	10.3	17.7	48.0	33.3	72.0	18.2	31.7	20.6	28.1	67	33
	6.937	149.1	24.5	124.5	55.9	149.1	73.0	34.1	58.1	33.6	134.3	297.2	29.7	6.938	58.4	10.3	17.7	48.0	33.3	72.0	18.2	31.7	20.6	28.1	67	33
	6.973	147.2	17.1	124.8	55.9	147.2	77.3	32.0	61.1	33.6	117.1	263.4	29.7	6.974	58.4	10.3	17.7	48.0	33.3	72.0	18.2	31.7	20.6	28.1	67	33
	6.539	85.7	3.1	50.6	65.7	85.7	87.4	32.0	61.1	33.6	117.1	263.4	29.7	6.540	58.4	10.3	17.7	48.0	33.3	72.0	18.2	31.7	20.6	28.1	67	33
	6.575	84.1	2.9	50.6	65.7	84.1	79.8	31.5	61.1	33.6	104.1	241.0	29.7	6.576	58.4	10.3	17.7	48.0	33.3	72.0	18.2	31.7	20.6	28.1	67	33
6.611	82.0	2.8	50.6	65.7	82.0	70.1	29.0	61.1	33.6	91.1	217.3	29.7	6.612	58.4	10.3	17.7	48.0	33.3	72.0	18.2	31.7	20.6	28.1	67	33	
6.720	78.9	2.7	49.0	64.9	78.9	67.6	26.9																			

Table V (Cont.)

FOUR-BLADED IMPELLER DATA

(1) 2000 RPM AND 16.8 CFS DISCHARGE

φ	T	v	v _z	v _r	v _t	v _n	β	β	c _t	m	h _n	H	I
°	in.	fps	fps	fps	fps	fps	deg.	deg.	ft/sec.	ft ² /sec.	ft.	ft.	ft.
3°20'	6.510	80.8	7.7	12.1	68.3	13.0	31.2	17.7	15.8	21.9	121.1	102	69
	6.608	81.9	10.5	12.1	69.1	13.0	31.0	17.5	15.8	21.2	120.1	102	69
	6.722	83.5	11.7	12.1	70.7	13.0	30.7	17.3	15.8	20.4	119.6	102	69
	6.813	86.2	13.5	12.1	72.7	13.0	30.5	17.1	15.8	19.6	118.5	102	69
	6.971	88.3	16.5	12.1	74.8	13.0	30.1	16.8	15.8	18.8	117.3	102	69
19°08'	6.510	71.4	5.8	20.9	68.0	21.7	34.1	17.0	16.1	25.1	119.9	98	65
	6.608	75.6	8.5	20.3	70.4	21.6	33.8	16.8	16.1	24.8	119.2	97	65
	6.722	81.1	11.2	20.3	72.7	21.6	33.5	16.5	16.1	24.6	118.5	97	65
	6.813	87.7	14.5	20.3	75.4	21.6	33.2	16.2	16.1	24.0	117.8	97	65
	6.971	92.7	19.2	20.3	78.8	21.6	32.8	15.8	16.1	23.8	117.3	97	65
31°56'	6.510	70.6	7.6	20.1	76.6	21.8	35.0	15.5	16.1	21.4	119.9	91	61
	6.608	74.9	10.2	20.1	78.5	21.8	34.7	15.2	16.1	20.7	119.2	91	61
	6.722	81.9	13.1	20.1	81.2	21.8	34.4	14.9	16.1	20.0	118.5	91	61
	6.813	89.9	17.1	20.1	84.2	21.8	34.0	14.6	16.1	19.3	117.8	91	61
	6.971	98.9	23.2	20.1	88.2	21.8	33.6	14.2	16.1	18.6	117.3	91	61
50°11'	6.510	90.2	11.9	28.0	85.6	28.4	38.0	13.0	16.1	21.0	125.5	80	61
	6.608	94.1	15.2	28.0	88.2	28.4	37.7	12.7	16.1	20.3	124.8	80	61
	6.722	100.2	20.3	28.0	91.9	28.4	37.4	12.4	16.1	19.6	124.1	80	61
	6.813	108.2	26.5	28.0	96.2	28.4	37.0	12.1	16.1	18.9	123.4	80	61
	6.971	118.1	35.2	28.0	102.1	28.4	36.6	11.7	16.1	18.2	122.7	80	61
66°30'	6.510	90.2	11.2	30.1	81.8	31.2	41.8	10.2	16.1	16.5	131.8	53	58
	6.608	92.7	14.5	30.1	84.2	31.2	41.5	9.9	16.1	15.8	131.1	53	58
	6.722	98.9	19.2	30.1	88.2	31.2	41.2	9.6	16.1	15.1	130.4	53	58
	6.813	105.2	25.1	30.1	92.1	31.2	40.8	9.3	16.1	14.4	129.7	53	58
	6.971	114.2	33.2	30.1	98.2	31.2	40.4	8.9	16.1	13.7	129.0	53	58
82°20'	6.510	89.6	11.6	37.6	73.2	51.5	45.1	7.3	16.1	10.8	141.5	31	56
	6.608	91.1	15.1	37.6	75.7	51.5	44.8	7.0	16.1	10.1	140.8	31	56
	6.722	97.1	20.3	37.6	78.8	51.5	44.5	6.7	16.1	9.4	140.1	31	56
	6.813	104.1	26.5	37.6	82.1	51.5	44.2	6.4	16.1	8.7	139.4	31	56
	6.971	112.1	35.2	37.6	87.2	51.5	43.8	6.0	16.1	8.0	138.7	31	56

Table V (Cont.)

FOUR-BLADED IMPELLER DATA

(1) 2000 RPM AND 12.9 CFS DISCHARGE

φ	T	v	v _z	v _r	v _t	v _n	β	β	c _t	m	h _n	H	I
°	in.	fps	fps	fps	fps	fps	deg.	deg.	ft/sec.	ft ² /sec.	ft.	ft.	ft.
3°20'	6.510	62.8	7.0	29.8	54.8	30.6	76.8	27.2	59.3	12.3	106.8	176	34
	6.608	67.1	9.8	29.8	57.9	30.6	76.8	27.2	59.3	12.3	106.8	176	34
	6.722	71.7	13.8	29.8	61.0	30.6	76.8	27.2	59.3	12.3	106.8	176	34
	6.813	78.0	18.1	29.8	64.2	30.6	76.8	27.2	59.3	12.3	106.8	176	34
	6.971	84.2	24.2	29.8	68.7	30.6	76.8	27.2	59.3	12.3	106.8	176	34
19°08'	6.510	63.0	1.0	18.5	60.2	18.5	86.9	17.1	55.1	30.4	115.9	168	30
	6.608	66.3	4.4	18.5	63.0	18.5	86.9	17.1	55.1	30.4	115.9	168	30
	6.722	69.7	8.6	18.5	66.8	18.5	86.9	17.1	55.1	30.4	115.9	168	30
	6.813	74.1	13.6	18.5	70.7	18.5	86.9	17.1	55.1	30.4	115.9	168	30
	6.971	80.2	20.2	18.5	75.4	18.5	86.9	17.1	55.1	30.4	115.9	168	30
31°56'	6.510	67.6	1.2	15.8	65.8	15.9	85.4	13.6	48.3	36.4	97.3	137	25
	6.608	68.4	4.0	15.8	67.0	15.9	85.4	13.6	48.3	36.4	97.3	137	25
	6.722	73.2	8.1	15.8	71.5	15.9	85.4	13.6	48.3	36.4	97.3	137	25
	6.813	78.6	12.7	15.8	75.3	15.9	85.4	13.6	48.3	36.4	97.3	137	25
	6.971	82.1	18.5	15.8	79.5	15.9	85.4	13.6	48.3	36.4	97.3	137	25
50°11'	6.510	72.5	5.0	15.8	70.6	16.7	72.7	12.3	43.6	23.8	94.5	128	27
	6.608	77.9	9.2	15.8	75.5	16.7	72.7	12.3	43.6	23.8	94.5	128	27
	6.722	83.1	14.5	15.8	80.3	16.7	72.7	12.3	43.6	23.8	94.5	128	27
	6.813	88.1	20.3	15.8	85.1	16.7	72.7	12.3	43.6	23.8	94.5	128	27
	6.971	94.4	28.5	15.8	90.3	16.7	72.7	12.3	43.6	23.8	94.5	128	27
66°30'	6.510	81.6	10.6	28.8	75.6	30.7	69.8	22.1	30.5	20.9	65.0	103	33
	6.608	82.2	13.6	28.8	78.4	30.3	69.8	22.1	30.5	20.9	65.0	103	33
	6.722	88.9	18.9	28.8	83.4	30.3	69.8	22.1	30.5	20.9	65.0	103	33
	6.813	92.2	25.9	28.8	88.5	30.3	69.8	22.1	30.5	20.9	65.0	103	33
	6.971	99.4	35.2	28.8	93.2	30.3	69.8	22.1	30.5	20.9	65.0	103	33

Table V (Cont.)

FOUR-BLADED IMPELLER DATA

(k) 2500 RPM AND 20.0 GFS DISCHARGE

θ	r in.	w fps	w _z fps	w _r fps	w _t fps	w _m fps	δ deg.	β deg.	c _t fps	$\frac{m}{ft^2/sec}$	h _s ft.	H ft.	I ft.
3°20'	6.608	91.6	16.5	42.2	79.5	45.3	68.7	29.8	63.6	34.8	87.6	182.3	-101
	6.722	100.3	16.9	46.4	87.3	49.3	70.0	29.5	58.4	32.5	63.6	154.4	-110
	6.903	102.0	23.4	50.4	85.4	55.5	65.1	33.1	64.0	36.5	67.7	179.2	-118
	6.971	101.0	26.7	52.8	81.8	59.1	63.1	35.9	68.7	39.5	73.2	200.8	-120
19°08'	6.608	89.2	10.3	26.7	84.3	28.7	67.3	19.1	58.8	32.1	93.7	160.2	-101
	6.722	96.2	13.9	29.6	90.5	32.7	64.8	19.9	55.3	30.7	83.4	147.3	-103
	6.903	100.4	12.2	31.5	94.6	33.8	68.8	19.6	54.8	31.3	80.0	144.3	-110
	6.971	95.4	11.7	34.4	88.1	36.4	71.2	22.5	62.3	35.8	82.1	163.0	-129
34°56'	6.608	99.4	8.4	27.4	95.1	28.7	72.9	16.9	36.4	26.2	78.0	126.6	-86
	6.722	107.5	12.6	70.3	95.8	32.9	67.5	17.7	43.3	24.1	43.0	90.1	-106
	6.903	111.0	13.6	31.0	105.7	33.9	66.3	17.8	43.7	24.9	58.8	106.3	-96
	6.971	109.0	11.5	30.4	102.4	35.3	69.8	18.5	43.3	27.1	55.4	109.3	-111
50°44'	6.608	111.0	10.2	32.4	105.7	34.0	72.5	17.8	37.4	20.4	46.3	85.9	-80
	6.722	114.0	12.6	34.4	107.8	36.7	69.9	19.0	37.9	21.1	39.0	74.0	-98
	6.903	119.0	15.9	37.1	112.0	40.3	66.7	19.8	37.4	21.3	20.5	67.5	-106
	6.971	119.0	11.3	33.3	114.1	35.1	71.6	16.4	36.4	20.9	29.4	69.2	-101
66°32'	6.608	110.0	13.9	35.6	103.0	38.2	68.7	20.6	40.1	21.9	38.3	85.9	-92
	6.722	117.0	17.2	41.0	108.0	46.7	67.8	22.6	37.7	21.0	20.5	76.5	-94
	6.903	122.0	21.3	40.6	113.1	45.8	62.3	22.0	36.3	20.7	19.2	72.3	-96
	6.971	121.0	16.2	37.7	113.8	41.0	67.7	19.9	36.7	21.1	20.5	67.5	-104
82°20'	6.608	110.0	23.9	58.0	90.3	62.8	67.6	34.8	52.8	28.9	33.5	137.9	-97
	6.722	118.0	31.2	65.7	93.0	72.6	64.6	38.0	52.7	29.3	9.0	134.1	-104
	6.903	125.0	37.7	64.3	100.4	74.5	59.6	36.6	49.0	28.0	-	96.1	-132
	6.971	122.0	27.8	70.3	95.8	75.6	68.4	38.3	54.7	31.5	-	90.1	-166

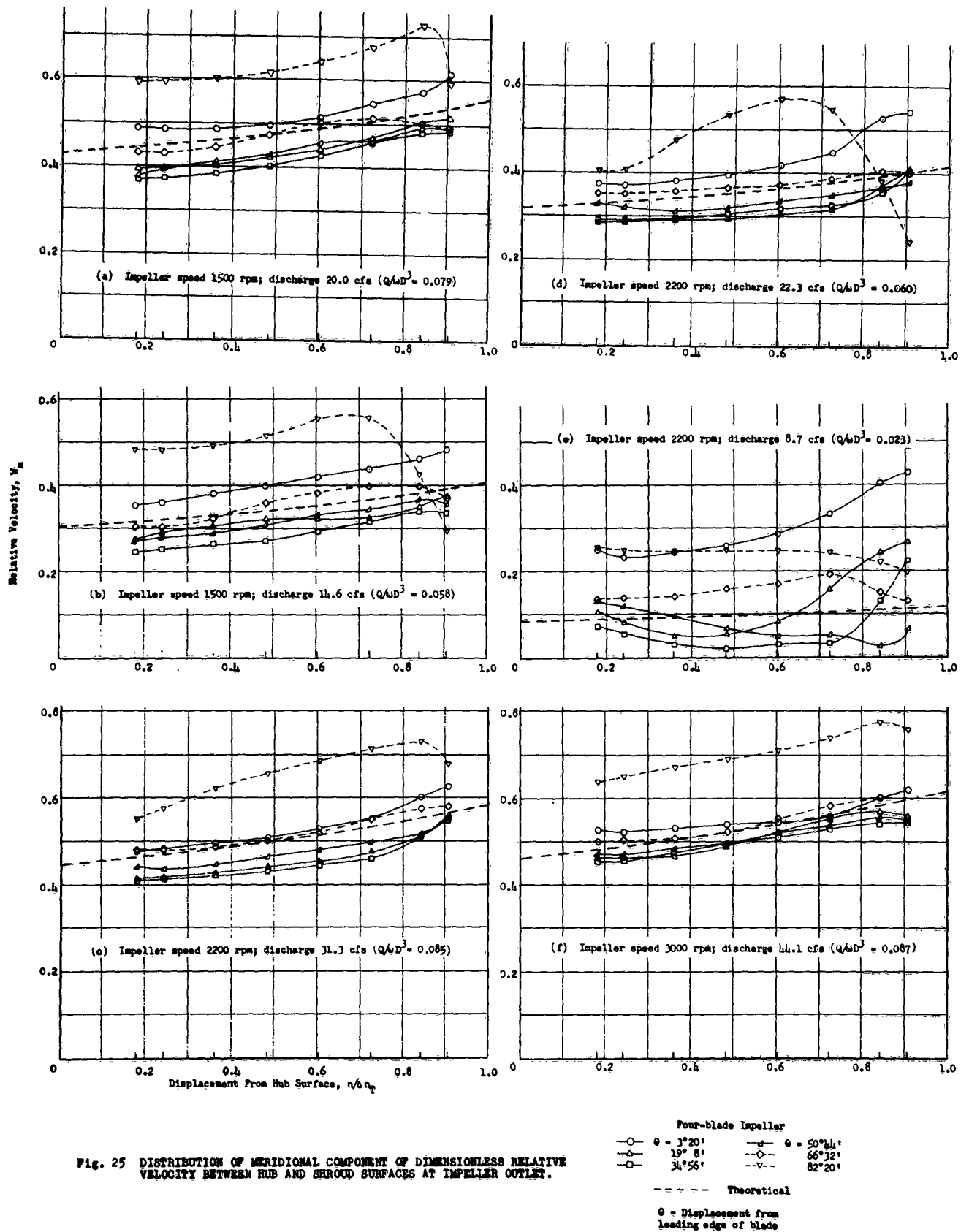


Fig. 25 DISTRIBUTION OF MERIDIONAL COMPONENT OF DIMENSIONLESS RELATIVE VELOCITY BETWEEN HUB AND SHROUD SURFACES AT IMPELLER OUTLET.

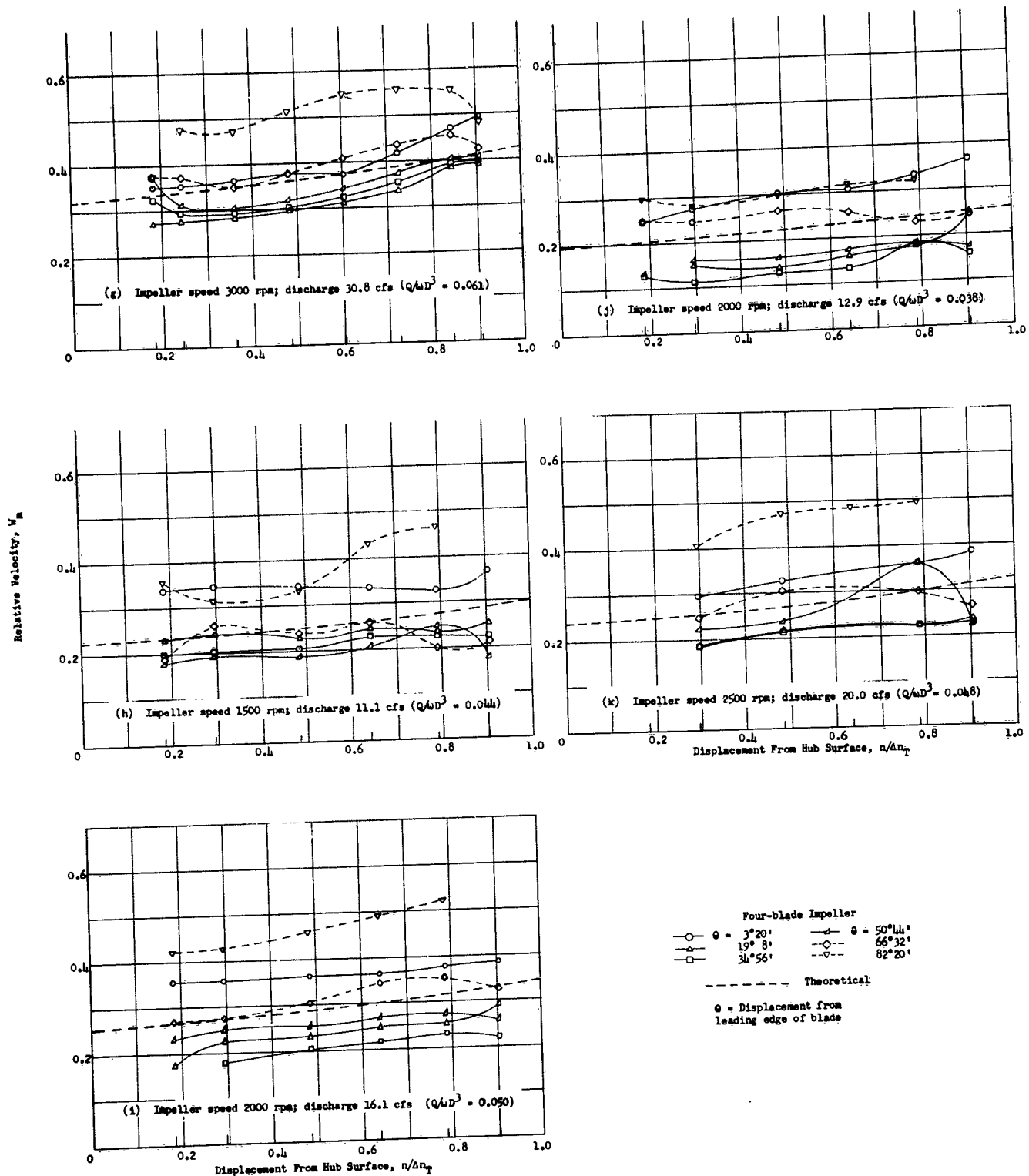
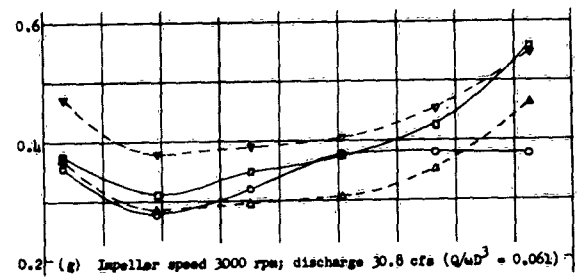
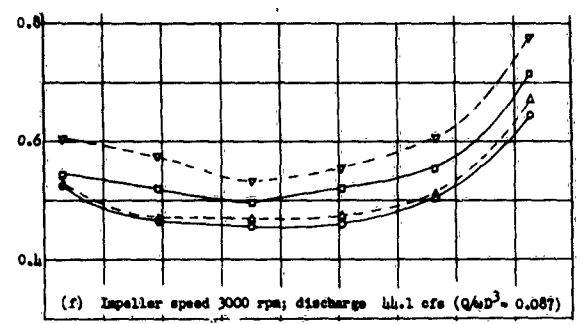
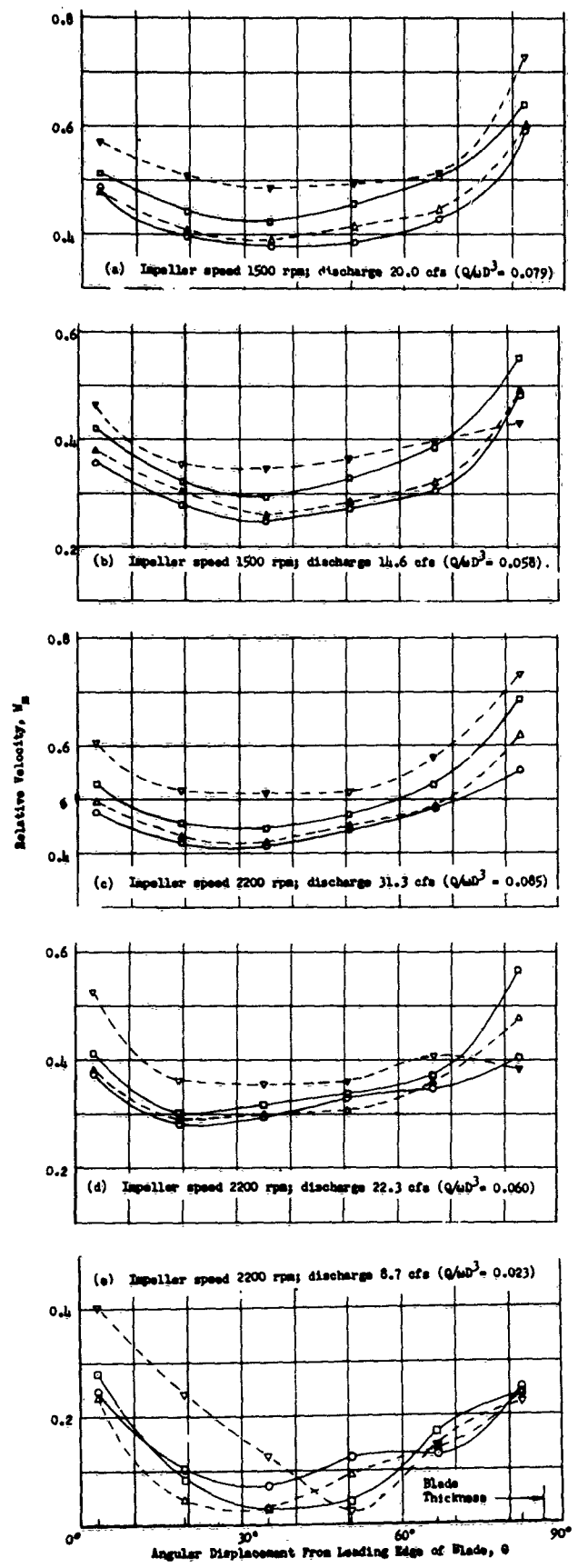


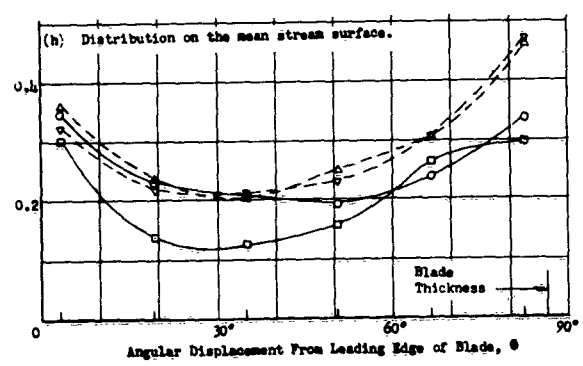
Fig. 25 - Concluded DISTRIBUTION OF MERIDIONAL COMPONENT OF DIMENSIONLESS RELATIVE VELOCITY BETWEEN HUB AND SHROUD SURFACES AT IMPELLER OUTLET.



(a)-(g) Four-blade Impeller

- $r/\Delta r_p = 0.181$
- △— 0.362
- 0.604
- ▽— 0.845

$r/\Delta r_p =$ Displacement from hub surface



(h) Four-blade Impeller

- $Q/\omega D^3 = 0.038$ (2000 rpm)
- △— 0.044 (1500 rpm)
- 0.048 (2500 rpm)
- ▽— 0.050 (2000 rpm)

$r/\Delta r_p =$ Displacement from hub surface = 0.543

Fig. 26 DISTRIBUTION OF MERIDIONAL COMPONENT OF DIMENSIONLESS RELATIVE VELOCITY ALONG PERIPHERY AT IMPELLER OUTLET.

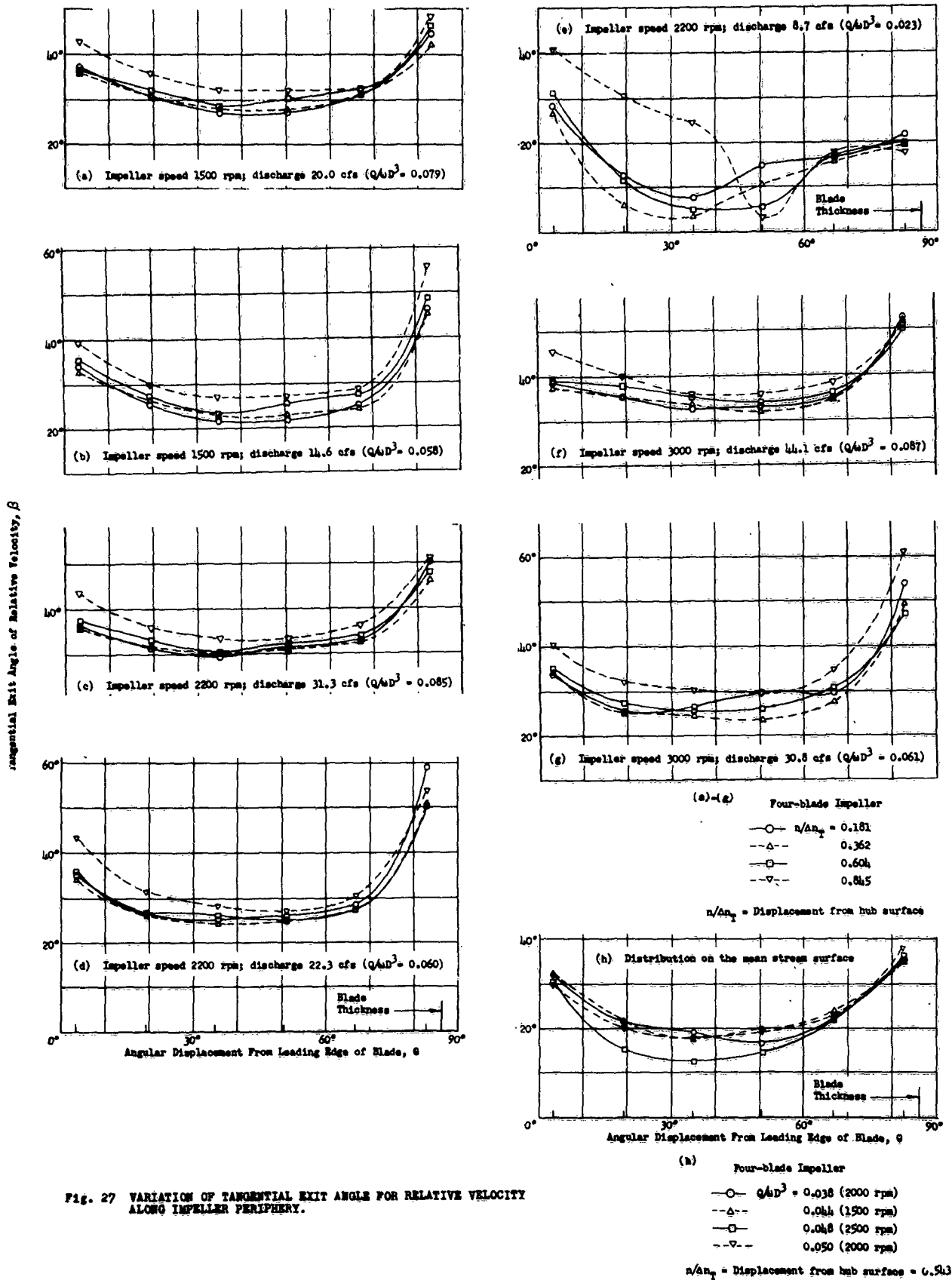


Fig. 27 VARIATION OF TANGENTIAL EXIT ANGLE FOR RELATIVE VELOCITY ALONG IMPELLER PERIPHERY.

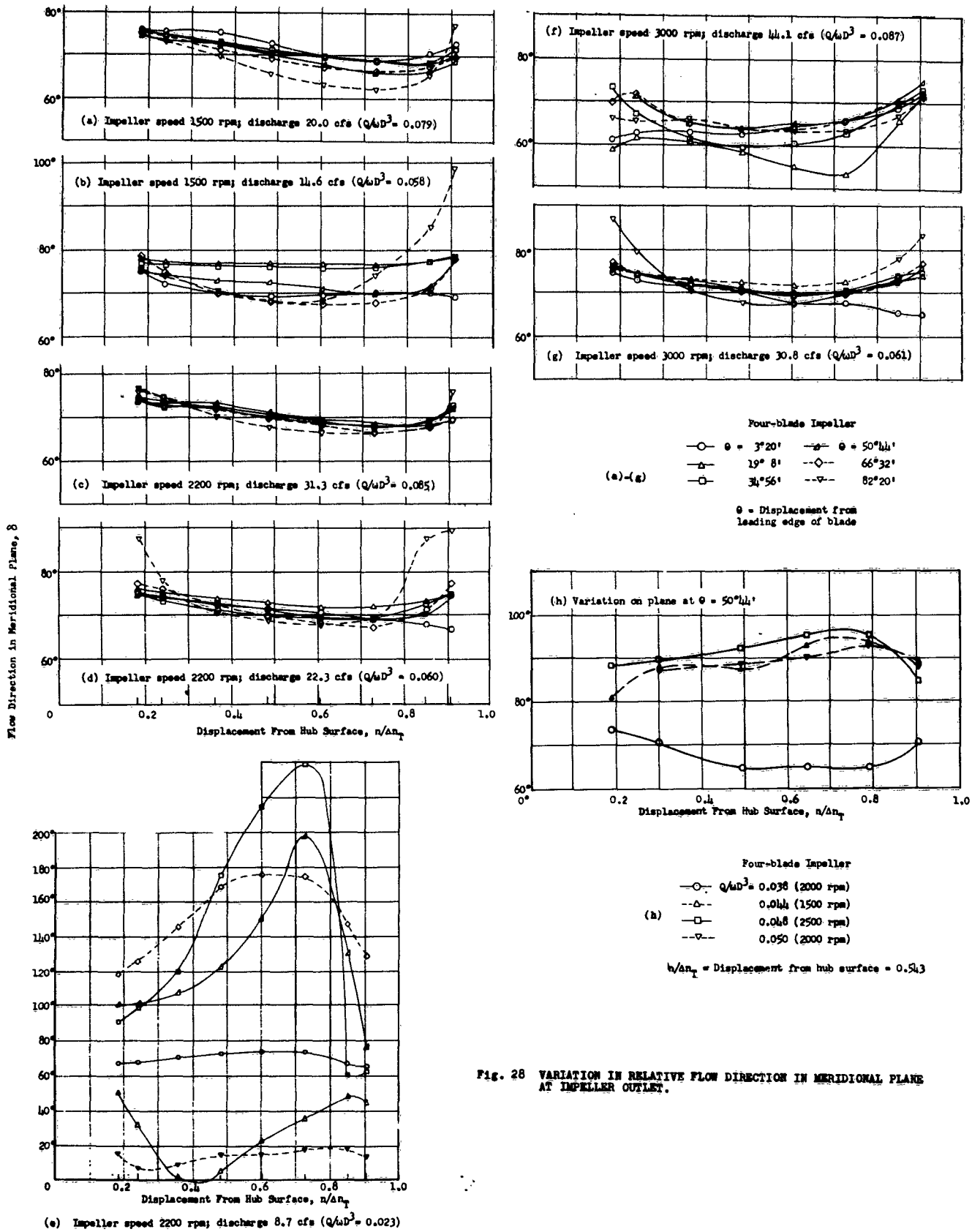


Fig. 28 VARIATION IN RELATIVE FLOW DIRECTION IN MERIDIONAL PLANE AT IMPELLER OUTLET.

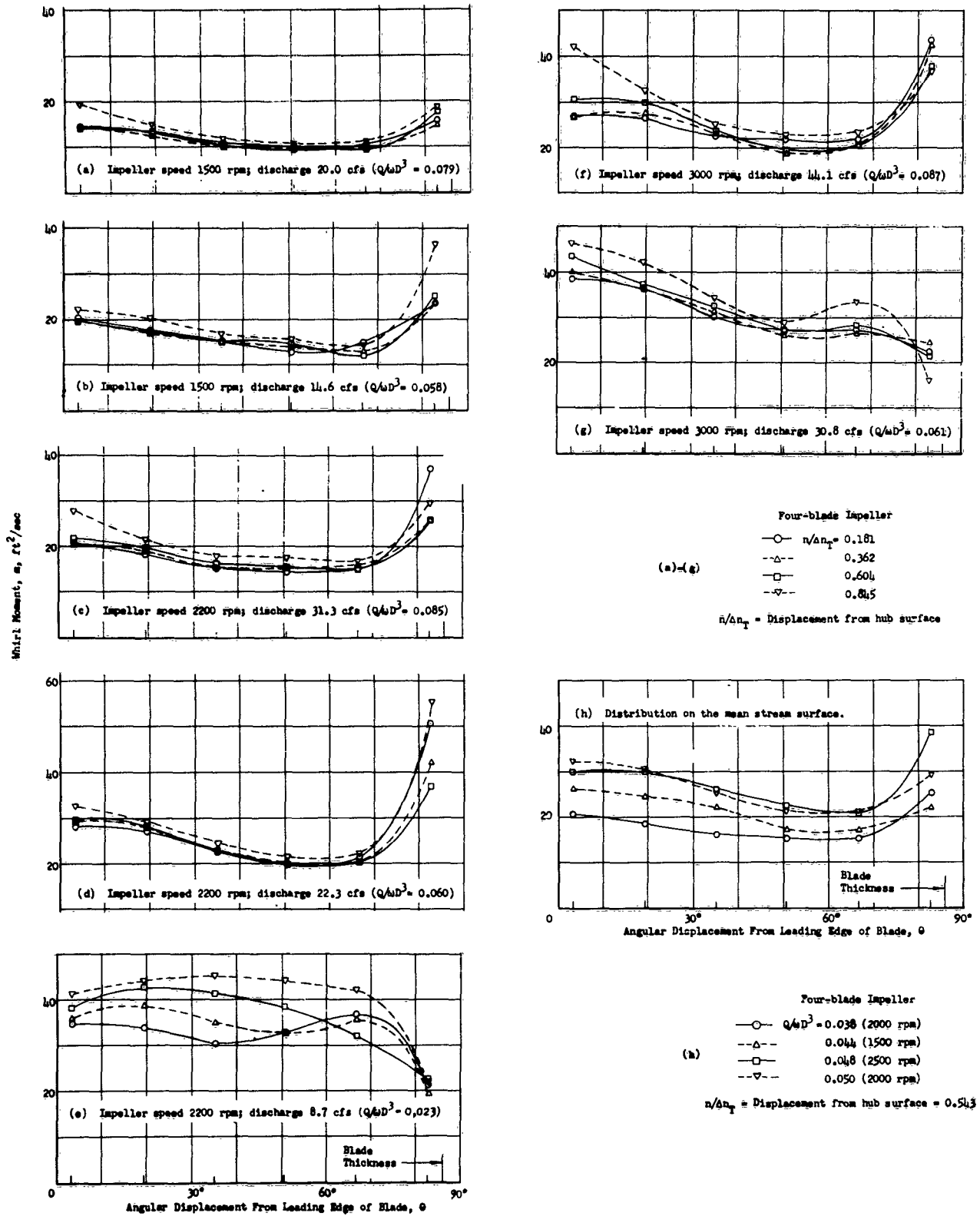


Fig. 29 DISTRIBUTION OF WHIRL-MOMENT ALONG PERIPHERY AT IMPELLER OUTLET.

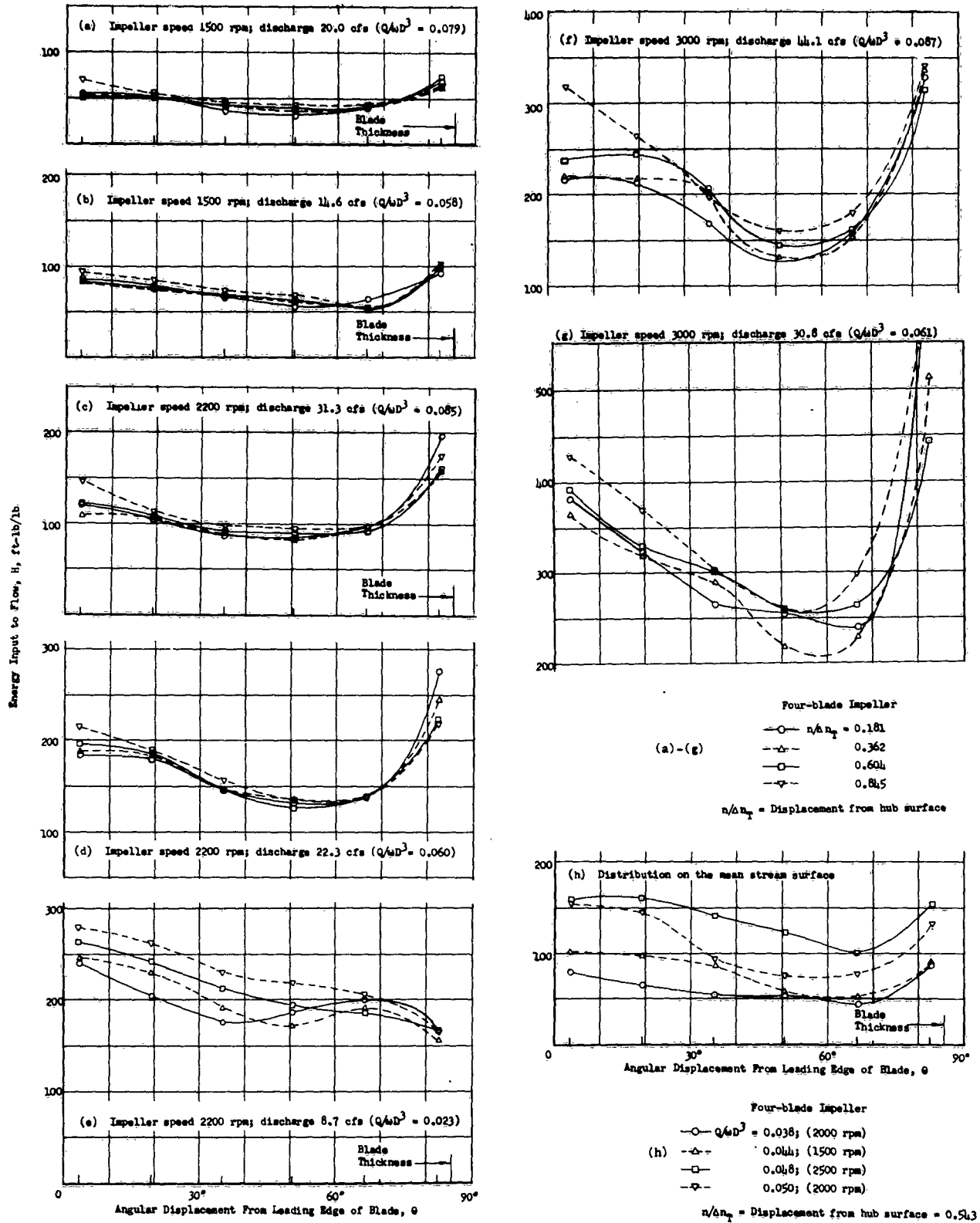


Fig. 30 DISTRIBUTION OF ENERGY INPUT TO FLOW AS MEASURED ALONG PERIPHERY AT IMPELLER OUTLET.

to obtain measurements of the internal flow distributions. The test stand was designed with this in mind, and the outlet diffuser is constructed so that disturbances of the relative flow will be minimized. For this reason a collector ring is not included, and the conventional compressor efficiency which includes the diffuser performance cannot be measured. However, as an indication of the general performance of the impeller design, the shaft power was measured with the dynamometer, and the corresponding static pressure was recorded for a range of flow rates at 3500 rpm. An "overall efficiency" was computed by considering the energy input to the gas to be the sum of the static pressure head in the diffuser, plus an average velocity head based upon the flow rate and the diffuser area. This overall efficiency is shown in Fig. 31. It must be noted that this efficiency includes the draft-tube inlet losses; there is also probably a considerable windage loss caused by the stainless steel tubing, supporting ring, and pitot-positioning-disk on the back of the impeller. The same energy input considered for the determination of the overall efficiency was also used for the head characteristic. The head input is plotted as a dimensionless ratio based upon the impeller tip speed. The impeller efficiency is determined for the 2200 rpm speed from the data presented in Table V. The useful energy H of the gas is considered to be the sum of the average static pressure head and the velocity head, and the impeller work is $\omega m/g$.

The total flow entering the draft tube is measured with the standard A.S.M.E. long-radius nozzle. The A.S.M.E. Fluid Meter Report was used to determine the variation of the discharge coefficient with the Reynolds number. The discharge was also computed at the impeller outlet

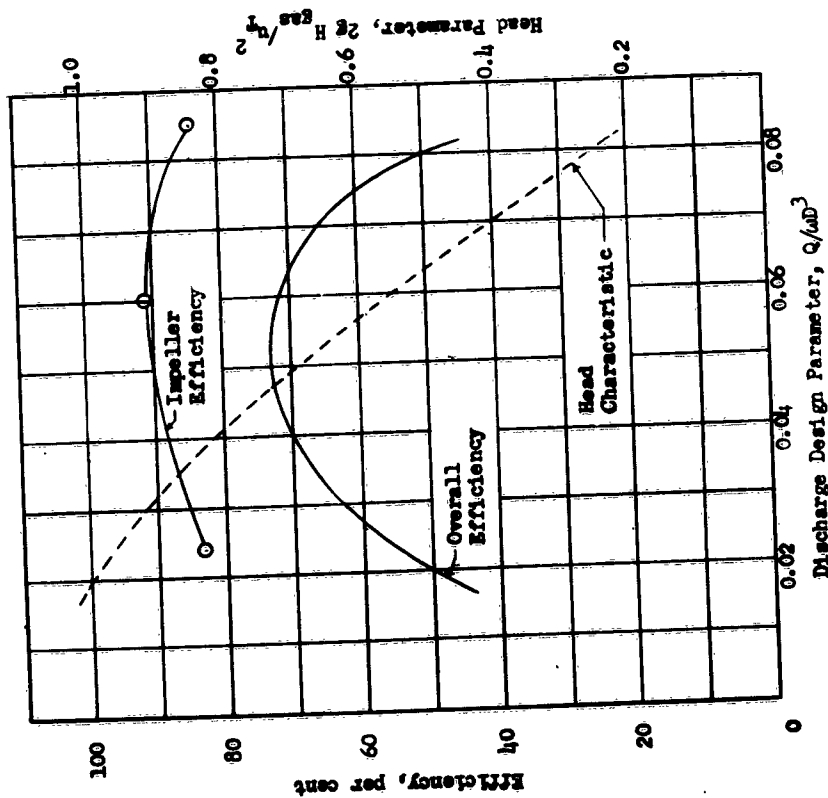


Fig. 31 EFFICIENCY AND HEAD CHARACTERISTIC

Table VI
COMPARISON OF INLET AND OUTLET FLOW RATES

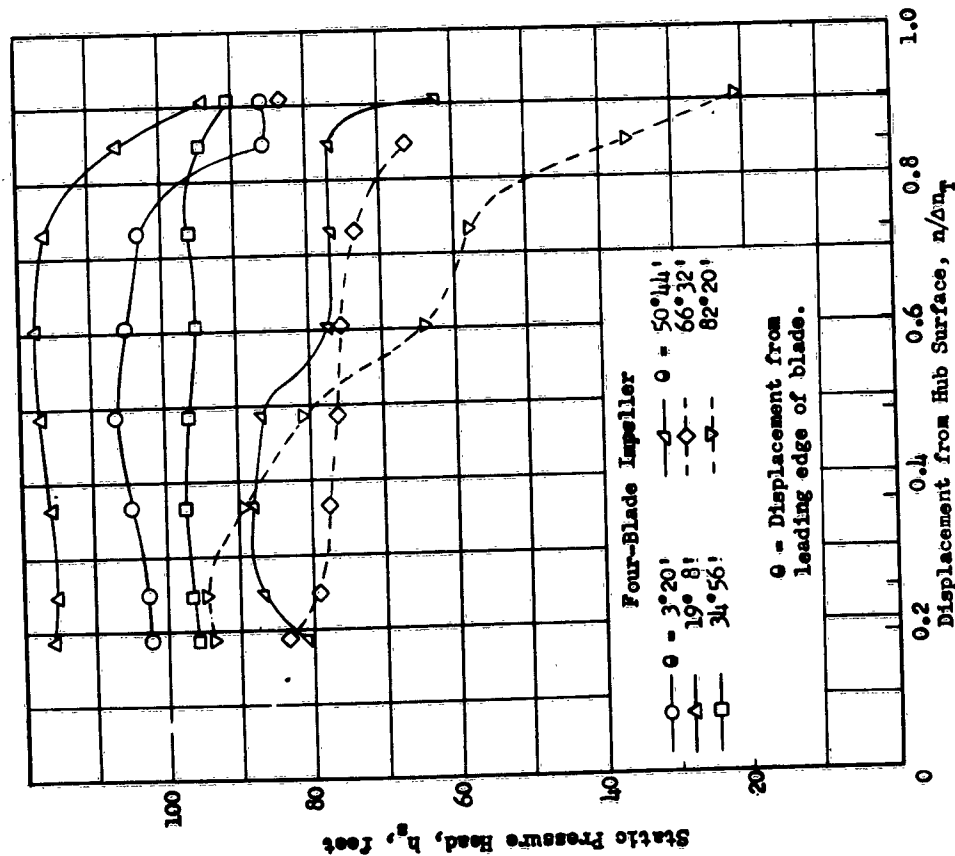
Speed	Draft Tube Reynolds No.	Flow Rate at Inlet Nozzle	Flow Rate at Impeller Outlet (by Numerical Integration)	Discharge Parameter $Q/\omega D^3$
rpm		cfs	cfs	
1500	182,000	20.0	20.7	0.079
1500	132,000	14.6	15.1	.058
2200	275,000	31.3	32.1	.085
2200	198,000	22.3	22.8	.060
2200	75,000	8.7	6.3	.023
3000	385,000	44.1	45.9	.087
3000	279,000	30.8	31.5	.061

by a numerical integration of the meridional velocity distribution. A comparison of the rates of flow, as measured with the nozzle and computed from the velocity survey, is shown in Table VI.

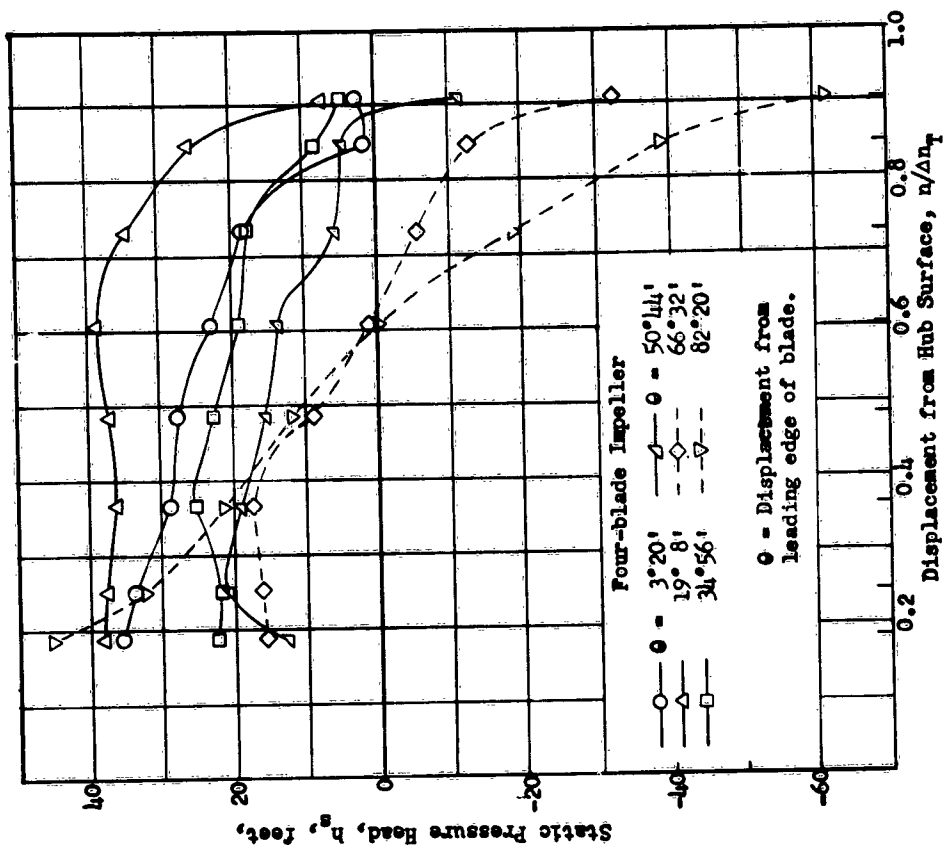
IV. CORRELATION OF THEORY AND EXPERIMENTAL RESULTS

A. Disturbance of Meridional Streamline Pattern

The impeller design is based upon the assumption that at the design condition of $Q/\omega D^3 = 0.060$, the meridional velocity distribution is undisturbed by the presence of the blades. The distribution of the theoretical velocity shows a uniform increase from the hub to the shroud. The velocity at the hub is 13 per cent below the average, and at the shroud the velocity is 16 per cent above the average. Examination of Fig. 25 shows that this general trend for the meridional velocity to increase uniformly from hub to shroud occurs for all of the test runs, and for values of the discharge parameter $Q/\omega D^3$ ranging from 0.023 to 0.087. However, while the shape of the curve does not significantly change, it is displaced in the peripheral direction about ± 10 per cent from the average (theoretical distribution), with the exception of the curve immediately behind the trailing edge of the blade tip ($\theta = 82^\circ 20'$). The meridional velocity distribution just behind the trailing edge is displaced about 20 per cent above the average, and the reduction in the velocity profile due to boundary layer build-up starts at a considerable distance from the shroud. This effect becomes more pronounced at the lower discharge rates, indicating a significant boundary layer buildup at the shroud surface near the trailing edge. The large pressure gradient across the channel from hub to shroud, occurring behind the trailing edge, may indicate an appreciable secondary flow in this region, (Figs. 32 and 33).



(a) Discharge Parameter, $Q/wD^3 = 0.060$



(b) Discharge parameter, $Q/wD^3 = 0.085$

Fig. 32 STATIC PRESSURE VARIATION FROM HUB TO SHROUD AT IMPELLER OUTLET.

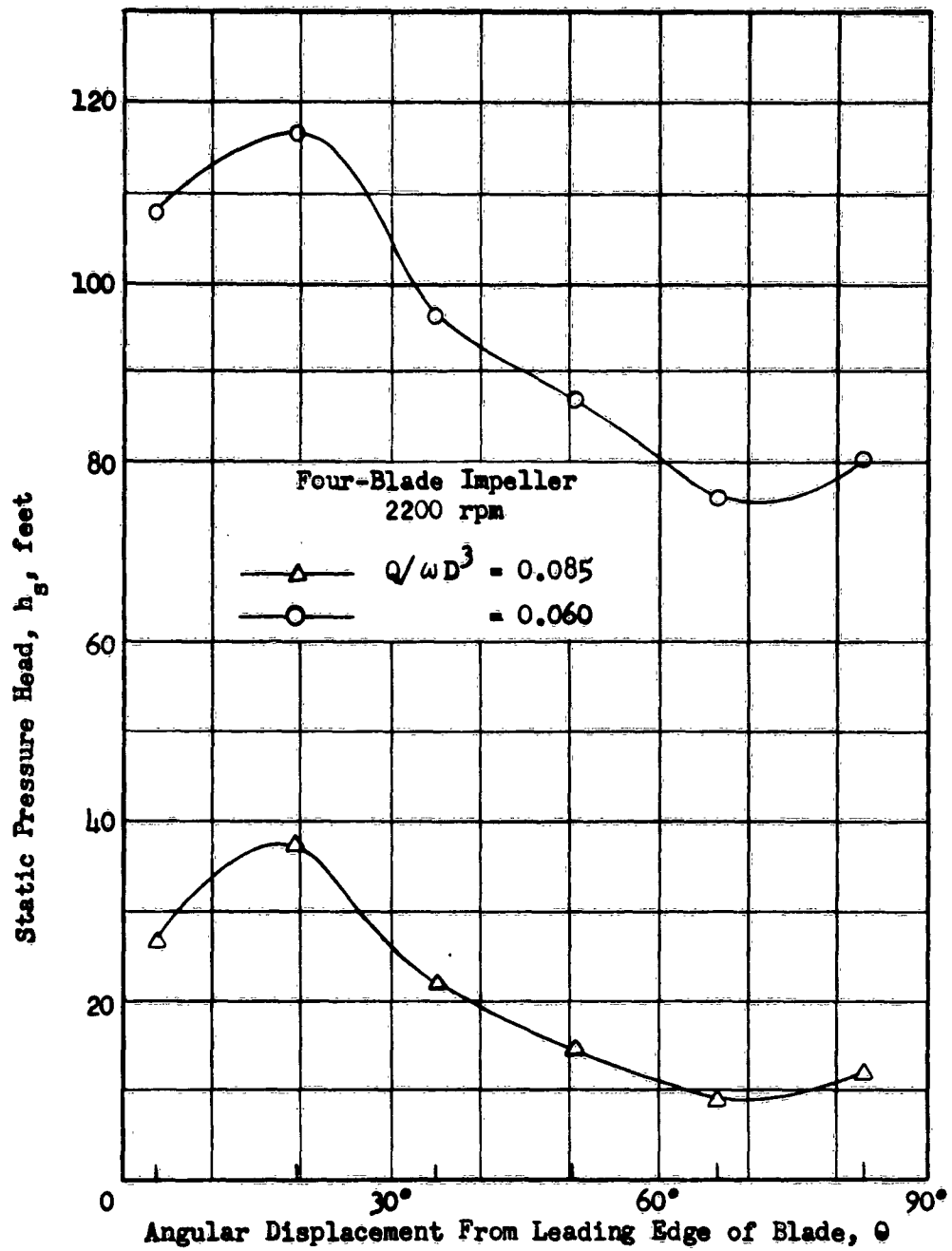


Fig. 33 STATIC PRESSURE VARIATION FROM BLADE TO BLADE ON MEAN STREAM SURFACE AT IMPELLER OUTLET.

B. Similarity Considerations

It is generally accepted that similitude relations are satisfied for turbomachines operating under the conditions of this investigation (Wislicenus¹³, Stanitz¹⁴) in which Mach number and Reynolds number effects are not involved. This means that the velocity diagrams at all points of the flow field will remain similar over a range of speeds, provided the discharge parameter $Q/\omega D^3$ is maintained constant. Comparison of the dimensionless velocity distributions of Figs. 25 and 26, and of the velocity directions shown in Figs. 27 and 28, shows that similitude relations are effectively maintained, and tends to verify the reliability of the measurements. Because of this similarity, it is sufficient to concentrate on the data for one particular speed, 2200 rpm, to study the variations occurring at the design conditions. Complete data at this speed are presented for a range of values of $Q/\omega D^3$ of 0.023, 0.060, and 0.085, which bracket the design value of 0.060.

C. Variation in the Energy and Whirl-Moment Values

According to the infinite blade theory, the energy input, and the increase in the whirl-moment, should be uniformly distributed at the blade outlet. The variation in these values is shown in Figs. 29 and 30. Inspection of the (c) and (d) parts of these figures for the 2200 rpm speed, just above and below the design condition, reveals a small variation of ± 10 per cent (with the exception of the trailing edge of the blade) across the channel from hub to shroud. However, there is a significant variation from blade to blade. This same type of variation has been observed by Hamrick, et al.¹². The maximum energy input occurs at the driving face

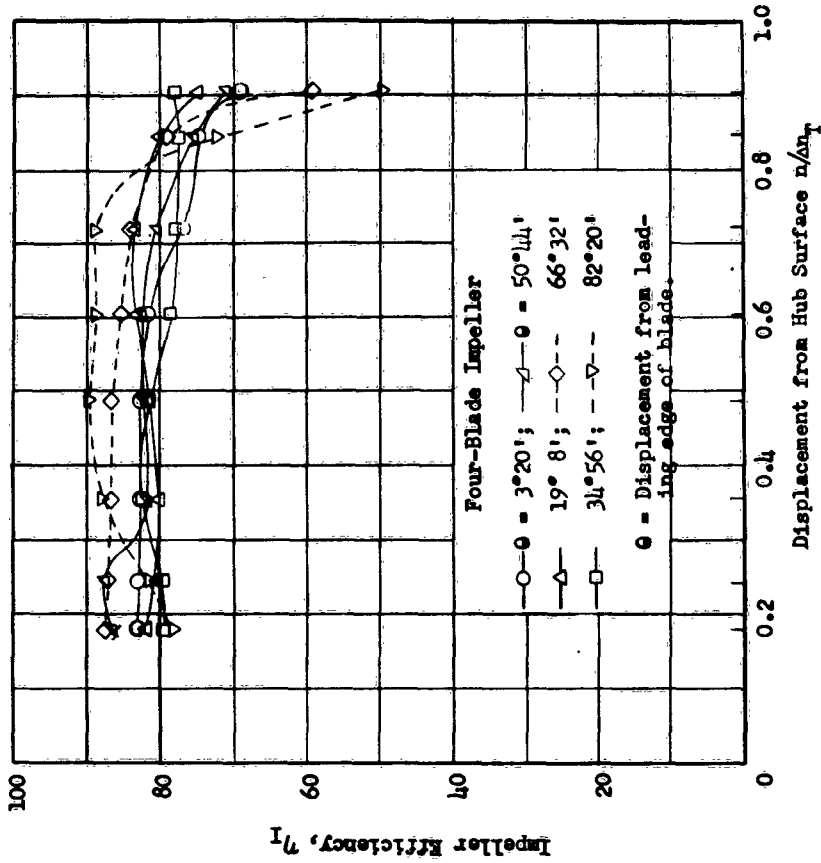
of the blade, supporting the hypothesis made in Reference 12, that "secondary flows in the boundary layer tend to shift the low-energy air toward the blade suction surface".

The value of I should remain constant for isentropic flow, and is a measure of the "loss", which is defined as the difference between the "useful" energy H and the energy input to the gas given by $\omega m/g$. The impeller efficiency is defined as the ratio of these two values. The variation in the impeller efficiency is shown in Fig. 34. These efficiency values include the energy losses in the draft tube. The lowest efficiency occurs near the shroud surface, across the entire passage from blade to blade; the losses are particularly high in the corner formed by the trailing face of the blade and the shroud surface.

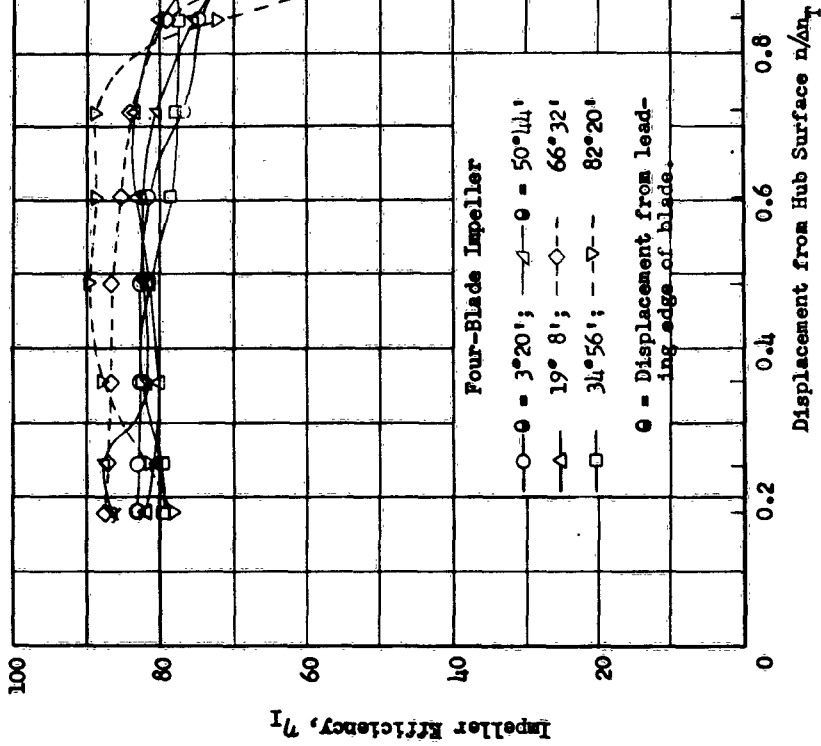
D. Comparison with the Blade to Blade Solution

For the blade to blade solution, it is assumed that the flow proceeds along surfaces of revolution generated by meridional streamlines. Variation of the flow angle δ along the periphery is a measure of the extent that the flow "twists" away from this surface of revolution. Examination of Fig. 29d (2200 rpm, $Q/\omega D^3 = 0.060$) shows that the angle δ varies only about 3 degrees on any given geometric surface of revolution. This indicates that the fluid particles remain essentially on surfaces of revolution for the main flow region between the blades. The uniformity of the flow from hub to shroud indicates that a satisfactory picture of the flow across the entire channel will be derived from values computed for the mean stream surface.

Comparison of the theoretical meridional velocity distribution



(a) Impeller Speed 2200 rpm; $Q/\omega D^3 = 0.060$



(b) Impeller Speed 2200 rpm; $Q/\omega D^3 = 0.085$

FIG. 34. VARIATION OF IMPELLER EFFICIENCY FROM HUB TO SHROUD AT IMPELLER OUTLET.

with the measured results is shown in Fig. 35. It may be observed that the general trend in the measured distribution is similar to the theoretical for all values of the discharge parameter. The measured values do not rise as steeply as the theoretical near the trailing face of the blade. This is most likely caused by unloading of the pressure forces on the blade near the blade tip, because the pressure difference across the blade must become zero at the tip. This hypothesis is supported by the distribution of static pressure from blade to blade, as shown in Fig. 33. The static pressure is observed to be a minimum a short distance from the suction side of the blade, and then increases upon approaching the blade. This indicates the presence of a secondary flow, tending to produce a velocity distribution at the blade outlet, which is more uniform than that computed on the basis of potential theory.

E. The Impeller Slip Factor

The slip factor μ is an important parameter for the determination of the impeller performance, and is defined as the ratio of the average value of the tangential component of the absolute velocity divided by the theoretical value that would be obtained if the fluid were perfectly guided by the vanes. Stodola¹⁵ gives an equation for straight blades,

$$\mu = 1 - 0.500 \Delta\theta ,$$

and, for a blade spacing of 1.502 radians, the slip factor should be 0.249. Stanits¹⁴ is not in agreement with the Stodola correction; he has computed the slip factor by relaxation methods for a series of centrifugal impellers having straight blades, and also for two impellers having

Values of Discharge Parameter, $Q/\omega D^3$

—○—	0.023;	---○---	0.060
—△—	0.038;	---△---	0.061
—□—	0.044;	---□---	0.079
—▲—	0.048;	---▲---	0.085
—◇—	0.050;	---◇---	0.087
—▽—	0.058;	---	theoretical

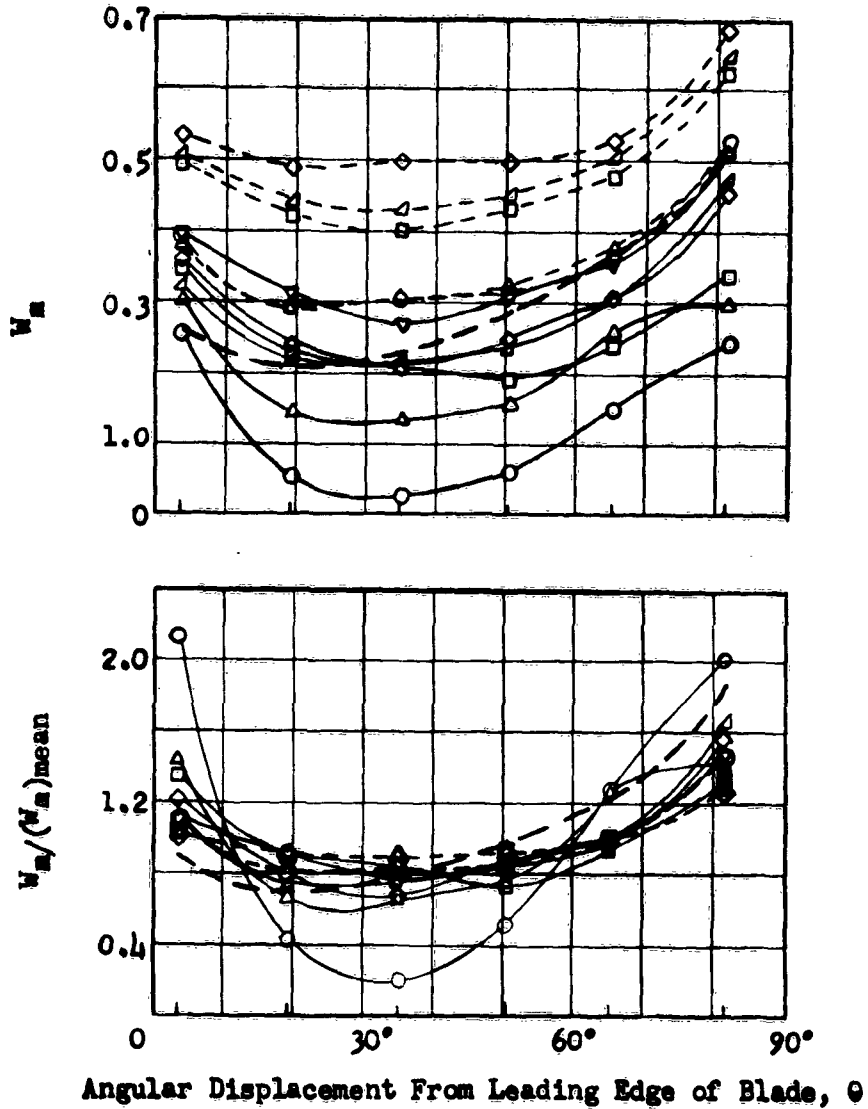


Fig. 35 COMPARISON OF MEASURED AND THEORETICAL MERIDIONAL VELOCITY DISTRIBUTION ON MEAN STREAM SURFACE AT THE IMPELLER OUTLET.

logarithmic-spiral blades of backward curvature, and found

$$\mu = 1 - 0.3154\theta .$$

This equation leads to a slip factor of 0.527 for the four-blade impeller of this investigation. A comparison of the measured slip factors is shown in Fig. 36. This figure indicates that the slip factor depends upon the speed and discharge in an actual impeller, and shows a variation of nearly ± 12 per cent about a median value of 0.571, leading to an equation for the slip factor,

$$\mu = 1 - 0.304\theta ,$$

which is in close agreement with the theoretical relationship of Stanitz.

F. Overall Performance

The large deviation between the impeller efficiency and the overall efficiency shown in Fig. 31, particularly at low flow rates, indicates the existence of eddy motion within the impeller. * The existence of an eddy attached to the driving face of the impeller at low flow rates is theoretically shown by Stanitz¹⁶. Reverse flow on the driving face is also indicated for flow solutions at low weight flows by Prian and Michel¹⁷ but direct experimental evidence of the eddy was not found. A possible explanation, offered in reference (12), is that the flow is unstable, and that instantaneous eddies will form and be washed away, somewhat in the manner of rotating stall observed in axial-flow compressors. Detection of this phenomena is not possible with the spherical pitot-probe, as this instrument will only give a time average of the total pressure, and

* See reference (12)

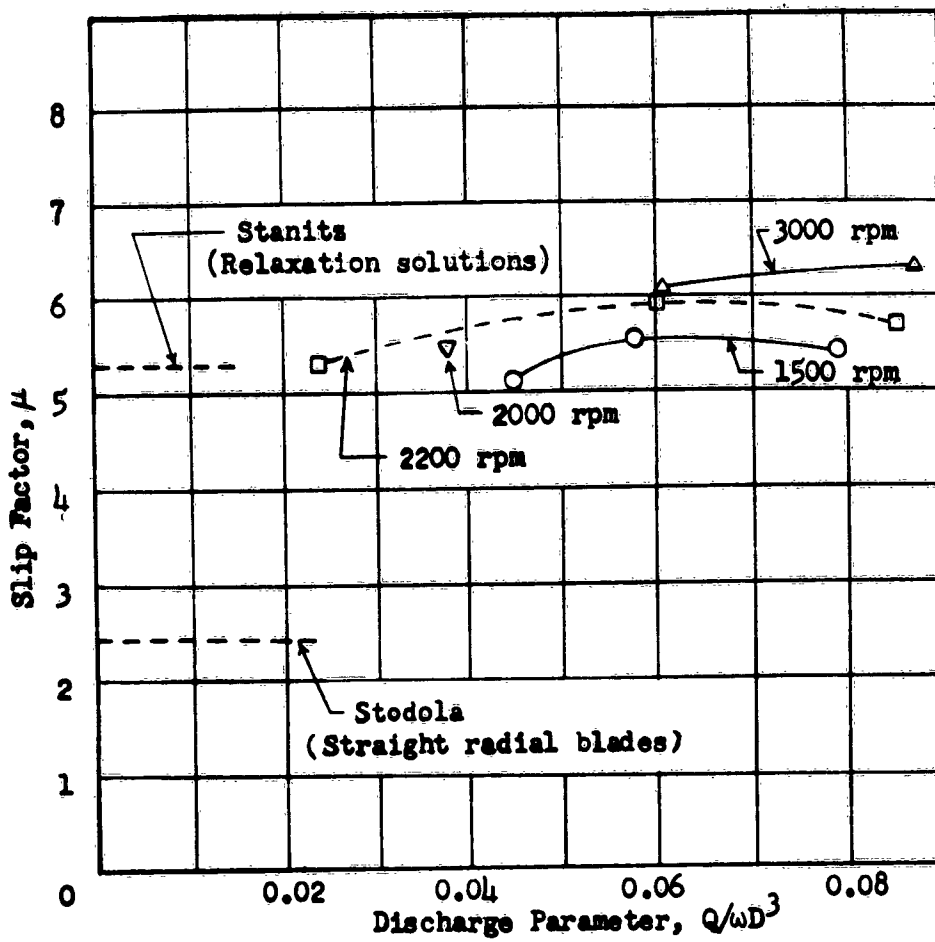


Fig. 36 IMPELLER SLIP FACTOR

this time-average is impossible to interpret in areas of rapidly changing flow direction. This instability may explain the discrepancy in the total flow rate as measured at the inlet nozzle, and computed by numerical integration at the impeller outlet, shown in Table VI, at the low rate of flow. The integrated value is nearly 27 per cent lower than the value measured at the nozzle.

V. SUMMARY AND CONCLUSIONS

A four-blade, mixed-flow impeller has been designed on the basis of axisymmetric flow conditions derived from the assumption of an infinite number of blades. The flow distribution at the outlet of this impeller has been measured with a spherical pitot-probe mounted on the impeller, and the results of these measurements are presented in graphical form. Comparisons between the theoretical flow distributions and the measured distributions have been made, and the following conclusions are drawn.

1. The shape of the meridional velocity distribution remains essentially unchanged from the theoretically predicted shape based upon the assumption of axial symmetry, in spite of the small blade number (four) of the impeller. However, in the blade to blade direction, the meridional distribution is displaced as much as 20% above and 10% below the average. This trend is observed for a range of the discharge parameter $Q/\omega D^3$ from 0.023 to 0.085.

2. The blade surface is considered to be a bound-vortex sheet with a zero ring-component of vorticity. This means the blades do not induce velocity components which disturb the meridional velocity distribution at the design condition. The observed conformity of the meridional velocity

distribution with the theoretical distribution for potential through-flow in the annular space formed by the hub and shroud surfaces, tends to verify the vortex theory of the flow.

3. The fluid particles remain essentially on surfaces of revolution generated by the meridional streamlines. Variations in the cone angle δ of the relative velocity are of the order of only 2 and 3 degrees in the peripheral direction. This substantiates the underlying assumption of the quasi-three-dimensional relaxation solutions of the flow.

4. The observed blade-to-blade velocity distribution is more uniform than the distribution computed by relaxation methods. This may be due to the large blade spacing, and the necessary blade unloading near the tip which tends to increase the pressure at the suction (trailing) face of the blade, and decrease the pressure on the driving (leading) face of the blade. This unloading tends to smooth out the abrupt velocity change across the blade, as is indicated by the relaxation solution.

5. Low energy air tends to shift towards the suction side of the blades, which coincide with observations made by other investigators^{12, 17}. This shift is apparently caused by secondary flows in the boundary layer, and may account for the discrepancy in the relaxation solution near the blade surface.

6. The impeller slip factor varies nearly 12 per cent about a median value of 0.57, over a range of speeds (1500 to 3000 rpm) and discharge rates ($Q/\omega D^3 = 0.023$ to 0.085). The measured slip factor compares favorably with a theoretical value of 0.53 given by Stanitz, but is in disagreement with the value of 0.25 computed from the Stodola equation for centri-

fugal impellers having straight blades.

Regarding the experimental technique applied during the investigation, it can be concluded that consistent and reproducible surveys of the internal flow distribution can be obtained with a directional pitot-probe mounted on the impeller and used in conjunction with a mercury-seal type of pressure-transfer device. The readings become unreliable if flow instabilities resulting from separation and eddy motion are present.

APPENDIX A

SYMBOLS

I. COORDINATE SYSTEMS

- (r, θ, z) Cylindrical coordinates rotating with the impeller
- (R, Θ, Z) Dimensionless cylindrical coordinates, where
 $R = r/D$, $Z = z/D$
- (s, n, θ) Meridional coordinates indicating the arc-length along a meridional streamline, the normal to the meridional streamline (positive towards the center of curvature), and the angular location around the impeller axis of rotation.
- (S, N, θ) Dimensionless meridional coordinates, where
 $S = s/D$, $N = n/D$
- (ξ, η) Orthogonal coordinates on the mean stream surface defined by equation 39.

II. VECTORS

Vectors are indicated by a bar over the letter. The vector product is indicated by a cross \times , and the scalar product by a dot \cdot .

III. VELOCITIES

- \bar{c} Absolute velocity of a fluid particle, $\bar{c} = \bar{u} + \bar{w}$
- \bar{u} Peripheral velocity of a point of the rotating impeller,
 $u = r\omega$
- \bar{w} Velocity of a fluid particle relative to the impeller.
- ω Angular speed of the impeller.
- C, W Dimensionless velocities, $C = \frac{c}{\omega D/2}$, $W = \frac{w}{\omega D/2}$

IV. OPERATORS

- \exp Exponential, ($\exp x = e^x$)
- ∇ Gradient vector operator
- ∇^2 Laplacian operator, ($\nabla \cdot \nabla$)

$\frac{D}{dt}$ Differentiation following the motion of the fluid,
$$\frac{D}{dt} = \frac{\partial}{\partial t} + \bar{w} \cdot \nabla$$

δ Small incremental variation

Δ Increment

V. INDICES

r,t,s Represent components in the radial, tangential and axial directions respectively

s,n Represent components in the meridional coordinate system

m Component in the meridional plane

rel Relative to the blade cascade

(Other indices used are explained in the text, or are considered as part of the definition of the symbol.)

VI. SPECIAL NOTATIONS FOR THE SPHERICAL PITOT-PROBE (See Fig. B1)

(x',y',z') Rectangular coordinates fixed to spherical pitot-probe with x'-axis along the sphere axis, and y'-axis parallel to the cross-piece.

$\bar{i}, \bar{j}, \bar{k}$ Unit vectors in the (x',y',z') system

$\bar{e}_r, \bar{e}_t, \bar{e}_z$ Unit vectors in the (r, θ ,z) system

α Conical angle formed by the four symmetrical pressure holes and the probe-axis (x'-axis).

β_p Angle between the probe-axis (x'-axis) and the tangential direction (t-direction)

γ_n Angle between the relative velocity vector and any pressure hole (n) on the spherical probe-head.

δ' Dihedral angle between the plane containing the incident relative velocity and the meridional plane of the spherical probe-head.

ϕ Conical angle formed by the relative velocity and the probe-axis (x'-axis)

$\cos(x',r)$ The direction cosine between the x' and r-axis, etc.

VII. OTHERS

\bar{a}	Acceleration vector of a fluid particle
B	Dimensionless height of axial-symmetry flow channel formed by stream surfaces adjacent to the surface of revolution generated by the mean meridional streamline, $B = \Delta n / \Delta n_{\text{blade}}$
c_{m0}	Absolute meridional velocity component at the hub surface ($n=0$)
D	Maximum diameter at blade outlet-edge
$F(r,z)$	Function defining the blade surface
$f(\xi), g(\xi)$	Functions defined by equations (45) and (46)
g	Acceleration of gravity
H	Total head input to fluid (specific energy), $H = \frac{c^2}{2g} + \frac{1}{g} \int \frac{dp}{\rho}$
h_s	Static pressure head
h	Relaxation grid spacing
I	$H - \frac{\omega}{g} m$
k	Fictive distributed blade force per unit volume (for infinite number of blades)
m	Whirl-moment, $m = rc_t$
\bar{n}	Normal vector to the blade surface
Δn	Spacing between hub and shroud surfaces along orthogonal in the meridional plane
p	Pressure
Q	Volume rate of flow through impeller
Q_n	Volume rate of flow between the hub surface and the stream surface of revolution generated by meridional streamline (n)
R_o	Residual (error in finite-difference equation due to incorrectly estimated function values.)

t	Time
β	Angle between relative fluid velocity and negative blade velocity, between \bar{w} and $(-\bar{u})$
Γ	Circulation
δ	Cone angle formed by direction of meridional component of relative fluid velocity with impeller axis (between w_m and z)
η_I	Impeller efficiency, $\eta_I = gH/\omega m$
λ	Absolute vorticity
λ_b	Absolute bound vorticity
λ_f	Absolute free vorticity
μ	Impeller slip factor, $\mu = \frac{(C_t)_{\text{average}}}{(C_t)_{\text{theoretical}}}$
ρ	Fluid mass per unit volume
ψ	Stream-function defined by equation (38)
$\Delta\psi$	Change in ψ at grid points
Ψ	Dimensionless stream-function indicating the quantity of flow passing between the Ψ -streamline and the leading face of the blade, expressed as a percentage of the flow between two blades, $\Psi = 100 \frac{\psi}{\Delta\psi}$

APPENDIX B

THE THREE DIMENSIONAL SPHERICAL PITOT PROBE

1. Theoretical Calibration Curves

The theoretical relationship between the relative velocity of the free-stream at a point, and the pressure readings given by the five holes of the spherical probe-head of Fig. (B1) if it is inserted into the stream at this given point, will be derived. As usual, the fluid will be assumed to be nonviscous, incompressible, and steady relative to the probe, so that the Bernoulli Equation will apply between a point in the free stream and hole (n) on the sphere,

$$p + \frac{\rho W^2}{2} = p_n + \rho \frac{w_n^2}{2}; \quad n = 0, 1, 2, 3, 4. \quad (B1)$$

Solving this equation for the pressure at hole (n) yields,

$$\begin{aligned} p_n &= p + \rho \frac{W^2}{2} \left[1 - \left(\frac{w_n}{W} \right)^2 \right] \\ &= p + k_n \rho \frac{W^2}{2}. \end{aligned}$$

The pressure recovery factor, $k_n = 1 - \left(\frac{w_n}{W} \right)^2$, is a function of the Reynolds number and the orientation, given by the angle γ_n , of the hole with respect to the stream. However, this factor becomes independent of the Reynolds number for sufficiently high velocities, and is only a function of γ_n , which can be expressed in terms of the two angles ϕ and δ' . By combining the equations for the pressure at each of the five holes, the following ratios may be obtained:

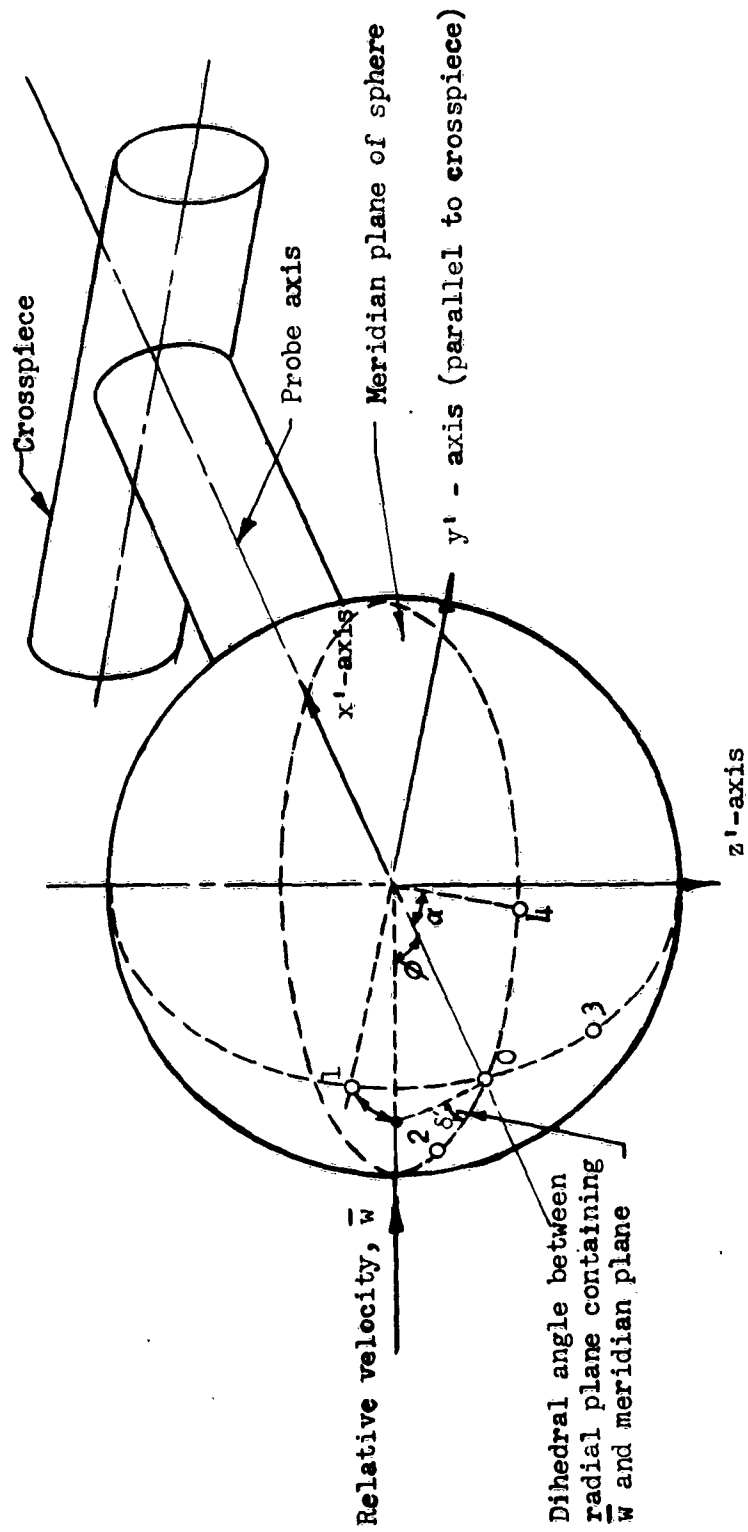


Fig. B1 NOTATION FOR SPHERICAL PROBE-HEAD

$$\frac{k_1 - k_3}{k_0 - k_3} = \frac{p_1 - p_3}{p_0 - p_3} = X_{133}(\phi, \delta'), \quad (B3)$$

$$\frac{k_2 - k_4}{k_0 - k_3} = \frac{p_2 - p_4}{p_0 - p_3} = Y_{243}(\phi, \delta'). \quad (B4)$$

Each of these ratios may be determined experimentally by measuring the pressure differences occurring between the corresponding holes on the pitot sphere for a known orientation of the probe with respect to the free-stream velocity vector. The two functions of equations (B3) and (B4) implicitly give ϕ and δ' , which determine the direction of the velocity, in terms of the ratios, $(k_2 - k_4)/(k_0 - k_3)$ and $(k_1 - k_3)/(k_0 - k_3)$.

These ratios have finite values if δ' is in the range $0 < \delta' < 180^\circ$ (Fig. B1). But in the range $-180^\circ < \delta' < 0$, the ratios become infinite when the vector makes equal angles with holes 0 and 3. For this reason, and also for the sake of symmetry, the graph of the two ratios defining flow direction and velocity is divided into two halves, $0 < \delta' < 180^\circ$, and $-180^\circ < \delta' < 0$. For the first half, the ratios given by equations (B3) and (B4) are used. For the second half, the ratios used are:

$$\frac{k_1 - k_3}{k_0 - k_1} = \frac{p_1 - p_3}{p_0 - p_1} = X_{131}(\phi, \delta'), \quad (B7)$$

$$\frac{k_2 - k_4}{k_0 - k_1} = \frac{p_2 - p_4}{p_0 - p_1} = Y_{241}(\phi, \delta'). \quad (B8)$$

The theoretical determination of the above ratios of the pressure recovery factors may be based upon potential flow around a sphere. For this case, the velocity at any point on the sphere surface, corresponding

to a radial line forming an angle γ_n with the w-direction, is given by the equation

$$w_n = \left(\frac{3}{2} \sin \gamma_n\right) w . \quad (B7)$$

This means that the pressure recovery factor at hole (n) for potential flow is given by

$$k_n = 1 - \frac{9}{4} \sin^2 \gamma_n, \quad (B8)$$

and the ratio of the pressure recovery factors is

$$\begin{aligned} \frac{k_1 - k_3}{k_0 - k_3} &= \frac{\sin^2 \gamma_3 - \sin^2 \gamma_1}{\sin^2 \gamma_3 - \sin^2 \gamma_0} \\ &= \frac{\cos^2 \gamma_1 - \cos^2 \gamma_3}{\cos^2 \gamma_0 - \cos^2 \gamma_3} \end{aligned} \quad (B9)$$

The ratios of the other pressure recovery factors are given by similar expressions.

The angle γ_n is related to ϕ and δ' by the equations of spherical trigonometry,

$$\begin{aligned} \cos \gamma_0 &= \cos \phi , \\ \cos \gamma_1 &= \cos \phi \cos \alpha + \sin \alpha \sin \delta' \sin \phi , \\ \cos \gamma_2 &= \cos \phi \cos \alpha + \sin \alpha \cos \delta' \sin \phi , \\ \cos \gamma_3 &= \cos \phi \cos \alpha - \sin \alpha \sin \delta' \sin \phi , \\ \cos \gamma_4 &= \cos \phi \cos \alpha - \sin \alpha \cos \delta' \sin \phi . \end{aligned} \quad (B10)$$

Making use of these relations, the functions representing the theoretical ratios of the pressure recovery factors are

$$X_{133} = \frac{2 \sin 2\alpha \sin \delta' \sin 2\phi}{2 \sin^2 \alpha (\cos^2 \phi - \sin^2 \delta' \sin^2 \phi) + \sin 2\alpha \sin \delta' \sin 2\phi} \quad (B11)$$

$$Y_{243} = \frac{2 \sin 2\alpha \cos \delta' \sin 2\phi}{2 \sin^2 \alpha (\cos^2 \phi - \sin^2 \delta' \sin^2 \phi) + \sin 2\alpha \sin \delta' \sin 2\phi} \quad (B12)$$

These ratios are plotted in Fig. B2. Because of perfect symmetry, only the first quadrant, in which δ' ranges from zero to 90 degrees is shown.

The above functions are used to determine the direction of the velocity. The magnitude of the velocity may be determined by applying the general pressure equation to the center hole, and to any one of the other four holes, say hole (3), which will give the equation

$$P_0 - P_3 = \rho \frac{w^2}{2} (k_0 - k_3).$$

From this, the velocity is

$$w = \sqrt{\frac{2}{\rho} \frac{P_0 - P_3}{k_0 - k_3}}. \quad (B13)$$

Equation (B8) and (B10) may be used to determine the theoretical relation of $(k_0 - k_3)$ to ϕ and δ' ,

$$\begin{aligned} k_0 - k_3 &= \frac{9}{4} (\cos^2 \gamma_0 - \cos^2 \gamma_3) \\ &= \frac{9}{4} \left[\sin^2 \alpha (\cos^2 \phi - \sin^2 \delta' \sin^2 \phi) + \frac{1}{2} \sin 2\alpha \sin 2\phi \sin \delta' \right] \quad (B14) \end{aligned}$$

After the magnitude and direction of the relative velocity has been determined, the static pressure of the free stream is given directly by

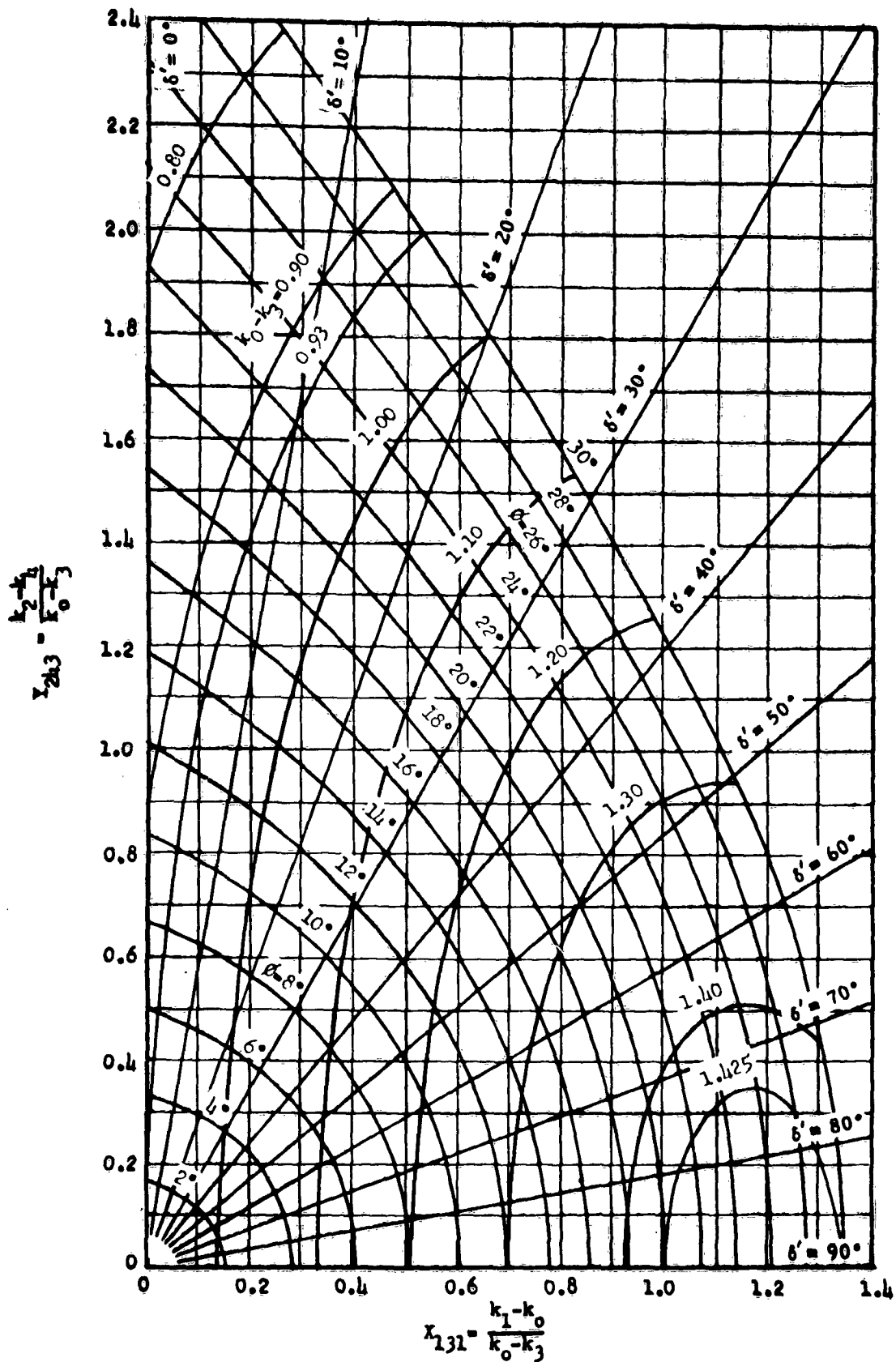


Fig. B2 THEORETICAL CALIBRATION CURVES FOR THE 5-HOLE SPHERICAL PITOT-PROBE

applying equation (B2) to the center hole,

$$p = p_0 - k_0 \rho \frac{w^2}{2} . \quad (B15)$$

The theoretical value of k_0 is given by equation (B8), where γ_0 is identical to the cone angle ϕ ,

$$k_0 = 1 - \frac{9}{4} \sin^2 \phi . \quad (B16)$$

2. Experimental Calibration Curves

The spherical probe was calibrated in the test stand shown schematically in Fig. B3. The calibration fixture consists of two concentric rings in a gimble mounting. The bottom ring is pivoted along its diameter in the table-mounting, with the pivot-axis perpendicular to the nozzle-axis. The tilting angle is measured with a protractor on the pivot-axis, and is equal to the cone angle ϕ between the velocity vector of the flow and the shaft-axis of the probe. The top ring rotates over the bottom ring, which has protracted angular divisions, to measure the dihedral angle δ' . The probe is mounted on the top ring with its axis coinciding with the ring-axis, and with the center of the spherical probe on the pivot-axis of the bottom ring. By this arrangement, the center of the sphere remains on the nozzle-axis and fixed in position, for any change of cone angle and dihedral angle. Thus, as these angles are changed, the error caused by non-uniformity of the velocity distribution of the air emerging from the nozzle is minimized.

Two spherical probes were designed and calibrated. The constructional details of the first probe that was used are shown in Fig. B4a.

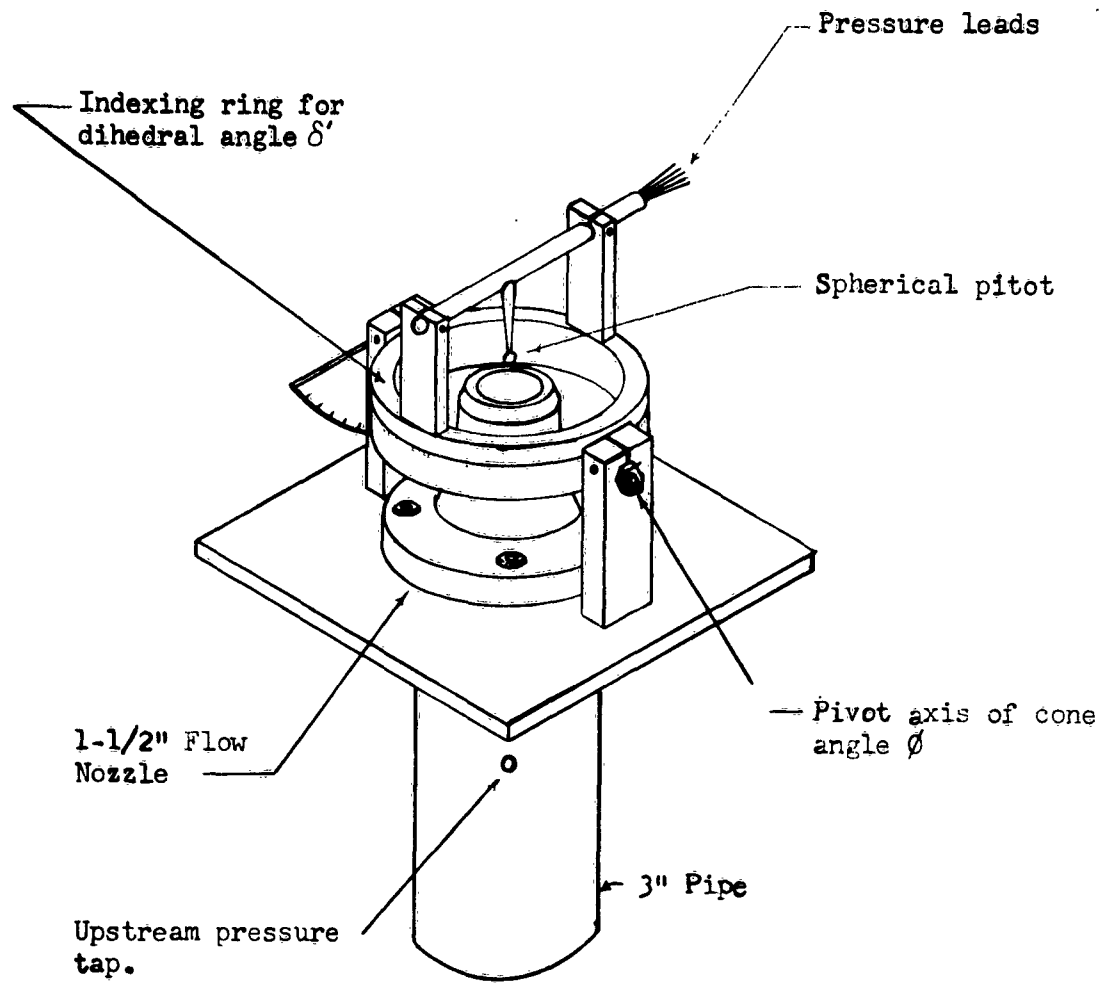
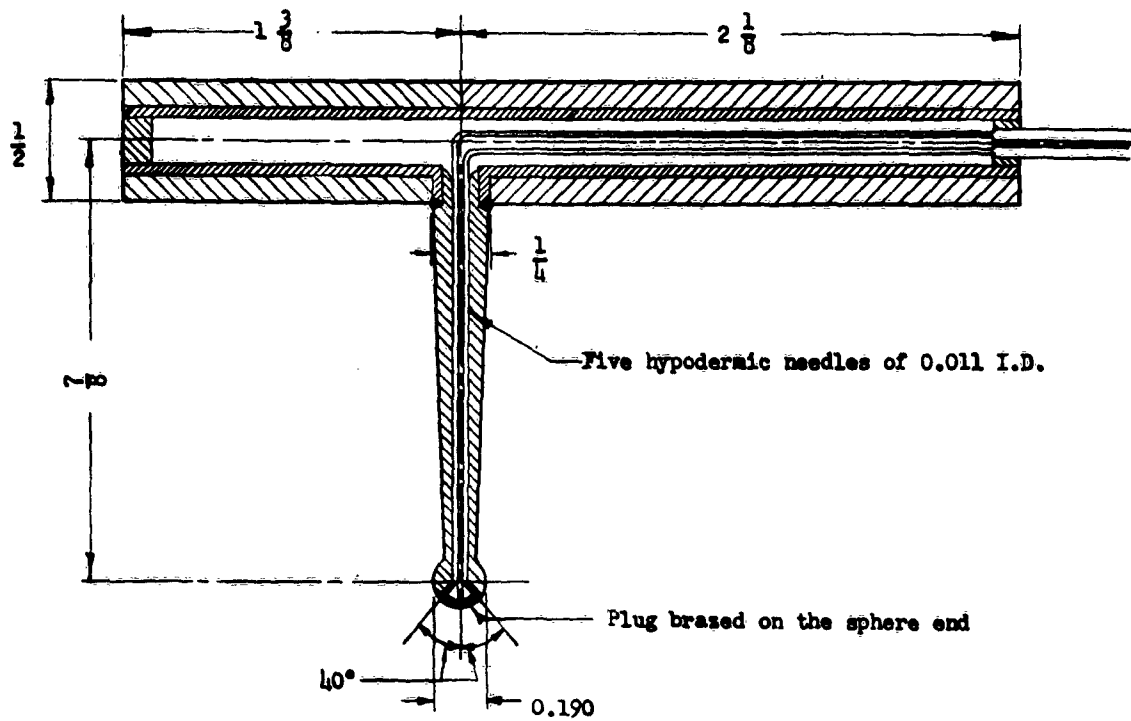
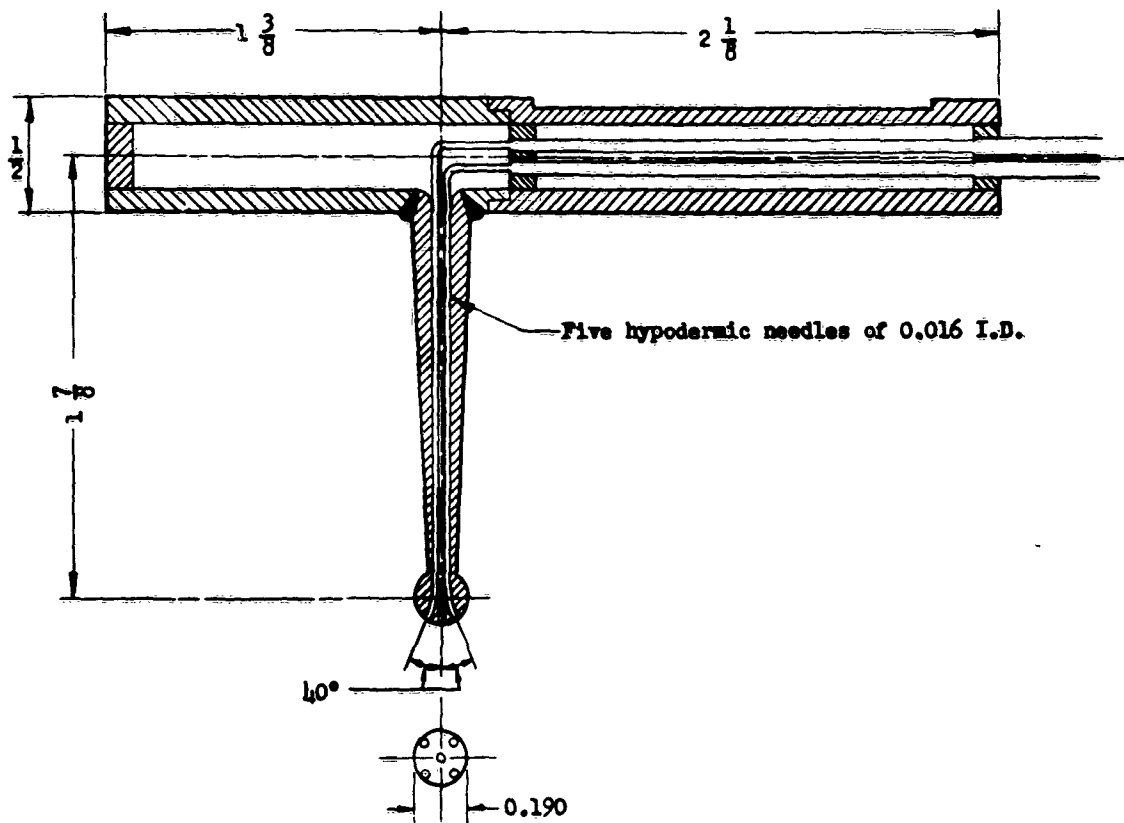


Fig. B3 SPHERICAL PITOT-PROBE CALIBRATION FIXTURE.



(a) Orifice Diameter of 0.011 inch



(b) Orifice Diameter of 0.016 inch

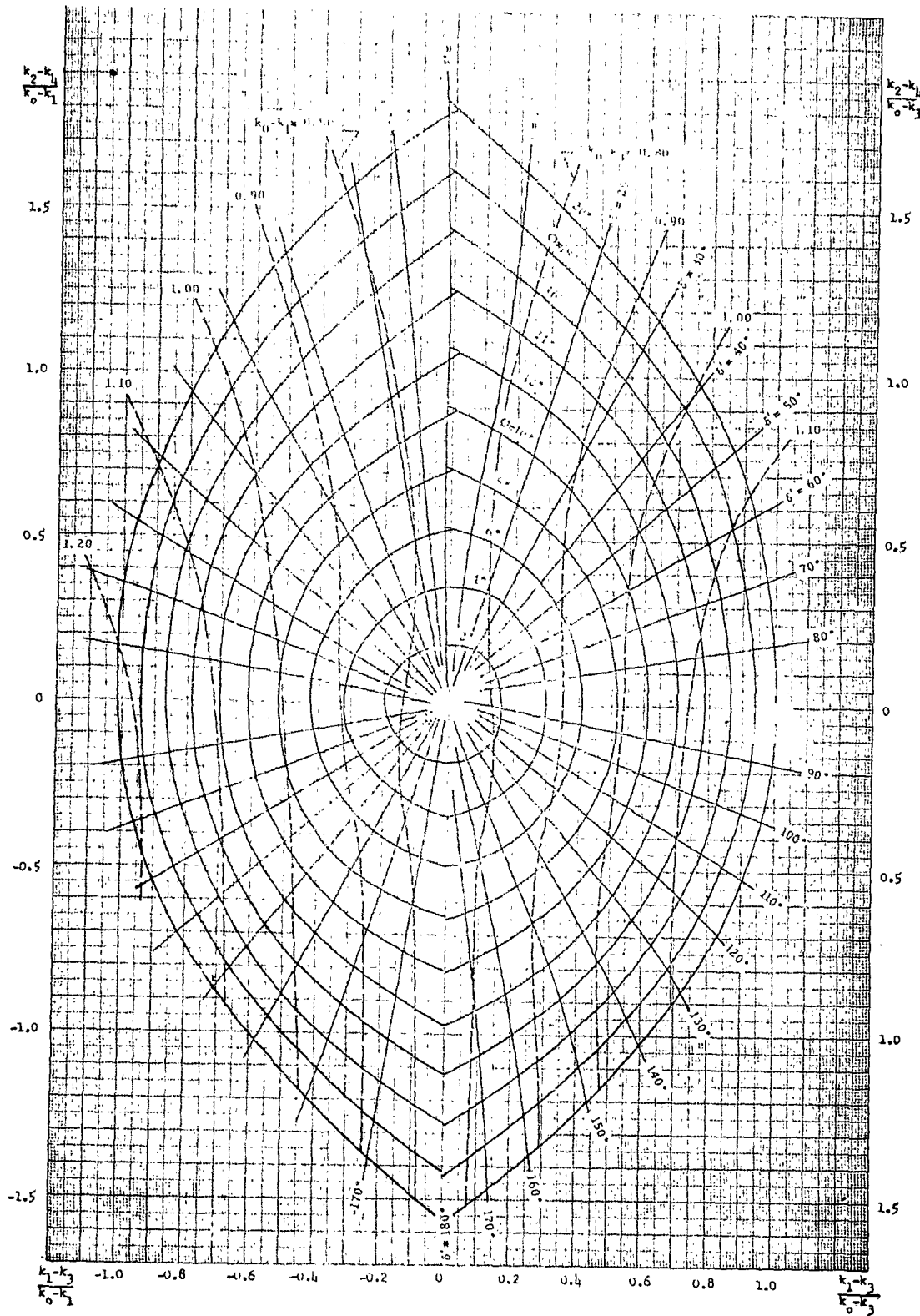
Fig. B4 CONSTRUCTIONAL DETAILS OF SPHERICAL PITOT

The inside diameter of the hypodermic-needle tubing is 0.011 inch. The high resistance caused by this rather long length of small tubing resulted in a slow response time for the instrument. A second probe was designed having a shorter length of small-diameter tubing, and the inside diameter was increased from 0.011 inch to 0.016 inch. The details of this second probe are shown in Fig. B4b. The original probe could be locked in only one position, which was not adequate to cover the wide variations encountered in the exit flow angles. Guided by the measurements obtained with the original probe, two flats were ground on the crosspiece of the second probe so that it could be locked in the two most favorable positions.

The experimental calibration curves for the original pitot-probe are shown in Figs. B5a and B6a, and for the second modified probe in Figs. B5b and B6b. The general trend of these experimental curves conforms to the theoretical curves, more closely at small angles of ϕ , and for increasing angles, the experimental curves become markedly different from the theoretical. By comparing the calibration of the two different probes, one may derive a measure of the individual discrepancies that can be expected in probes that have the same specified dimensions. On the basis of this comparison, if flow angles are to be measured within an accuracy of the order of one or two degrees, it is necessary to calibrate each instrument separately.

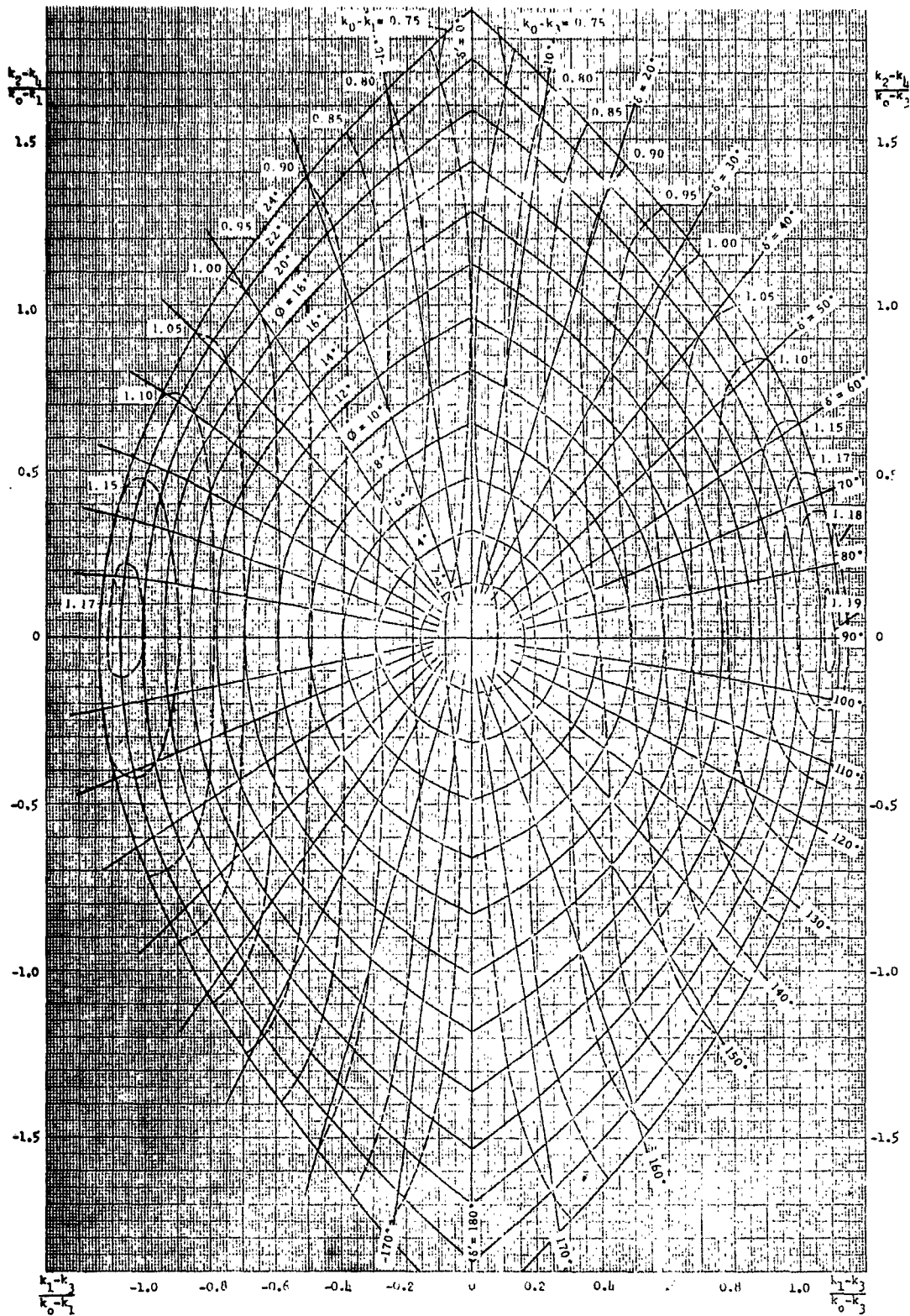
3. Relation of the Probe to the Impeller Geometry

The calibration curves of the spherical pitot-probe will give the magnitude and direction of the fluid velocity relative to the probe. It is necessary to express this measured velocity in relation to the blade



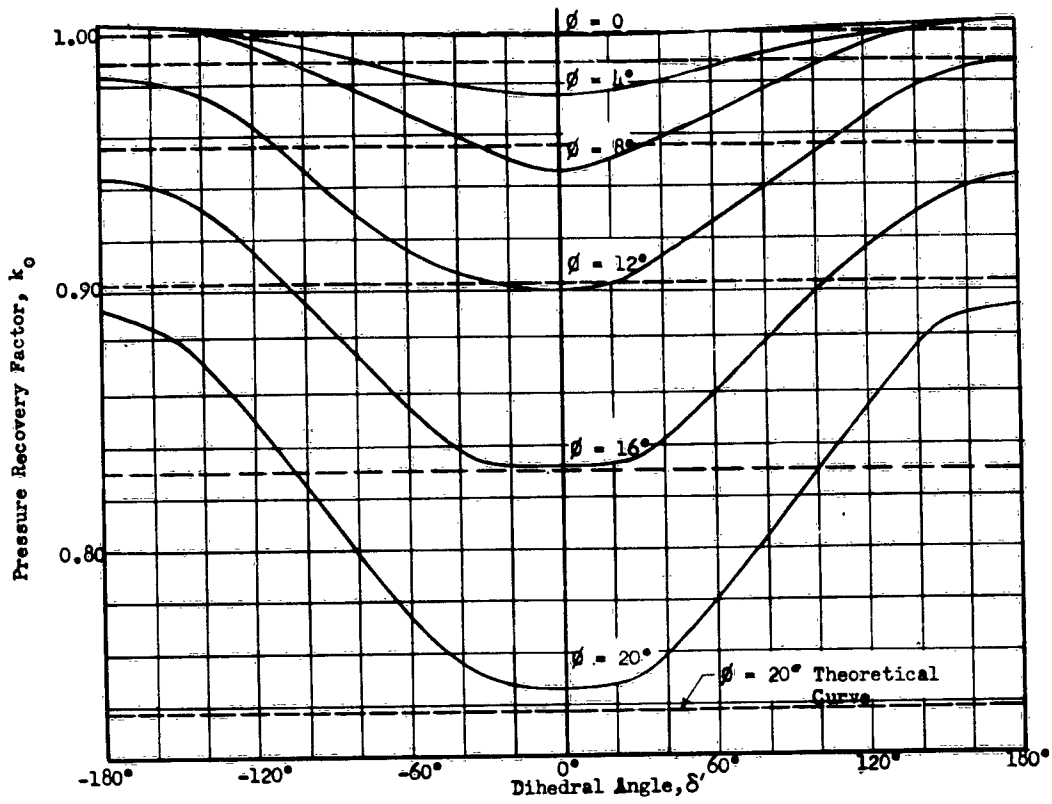
(a) Orifice Diameter of 0.011 Inch

Fig. B5 CALIBRATION OF SPHERICAL PITOT FOR DETERMINATION OF MAGNITUDE AND DIRECTION OF FLOW.

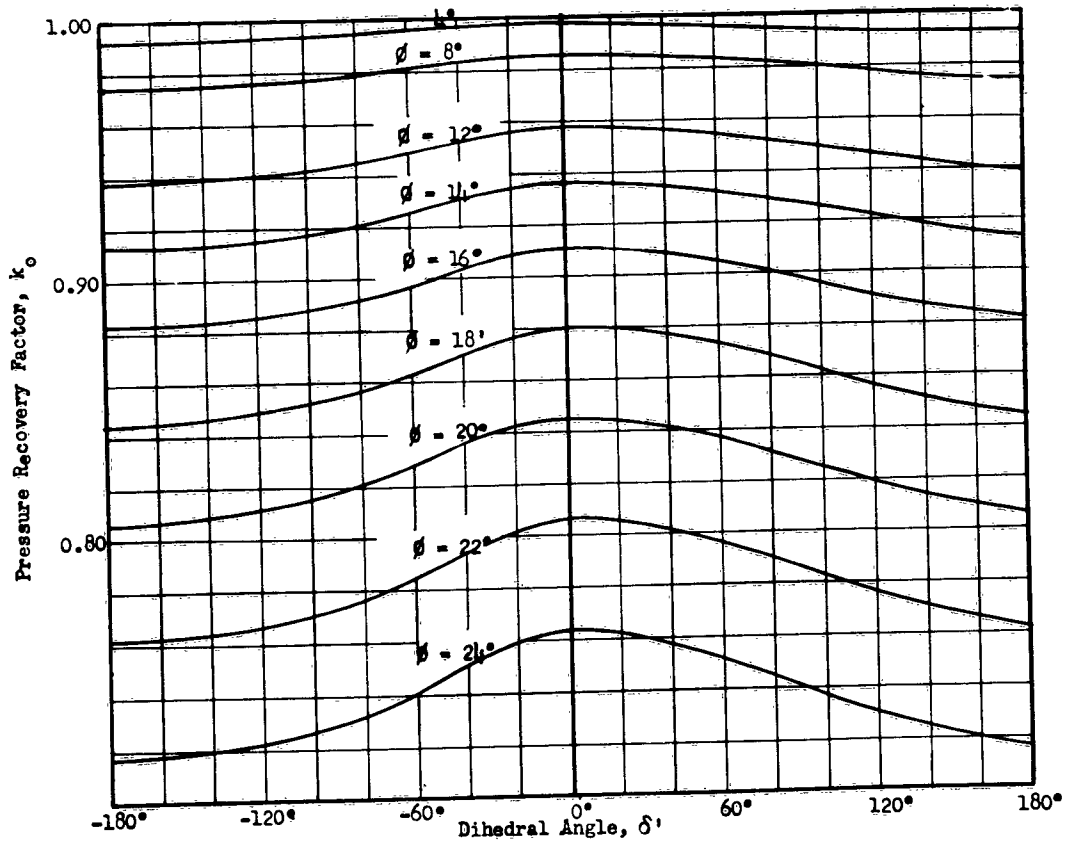


(b) Orifice Diameter of 0.024 Inch

Fig. B5 (Concluded) CALIBRATION OF SPHERICAL PITOT FOR DETERMINATION OF MAGNITUDE AND DIRECTION OF FLOW



(a) Orifice diameter 0.011 inch



(b) Orifice Diameter 0.016 inch

Fig. B6 CALIBRATION OF SPHERICAL PITOT FOR DETERMINATION OF STATIC PRESSURE.

cascade. To do this requires a transformation from the coordinates (x', y', z') fixed to the pitot-probe, to the impeller coordinates (r, θ, z) . Referring to Fig. B1 in conjunction with Fig. 24, the following direction cosines are immediately evident:

$$\cos(y', z) = -\cos 21^\circ 12' = -0.9323,$$

$$\cos(y', r) = \sin 21^\circ 12' = 0.3616,$$

$$\cos(y', t) = \cos 90^\circ = 0,$$

$$\cos(x', t) = \cos \beta_p,$$

$$\cos(z', t) = \sin \beta_p.$$

Additional direction cosines may be derived from the Lagrange Identity for the expansion of the vector multiplication,

$$(\bar{e}_t \times \bar{i}) \cdot (\bar{e}_r \times \bar{e}_t) = (\bar{e}_t \cdot \bar{e}_r) (\bar{i} \cdot \bar{e}_t) - (\bar{e}_t \cdot \bar{e}_t) (\bar{i} \cdot \bar{e}_r). \quad (B17)$$

As $(\bar{e}_t \times \bar{i}) = \sin \beta_p \bar{j}$ and $\bar{e}_r \times \bar{e}_t = \bar{e}_z$, equation (B17) becomes

$$\sin \beta_p (-\cos 21^\circ 12') = 0 - \cos(x', r),$$

and so

$$\cos(x', r) = 0.9323 \cos \beta_p.$$

The remaining direction cosines are derived from the relations

$$\cos(x', t) \cos(x', r) + \cos(y', t) \cos(y', r) + \cos(z', t) \cos(z', r) = 0,$$

$$\cos(x', r) \cos(y', r) + \cos(x', t) \cos(y', t) + \cos(x', z) \cos(y', z) = 0,$$

$$\cos(y', r) \cos(z', r) + \cos(y', t) \cos(z', t) + \cos(y', z) \cos(z', z) = 0,$$

and there is obtained

$$\cos(z',r) = -\sin\beta_p \cos 21^\circ 12' = -0.9323 \sin\beta_p$$

$$\cos(x',z) = \sin 21^\circ 12' \sin\beta_p = 0.3616 \sin\beta_p$$

$$\cos(z',z) = -\cos\beta_p \sin 21^\circ 12' = -0.3616 \cos\beta_p$$

The above relationships may be summarized in a table of direction cosines

	r	t	z
x'	0.9323 $\sin\beta_p$	$\cos\beta_p$	0.3616 $\sin\beta_p$
y'	0.3616	0	-0.9323
z'	-0.9323 $\sin\beta_p$	$\sin\beta_p$	-0.3616 $\cos\beta_p$

For the first pitot-probe that was made, the angle $\beta_p = 39^\circ 46'$, and for the second, modified pitot-probe there is a choice of two settings corresponding to angles for β_p of $18^\circ 55'$ and $40^\circ 15'$.

The velocity components in the (r,t,z) system are calculated directly from the equations

$$\begin{aligned} w_r &= w_x \cos(x',r) + w_y \cos(y',r) + w_z \cos(z',r), \\ w_t &= w_x \cos(x',t) + w_y \cos(y',t) + w_z \cos(z',t), \\ w_z &= w_x \cos(x',z) + w_y \cos(y',z) + w_z \cos(z',z), \end{aligned} \quad (B18)$$

where

$$\begin{aligned} w_{x'} &= w \cos \phi, \\ w_{y'} &= w \sin \phi \cos \delta', \\ w_{z'} &= w \sin \phi \sin \delta' \end{aligned} \quad (B19)$$

To illustrate the use of the above analysis, a complete numerical calculation for one of the data points will be carried through.

4. Numerical Example

To illustrate the method of computation, the flow data for a specific measurement with the pitot-probe will be worked out in detail. Consider the 2200 rpm test-run having a discharge of 28.4 cfm, with a pitot setting of $r = 6.720$ inch and $\theta = 50^\circ 44'$. The manometer readings are tabulated below.

Manometer Reading (inch Water-Gage)	Equivalent Feet of Air at 62°F
$h_0 = - 0.28$	- 19.2
$h_1 - h_3 = 1.90$	130.0
$h_0 - h_3 = 3.19$	218.3
$h_2 - h_4 = 0.15$	10.5

From Fig. B5, for the ratios $(h_1 - h_3)/(h_0 - h_3) = 0.60$ and $(h_2 - h_4)/(h_0 - h_3) = 0.05$, the following values are obtained: $\phi = 10.3^\circ$, $\delta' = 86.0^\circ$ and $(k_0 - k_3) = 1.01$. The relative velocity is computed from equation (B13),

$$w = \sqrt{2g \frac{h_0 - h_3}{k_0 - k_3}} = 118.0 \text{ fps.}$$

The components with respect to the pitot-probe are derived from equation (B19),

$$w_{x'} = 116.1 \text{ fps,}$$

$$w_{y'} = 1.5 \text{ fps,}$$

$$w_{z'} = 21.1 \text{ fps.}$$

The probe was set at the angle $\beta_p = 40^\circ 15'$, and from the table of direction

cosines, and equation (B18), the velocity components with respect to the impeller are

$$w_r = 55.4 \text{ fps,}$$

$$w_t = 102.1 \text{ fps,}$$

$$w_z = 19.9 \text{ fps,}$$

$$w_m = \sqrt{w_r^2 + w_z^2} = 58.9 \text{ fps.}$$

The flow directions are

$$\delta = \text{arc tan } w_r/w_z = 70.2^\circ,$$

$$\beta = \text{arc tan } w_m/w_t = 29.9^\circ,$$

and the tangential component of the absolute velocity, and the whirl-moment, are

$$\begin{aligned} c_t &= r\omega - w_t \\ &= (0.560)(230.4) - 102.1 = 26.8 \text{ fps,} \end{aligned}$$

and

$$m = rc_t = 15.0 \text{ ft}^2/\text{sec.}$$

The static pressure head, h_s , is determined from equation (B15). From Fig. B6, for $\delta' = 86.0^\circ$ and $\phi = 10.3^\circ$, the pressure recovery factor is $k_o = 0.964$. The manometer reading must be corrected for the centrifugal effects upon the air column in the tubing leading from the pitot probe to the rotary seals. The absolute pressure at the center hole of the probe is

$$(p_o) = (p_{\text{man}}) \exp \left[\frac{w^2(r^2 - r_{\text{shaft}}^2)}{2g R_{\text{gas}}} \right]$$

where R_{gas} is the gas constant, and the shaft radius is 1.250 inch.

By substitution into equation (B15), and conversion to equivalent feet of air, the static pressure head is $h_s = 22.2$ ft.

The quantities H and I are obtained directly from the definitions

$$H = \frac{c^2}{2g} + h_s$$

$$= \frac{c_t^2 + w_m^2}{2g} + h_s = 87.2 \text{ ft,}$$

$$I = H - \frac{w}{g} m = -20.1 \text{ ft.}$$

APPENDIX C

DETAILS OF THE BLADE-TO-BLADE RELAXATION SOLUTION

1. Method of Solution

The solution of differential equation (43), together with the boundary conditions shown in Fig. 15, is accomplished by numerical procedures essentially developed by Southwell^{6,7}. The method consists in estimating the values of the stream function over a system of mesh points of a grid covering the flow region. The error ("residual" R_o) introduced into the finite-difference equation (44) by these estimated values, is expressed by the equation.

$$\psi_1 + \psi_2 + \psi_3 + \psi_4 - 4\psi_o + hf(\xi_o)(\psi_1 - \psi_3) - h^2g(\xi_o) = R_o \quad (C1)$$

The estimated values of ψ are adjusted ("relaxed") until the residuals are eliminated. A grid spacing, $h = 0.1$, was used initially in the computation. This grid spacing provides satisfactory accuracy in the upstream region where the flow conditions are quite uniform; however, in the downstream regions, and at the blade inlet tip, the gradient of the stream function is relatively large, and in these regions it is necessary to use finer grid spacing for improved accuracy. The grid spacing is shown in Fig. 16. At the inlet tip, and in the downstream regions, the grid spacing is 0.05; and in the immediate neighborhood of the blade exit tip, where the Kutta condition must be satisfied, the grid spacing is 0.025.

2. Irregular Grid Points

At the blade surface the nodes of the relaxation grid will not coincide with the blade contour. For these points, irregular star-operators must

be used. The most general case, in which all of the arms are of non-standard length, is shown in Fig. C1. Considering the origin of the (ξ, η) axes at the central point, ψ can be represented by the polynomial approximation,

$$\frac{\psi}{h^2} = b_0 + b_1 \left(\frac{\xi}{h}\right) + b_2 \left(\frac{\eta}{h}\right) + b_3 \left(\frac{\xi}{h}\right)^2 + b_4 \left(\frac{\eta}{h}\right)^2 + b_5 \left(\frac{\xi}{h}\right)\left(\frac{\eta}{h}\right). \quad (C2)$$

The b-coefficients are determined by solution of the five simultaneous equations obtained from substitution of values at the five nodal points.

This leads to the expressions for the derivatives.

$$h^2 \frac{\partial^2 \psi}{\partial \xi^2} = \frac{2}{a_1(a_1+a_3)} \psi_1 + \frac{2}{a_3(a_3+a_1)} \psi_3 - \frac{2}{a_1 a_3} \psi_0, \quad (C3)$$

$$h^2 \frac{\partial^2 \psi}{\partial \eta^2} = \frac{2}{a_2(a_2+a_4)} \psi_2 + \frac{2}{a_4(a_4+a_2)} \psi_4 - \frac{2}{a_2 a_4} \psi_0, \quad (C4)$$

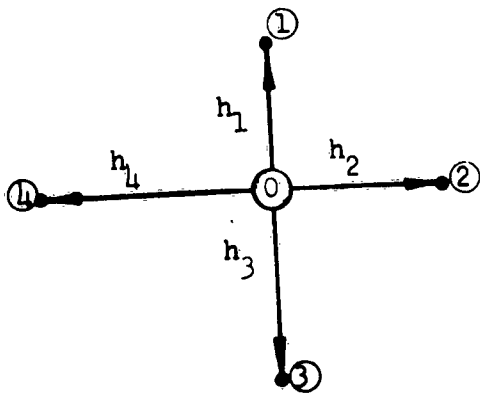
$$h \frac{\partial \psi}{\partial \xi} = \frac{a_3}{a_1(a_1+a_3)} \psi_1 - \frac{a_1}{a_3(a_3+a_1)} \psi_3 - \frac{(a_3-a_1)}{a_3 a_1} \psi_0 \quad (C5)$$

For the special case of $a_3 = a_4 = 1$, the values of the coefficients of ψ are tabulated by Shaw⁸.

The blade inlet tip does not coincide with a nodal point of the grid, so the irregular star shown in Fig. C2 is used. Applying the notation of this figure to equation (C2), the expressions for the derivatives at the inlet tip become

$$h^2 \nabla^2 \psi = \frac{1}{2}(\psi_1 + \psi_3) + \frac{1}{(a_t+1)} \left[\psi_2 + \frac{1}{a_t} \psi_4 - (2+a_t + \frac{1}{a_t}) \psi_0 \right] \quad (C6)$$

$$h \frac{\partial \psi}{\partial \xi} = \frac{1}{4}(\psi_1 - \psi_3) + \frac{a_t}{2(a_t+1)}(\psi_2 - \psi_0) + \frac{1}{2a_t(a_t+1)}(\psi_4 - \psi_0). \quad (C7)$$



$$a_1 = \frac{h_1}{h}, a_2 = \frac{h_2}{h}, \text{ etc.}$$

h = standard arm length

Fig. C1 NOTATION FOR IRREGULAR STAR OPERATOR

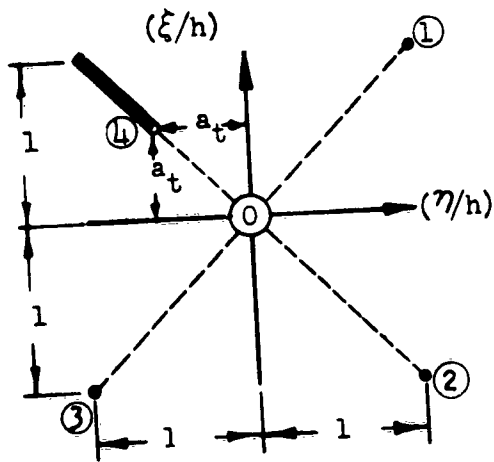


Fig. C2 NOTATION FOR STAR OPERATOR APPLIED AT BLADE INLET TIP

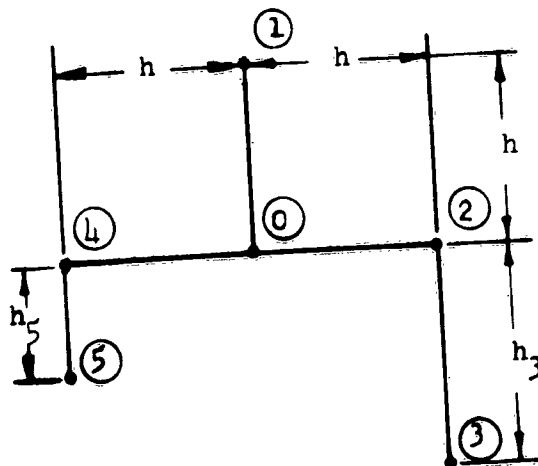


Fig. C3 IRREGULAR TRANSITION POINT BETWEEN FINE AND COARSE GRIDS.

At transition points between the fine and coarse grid spacing, irregular star operators must be used corresponding to equations (C3), (C4), and (C5). In addition, another type of transition point occurs as shown in Fig. C3. Using the polynomial approximation, equation (B2), the derivatives are

$$h^2 \frac{\partial^2 \psi}{\partial \xi^2} = \frac{1}{(2+a_3+a_5)} \left[\frac{2}{a_3} (\psi_3 - \psi_2) + \frac{2}{a_5} (\psi_5 - \psi_4) - 4(\psi_0 - \psi_1) \right], \quad (C8)$$

$$h^2 \frac{\partial^2 \psi}{\partial \eta^2} = \psi_2 + \psi_4 - 2\psi_0, \quad (C9)$$

$$h \frac{\partial \psi}{\partial \xi} = \frac{1}{(2+a_3+a_5)} \left[\frac{1}{a_3} (\psi_2 - \psi_3) + \frac{1}{a_5} (\psi_4 - \psi_5) + (a_3+a_5)(\psi_1 - \psi_0) \right] \quad (C10)$$

3. Kutta-Joukowski Condition

Considering the blades to be thin, the flow must be tangent to the blade surface at the exit. For the preliminary relaxation solution, no attempt was made to satisfy this condition. The downstream whirl-moment value was chosen on the basis that the flow leaves the impeller uniformly, at the specified blade angle. After completion of the relaxation solution, it was found that the β -angle of the streamline, at the blade exit tip, was about 10 degrees less than the blade angle. To correct this condition, a decrease in the downstream whirl-moment was necessary. As a first approximation of the change in whirl-moment required, consider a unit change in whirl-moment, and let $\Delta\psi$ represent the corresponding changes in the stream function. Referring to equation (C1), the values of h , f , and g are small, and the terms involving these factors approach zero to a higher order, as the grid spacing is reduced, than the first four terms of the

equation. The finite-difference equation for $\Delta\psi$ then becomes, approximately,

$$\Delta\psi_1 + \Delta\psi_2 + \Delta\psi_3 + \Delta\psi_4 - 4\Delta\psi_0 = R_0. \quad (C11)$$

On the blade contour, ψ is fixed, so that $\Delta\psi$ is zero at the blade. Equation (C11), representing the Laplace equation in $\Delta\psi$, can be solved by the relaxation method. As this equation is linear, the solution for any desired change of whirl-moment can be obtained by multiplication by the solution for the unit change in whirl-moment. After the whirl-moment is adjusted to satisfy the Kutta condition, a final relaxation must be done to eliminate the small residuals of equation (C1).

4. Determination of the Velocity Distribution

Lines of constant Ψ -values are relative streamlines, and the numerical value of Ψ indicates the rate of flow passing between the streamline and the leading blade face, as a percentage of the total flow passing through the channel between adjacent blades. The spacing of the streamlines (see Fig. 16) is indicative of the magnitude of the relative velocity, close spacing indicating higher velocities. The relative velocity components along the periphery at the blade outlet are determined by numerical differentiation of the stream-function using a seven-point differentiation formula given by Southwell⁷ for equally spaced grid points, and a five-point differentiation formula given by Wu⁹ for the unequally spaced grid points.

BIBLIOGRAPHY

- (1) Spannhake, W. Theoretical Studies of the Flow Through Turbomachines Contract No. Nonr. 322(00), Dept. of Mechanical Engineering Illinois Institute of Technology.
- (2) Wu, C. H. A General Through-Flow Theory of Fluid Flow with Subsonic or Supersonic Velocity in Turbomachines of Arbitrary Hub and Casing Shapes, NACA TN 2302, 1951.
- (3) Ruden, P. Untersuchungen Ubereinstufige Axialgeblase Luftfahrtforschung V. 14, 1937 (Translation, NACA TM 1062, April 1944)
- (4) Stanitz, J.D. Two-Dimensional Compressible Flow in Conical Mixed-Flow Compressors, NACA TN 1744, 1948
- (5) Stanitz, J.D. Two-Dimensional Flow on General Surfaces of Revolution in Turbomachines, NACA TN 2654, 1952
Ellis, G.O.
- (6) Southwell, R.V. Relaxation Methods in Engineering Science, Clarendon Press (Oxford), 1940.
- (7) Southwell, R.V. Relaxation Methods in Theoretical Physics, Clarendon Press (Oxford), 1946.
- (8) Shaw, F.S. An Introduction to Relaxation Methods, Dover Pub., 1953
- (9) Wu, C. H. Formulas and Tables of Coefficients for Numerical Differentiation with Function Values Given at Unequally Spaced Points and Application to the Solution of Partial Differential Equations. NACA TN 2244, 1950
- (10) Pearson, C.E. Measurement of Instantaneous Vector Air Velocity by Hot Wire Methods. J. of Aero. Sc. 1952
- (11) Pearson, C.E. Quantitative Measurement of Fluctuation in Air Flow by Hot-Wire Techniques, Rept. 126, Pratt and Whitney Project at Harvard University, 1950.
- (12) Hamrick, Misisin Study of Three-Dimensional Flow Distribution Based on Measurements in a 48-inch Radial-Inlet Centrifugal Impeller, NACA TN 3101, 1954.
and Michel
- (13) Wislicenus, G.F. Fluid Mechanics of Turbomachinery, McGraw-Hill, 1947
- (14) Stanitz, J.D. Centrifugal Compressors (Lecture 4), Gas Turbine Lectures, Dept. of Mech. Eng. University of Michigan

BIBLIOGRAPHY (Cont.)

- (15) Stodola, A. Steam and Gas Turbines, Vol. II. McGraw-Hill, 1927
- (16) Ellis, G. O. Two-Dimensional Compressible Flow in Centrifugal Com-
Stanitz, J. D. pressors with Logarithmic-Spiral Blades, NACA TN 2255,
1951.
- (17) Prian, V. D. An Analysis of Flow in Rotating Passage of Large Radial
Michel, D. J. Inlet Centrifugal Compressor at Tip Speed of 700 Feet
Per Second, NACA TN 2584.